

A High-Rotation General Circulation Model Experiment with Cycle Time Changes

By
Russell L. Elsberry

Department of Atmospheric Science
Colorado State University
Fort Collins, Colorado

Prepared as a Ph.D. dissertation with support from the Office of Naval Research
(Contract N000014-67-A-0299-0003-AA) and the Environmental Science Services
Administration (Grant E22-138-67(G)).
December, 1968



**Department of
Atmospheric Science**

Paper No. 134

A HIGH-ROTATION GENERAL CIRCULATION MODEL
EXPERIMENT WITH CYCLIC TIME CHANGES

by

Russell L. Elsberry

This report was prepared as a Ph. D. dissertation with support from the Office of Naval Research (Contract N000014-67-A-0299-0003-AA) and the Environmental Science Services Administration (Grant E22-138-67(G)).

Department of Atmospheric Science
Colorado State University
Fort Collins, Colorado

December 1968

Atmospheric Science Paper No. 134

ABSTRACT

A HIGH-ROTATION GENERAL CIRCULATION MODEL EXPERIMENT WITH CYCLIC TIME CHANGES

The phenomenon of vacillation in a rotating annulus is studied as a possible analogue for the atmospheric index cycle. With a simple distribution of heat sources we attempt to isolate the essential mechanisms by which a baroclinic fluid system undergoes periodic variations in troughline tilt and vortex growth and decay.

For comparison with atmospheric wave cyclones, the three-dimensional flow circulation in the annulus is computed at various stages of the vacillation. A diagnostic scheme including the balance equation for the horizontal, non-divergent streamfunction, and the quasi-geostrophic ω -equation for the vertical motion is used. The similarity between the annulus flow and the atmosphere is striking. The correct position of the low-level cyclone with respect to the top surface jet is observed and consequently also similar distributions of vertical motion, convergence and divergence. A three-cell pattern in the mean meridional motion is evident throughout the vacillation.

Although boundary layers present at all of the surfaces have important roles in the external forcing of the flow, we are mainly interested in the mechanisms by which the interior fluid accomplishes the various transports required of it. Most important of these is the transfer of heat from the sources at the outer wall and the base heating ring to the cold source at the inner rim. The eddy heat transfer is extremely efficient near midradius, transferring much more heat than is required by the source. A strong compensating indirect cell is set up to counteract this excess heat transfer. The total

heat content of the fluid is decreasing during the vortex stage as more heat is transferred to the cold source than is provided at the sources.

Two important differences are noted in the energy cycle: The importance of conversion of zonal potential energy into zonal kinetic energy in the boundary layers, and the zonal motions drive the eddies, particularly prior to vortex development.

Intensification of the jet is observed under stable conditions, according to the theorem of Charney and Stern (1962). But the more general case is fulfillment of the necessary, but not sufficient, condition for instability, with both cases of growth and of decay in jet speeds being observed. A seemingly unstable configuration of potential vorticity in the jet is maintained as the jet axis shifts in radial tilt and orientation. The jet maximum does decay at times when the necessary condition is satisfied, but the sufficient condition for decay is not known and no quantitative prediction of the breakdown is achieved. Finally we suggest that vacillation may be characterized as a quasi-stable oscillation about equilibrium potential vorticity states. With only slight variations in rotation or heating from the conditions for steady waves, the tendency toward conservation of potential vorticity leads to stable shifts of the jet axis until sufficiency conditions for instability occur.

Russell Leonard Elsberry
Atmospheric Science Department
Colorado State University
Fort Collins, Colorado 80521
December, 1968

ACKNOWLEDGEMENTS

An experimental study such as the following is dependent on the efforts and cooperation of many individuals. Foremost were those of Professors Dave Fultz and Herbert Riehl who planned this experiment at the University of Chicago after analyzing a steady three-wave case. Professor Fultz and his associates, principally Mrs. J. Weil and G. Gray, and later T. Spence, completed the experiment and preliminary data analysis. In addition a number of check experiments were run and special investigations were carried out as the analysis proceeded.

These experimental data were kindly presented to the author by Professor Riehl, who, in addition to serving as advisor, arranged for the author to spend a year at Imperial College. The author is especially indebted to the faculty, staff and students of the Department of Meteorology, Imperial College, under the direction of Professor P. Sheppard, for their assistance, cooperation, and helpful discussions. Computer time for data handling and computations was granted by the Imperial College Computing Centre.

The author would also like to thank the other members of his dissertation committee, including Professors F. Baer, L. Baldwin, and H. Nicholson. In addition the author acknowledges many profitable discussions with colleagues at Colorado State University and the Naval Postgraduate School.

Finally a grateful acknowledgement to the author's wife Linda for her assistance in the data handling and typing as well as her encouragement.

This work was carried out under a grant from the Office of Naval Research.

TABLE OF CONTENTS

CHAPTER	PAGE
I. INTRODUCTION	1
Purpose	
Experimental conditions	
Plan of the research	
II. DATA	8
Top surface flow	
Temperature	
PART A. STRUCTURE OF THE FLOW	25
III. TOPOGRAPHY OF TOP SURFACE	25
IV. INTERIOR HORIZONTAL FLOWS	29
V. VERTICAL MOTION	36
Divergent part of the velocity	
Mean meridional motion	
PART B. GENERAL CIRCULATION	46
VI. HEAT BALANCE	47
Cycle mean heat balance	
Additional mean meridional motion	
Constant heat source	
Summary of the heat balance	
VII. ANGULAR MOMENTUM	58
VIII. ENERGY CYCLE	61
Evaluation of the energy cycle quantities	
Energy quantities versus cycle time	
Energy cycle over a complete vacillation	
Time dependent energy cycle	
Comparison with atmosphere	
Release of potential energy in jet coordinates	
IX. POTENTIAL VORTICITY CONSIDERATIONS	78
Growth and decay of the jet	
Vacillation versus steady state	
X. CONCLUSION: ANNULUS--ATMOSPHERE ANALOGUE	92
Structure of the circulation	
Effect of annulus geometry on the flow mechanisms	
LITERATURE CITED	99
APPENDICES	102
A. Processing of temperature data	
B. Top surface configuration	
C. Quasi-geostrophic ω equation	
D. Heat and mass balance in top layer	
E. Energy cycle equations	
F. Mixed barotropic-baroclinic instability	

LIST OF TABLES

Table	Page
1 Wave speed versus cycle time	9
2 Time deviations of eddy temperature variance	67
3 Locations of λ - t diagrams	103
4 Mass flow through the 7-6 cm layer	109

LIST OF ILLUSTRATIONS

Figure		Page
1	Surface photographs versus cycle time	4
2a-d	Surface isotach analyses	10
3a-b	Deviations from overall mean temperature; mean lapse rate	15
4a-b	Detailed temperature structure near cold and warm walls	16
5	Temperature difference junction λ -t diagram at $z = 2.5$ cm	18
6a-d	Horizontal temperature fields at $z=6, 4, 2,$ and 0.1 cm	21
7	Horizontal grid	27
8a-d	Streamfunction at $z = 6, 4, 2$ and 0.1 cm	32
9a-d	Vertical motion ω at $z = 5$ and 2 cm.	38
10a-d	Stokes streamfunction at $T = 1, 5, 9, 13$	44
11	Cycle mean heat balance	49
12	Radial distribution of heat transfer vs cycle time	52
13a-c	Integrated horizontal heat transfer near walls	54
14a-b	Cycle mean and time changes of momentum sources and sinks; vertically integrated eddy momentum flux	59
15	Energy quantities versus cycle time	66
16	Energy cycle over a complete vacillation	66
17a-b	Energy cycle versus cycle time for \bar{P}, P', \bar{K} and K'	70
18a-b	Temperature profiles corresponding to maximum and minimum energy temperature deviations from the overall mean	72
19a-b	Profiles of vertical motion and temperature across the jet axis; correlation $[w] [T]$ versus cycle time	75
20a-b	Mean velocity in the layer $21-22^{\circ}\text{C}$. at midradius; potential vorticity in the layer $21-22^{\circ}\text{C}$ at midradius	81
21a-b	Same as Figure 20 for $20-21^{\circ}\text{C}$ layer	82
22a-b	Same as Figure 20 for $19-20^{\circ}\text{C}$ layer	83

LIST OF SYMBOLS

r	radius, radial direction coordinate
r_i	inner radius
r_o	outer radius
Ω_o	angular rotation rate
g	gravitational acceleration
ϵ	thermal expansion coefficient
δ	depth
δ^*	Ekman depth
$f=2\Omega_o$	Coriolis parameter
R	kinematic Rossby number
R_{oT}	thermal Rossby number
$\omega=\frac{dp}{dt}$	vertical motion in pressure coordinate
p	pressure
U	typical zonal velocity component
t	time (cycle phase)
λ	angular displacement from surface troughline in wave coordinates
z	height above base
h	pressure height
θ	azimuthal coordinate
V_r, V_θ	velocity components in r, θ coordinates
ζ	relative vorticity
C_D	drag coefficient
D_h	two-dimensional divergence
V	total speed relative to pan
ν	kinematic viscosity
α	specific volume

$J(,)$	Jacobian operator
ψ	streamfunction
w	vertical motion in z coordinates
ρ	density
ψ_c	streamfunction in wave coordinates
τ	non-dimensional temprature
Q	non-dimensional rate of heat addition
σ	static stability
χ	streampotential
\bar{K}, K'	zonal, eddy kinetic energy
\bar{P}, P'	zonal, eddy available potential energy
p_s, p_B	pressures at the top surface, bottom
$C(,)$	conversion between two energy forms
$D()$	dissipation of kinetic energy
$G()$	generation of potential energy
$\langle \rangle$	integration over the whole mass of fluid
F	frictional force per unit mass
β^*	linearized thermal expansion coefficient
$\beta(=0)$	variation of Coriolis parameter f
q	potential vorticity
ζ_g	geostrophic vorticity
D	distance between isothermal surfaces
R_s	radius of curvature
n	normal coordinate

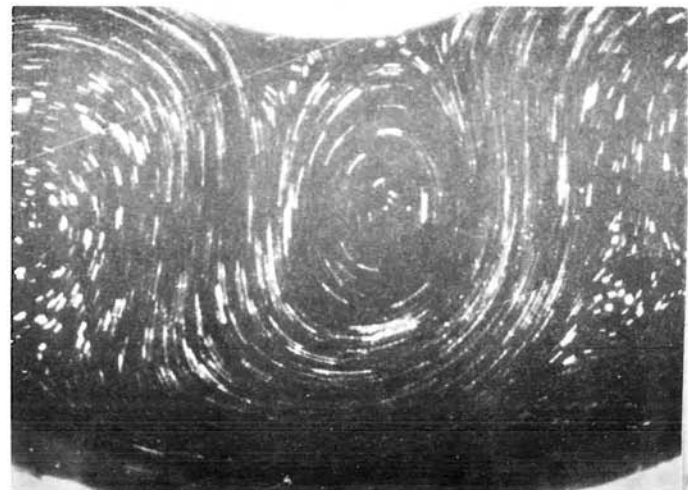
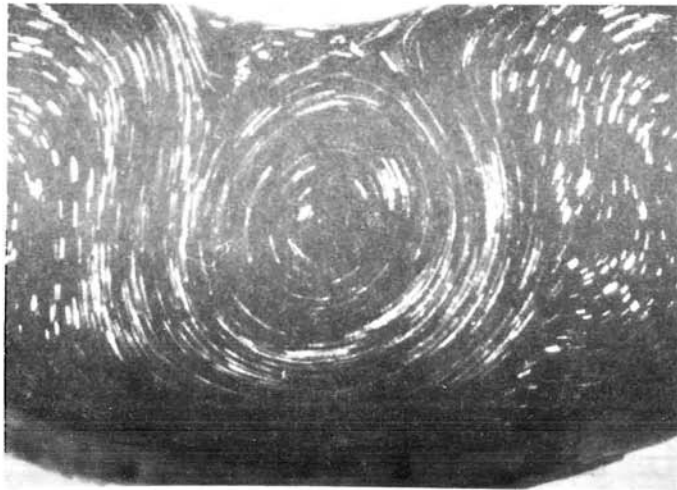
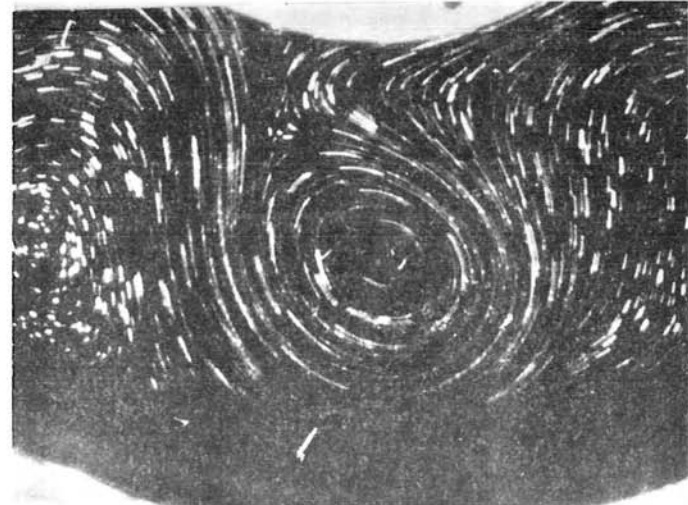
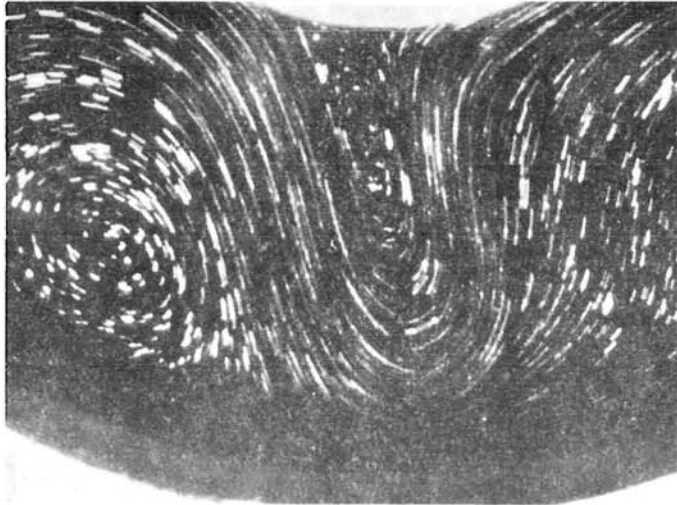


Fig. 1 Photographs of top surface aluminum powder streaks at alternate rotations illustrating the vacillation cycle with a period of close to 16 rotations. $T = 1$, upper left; $T = 3$, upper right; $T = 5$, lower left; $T = 7$

$J(,)$	Jacobian operator
ψ	streamfunction
w	vertical motion in z coordinates
ρ	density
ψ_C	streamfunction in wave coordinates
τ	non-dimensional temprature
Q	non-dimensional rate of heat addition
σ	static stability
χ	streampotential
\bar{K}, K'	zonal, eddy kinetic energy
\bar{P}, P'	zonal, eddy available potential energy
p_S, p_B	pressures at the top surface, bottom
$C(,)$	conversion between two energy forms
$D()$	dissipation of kinetic energy
$G()$	generation of potential energy
$\langle \rangle$	integration over the whole mass of fluid
F	frictional force per unit mass
β^*	linearized thermal expansion coefficient
$\beta(=0)$	variation of Coriolis parameter f
q	potential vorticity
ζ_g	geostrophic vorticity
D	distance between isothermal surfaces
R_S	radius of curvature
n	normal coordinate

CHAPTER 1

INTRODUCTION

Purpose. To understand the complex motions of the atmosphere, it is helpful to isolate the essential features of the circulation in simple models. Laboratory models with widely differing arrangements of heat and momentum sources and sinks, as well as geometries vastly departing from dynamic similitude requirements, have opened up the possibility of controlled experiments on the large-scale atmospheric circulations. The existence of experimental analogues, in which various requirements of dynamic similitude are not satisfied, can indicate which of the various parameters are important in determining the flow.

Fultz(1952, 1956) and Hide (1953, 1956) have shown that at least four distinct flow regimes result when water in a rotating annulus is heated at the outer rim and cooled at the inner rim. Maintaining the same temperature difference across the fluid, variations in rotation lead to transitions between: (a) an axisymmetric Hadley cell, (b) steady state progressive wave motion, with transitions to higher wave numbers at higher rotations, (c) vacillating wave motion, discovered by Hide (1956), and (d) unsteady, asymmetric wave motion. The motion, shown by small aluminum particles floating on the top surface or various tracers in the interior of the fluid, is surprisingly similar to large-scale planetary circulations. When normalized in terms of the equatorial velocity and other characteristic parameters, quantitative comparisons indicate that these controllable experiments can be very helpful in the study of atmospheric dynamics.

A complete study of these experimental analogues requires information on their three-dimensional structure. Thus a series of experiments at the University of Chicago was planned to obtain internal temperature and top-surface velocity data to define this structure for each of the four classes. Having such data, Riehl and Fultz (1957, 1958) were able to compute the internal flows, as well as suggest the mechanisms which maintain the steady-state wave motion. Väisänen (1961) carried out a similar analysis for the symmetric Hadley cell. This study continues the plan for the vacillation case, based on data taken in the Hydrodynamics Laboratory of the University of Chicago by Professor Dave Fultz.

The phenomenon of vacillation may take on many variations depending on the heating and rotation rates for the particular geometry. Pfeffer and Chiang (1967) have described a type of vacillation which involves amplitude variations only. In this case we interpret vacillation to be the cyclic variation of troughline orientation (with respect to radial lines) and wave amplitude (Figure 1). The troughline of the surface streamflow varies from a southwest-northeast (north toward center of rotation) "tilt" through a radial orientation to a southeast-northwest tilt. That is, the sense of the angular momentum transfer by horizontal eddy motion reverses over the period of the cycle. As the wave moves into the SE-NW tilt large cyclonic circulations develop in the troughs. Thus with a period of 16 rotations, the surface flow goes through a reversal of "eddy" angular momentum flow and, intuitively with the analogy to development of vortices in the atmosphere, a variation in heat flow. While the angular momentum

and heat fluxes are not explicitly related to the troughline tilt, this tilt is considered the essential feature of vacillation (Fultz, personal communication).

The atmospheric phenomenon for which vacillation in the annulus is an analogue is the index cycle. A "cycle" in values of the zonal index, the longitudinal mean of the surface geostrophic wind, has been qualitatively associated with changes in the large-scale atmosphere circulation. High index values occur with zonal motion, alternating with low values which occur when disturbances form and meridional motion is more dominant. While the concept of an index cycle has proven useful in a descriptive sense, attempts to obtain quantitative evidence for its existence have generally failed.

By studying the vacillation which involves a simple distribution of heat sources, we hope to isolate the essential mechanisms by which a baroclinic fluid system is able to undergo periodic variations. Atmospheric waves at best undergo quasi-periodic variations for only short periods. However since the present forecasts for longer than a few days are mainly statistical, an increased understanding of the factors involved in the development and maintenance of quasi-periodic variations would be of considerable value.

Experimental conditions. Details of the experiment and the associated equipment are contained in Fultz, et al (1959) and a series of contract reports (e.g. Fultz 1964). The annulus has an outer radius r_o of 19.525 cm, an inner radius r_i of 7.825 cm, and is filled to a depth of 7.00 cm with water containing a small amount of detergent.

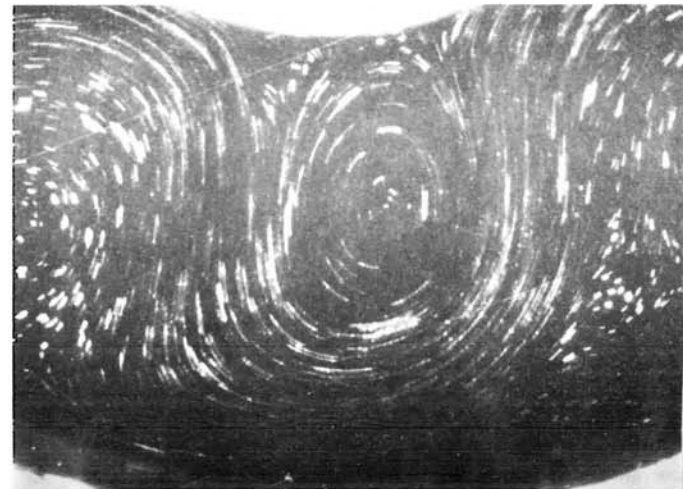
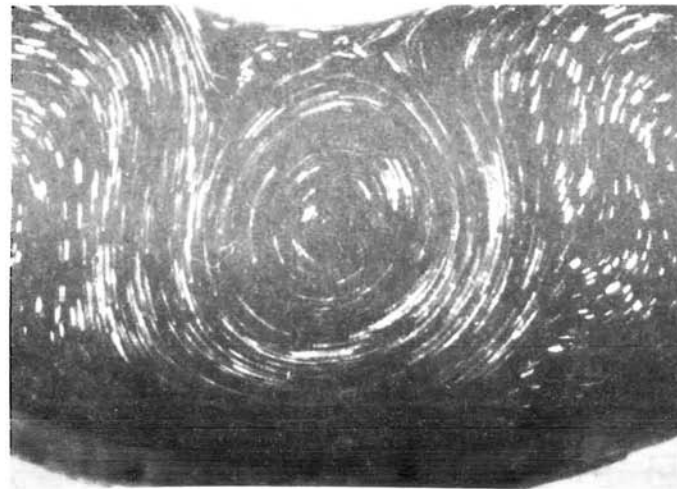
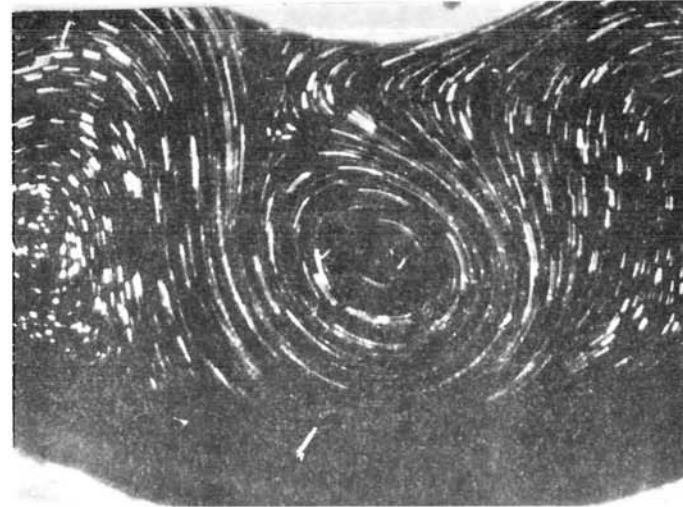
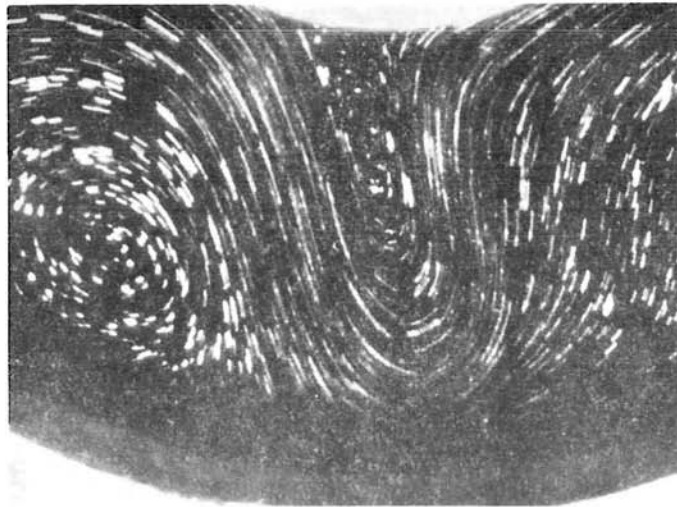


Fig. 1 Photographs of top surface aluminum powder streaks at alternate rotations illustrating the vacillation cycle with a period of close to 16 rotations. $T = 1$, upper left; $T = 3$, upper right; $T = 5$, lower left; $T = 7$

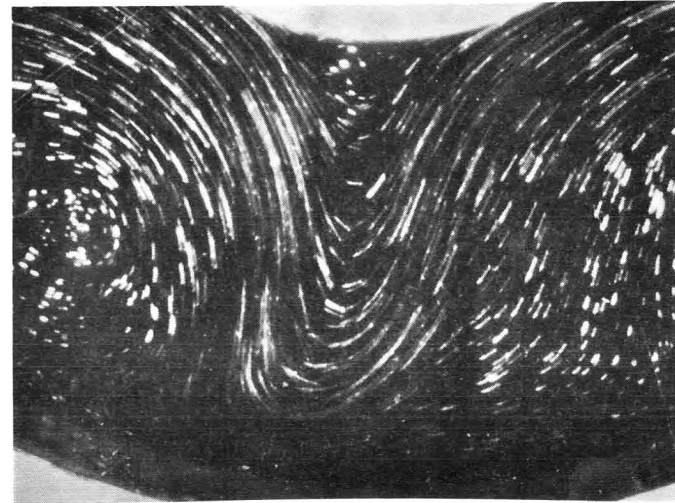
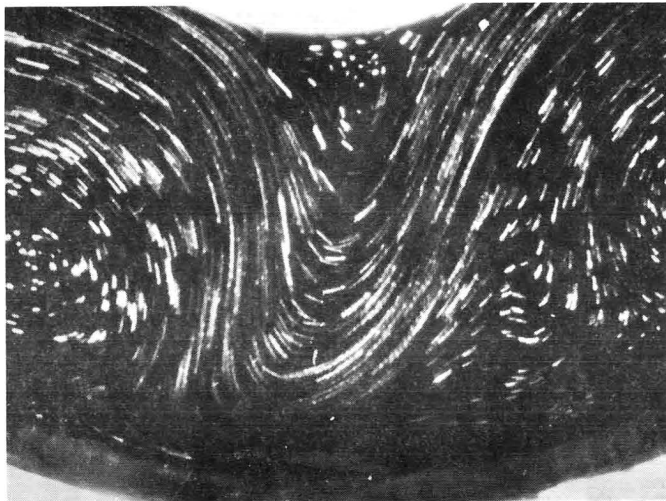
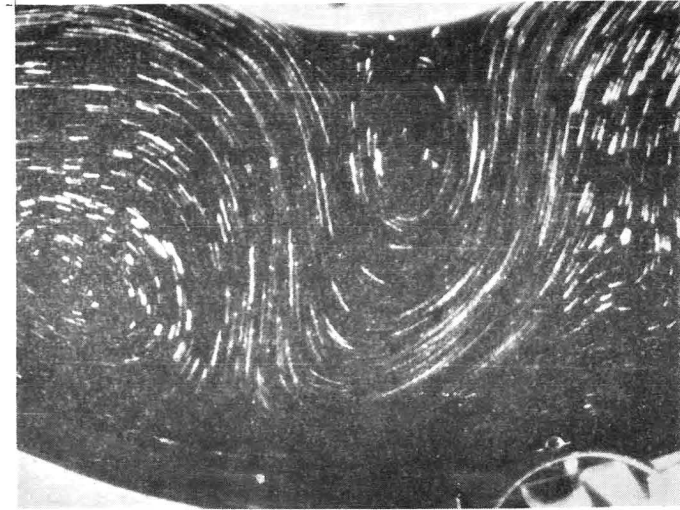


Fig. 1 (cont'd) T = 9, upper left; T = 11, upper right; T = 13, lower left; T = 15. Inner radius, 7.825 cm; outer radius, 19.525 cm; angular rotation rate, 0.5 sec^{-1}

Heat is added to the fluid at the outer rim by means of heating coils in contact with the rim. Heat is also added by a base heating ring extending from $\frac{r}{r_0} = 0.6$ to 0.8 since, from experience, this helps to make the vacillation periodic and shifts the jet inward from the wall. Total nominal heating of 95 watts, 80 at rim and 15 at base, is comparable to the 100 watts used in the symmetric case (Väisänen, 1961) and the three-wave case (Riehl and Fultz, 1957, 1958). However all of the heating was at the rim in those cases. Thus the main difference between the experiments is the rotation rate $\Omega_c = 0.05, 0.3$ and 0.5 sec^{-1} for symmetric, three-wave and five-wave vacillating cases.

The parameter most important in distinguishing the regimes is the thermal Rossby number $R_{OT} = \frac{g\varepsilon(\Delta r T)\delta}{(r_0\Omega_0)f\Delta r}$ which is the ratio of the thermal wind to the equatorial rim speed $r_0\Omega_0$. Here we use the notation of Fultz (1959) where ε is the thermal expansion coefficient, $\frac{\Delta r T}{\Delta r}$ is a typical radial temperature gradient, δ is the depth, and $f = 2\Omega_0$ is the Coriolis parameter. Values of R_{OT} for the respective experiments are 3, 0.19 and 0.025.

Plan of the research. Having shown that the surface flow patterns are analogous to those in the atmospheric index cycle, we first establish analogy of internal circulations as well. The available data include the surface velocities from the photographs of Figure 1, and the temperature field throughout the field.

In Part A on the structure of the flow, the technique for computing the horizontal streamfunction is discussed. Although the quasi-horizontal flow in the interior can be made visible by dye releases and other techniques, quantitative measurements are difficult

and are used only to check the computed streamfunction patterns. As in investigations of atmospheric energetics and mechanisms, the computation of the vertical motion in the annulus is crucial. We here use the so-called ω equation which is also used for large-scale atmospheric vertical motion calculations.

To complete the atmosphere-annulus analogy we compute in Part B the various statistical parameters which specify the general circulation. Other than the mass balance implied by the continuity equation, there are several constraints which the flow must simultaneously satisfy. By computing these quantities we can determine the mechanisms by which the fluid transfers heat and momentum from sources to sinks. The generation of potential energy, conversion to kinetic energy and then the dissipation of kinetic energy form the links in the energy cycle. Here the vertical motion calculations are very important in the transformations between various energy forms, although the kinetic energy of the vertical component is negligible. Thus in Part B how the vacillation occurs is described in terms of general circulation balances and integral constraints.

To explain why the vacillation occurs we look for an instability criterion involving both baroclinic and barotropic effects. When applied to coordinates aligned with the jet stream, the criterion predicts the growth and decay of the jet stream. Further consideration of the potential vorticity suggests the explanation for the occurrence of vacillation versus steady state waves. In conclusion we discuss the various factors involved in comparing the vacillation in the annulus to the index cycle in the atmosphere.

CHAPTER II

DATA

As in Riehl and Fultz (1957) the internal flow velocities will be computed using (a) surface velocity measurements and (b) temperature (converted to specific volume) measurements in the interior. The temperatures were digitally recorded each rotation and, as shown later, were converted to values at times corresponding to a surface photograph.

Each of the five waves goes through the vacillation cycle nearly simultaneously. Fultz (1968) has isolated the slight phase lead of one or two of the waves with respect to the others as probably being due to a slight ellipticity in the bottom surface. This has only a small effect on the temperature data which is the mean of three thermocouples in three different waves. In each of the diagrams we present only one wave implying that all five are exactly identical in the structure and development.

Top surface flow. The kinematic Rossby number $R = \frac{U}{r_o \Omega_o}$ is an important parameter for comparison between experiment and atmosphere, as was suggested by Rossby (1947). Since R is the ratio of convective to Coriolis accelerations, the value of 0.09 based on the surface jet speed indicates that the motion was less ageostrophic than for the three-wave case where $R \sim 0.2$. And with $R \ll 1$ the use of the ω -equation is justified for computation of the vertical motion.

The most distinguishable feature of the photographs of the surface flow is the orientation of the jet streams. Without detailed analysis of the streak measurements, it is possible to specify the various stages of the vacillation. The time at which the tilt of the troughline was advancing from west to east through the radial

orientation was chosen as the beginning of cycle time. Because the vacillation is periodic, linear interpolation between successive radial orientations specifies the time variation. For most of the experiments this interval is very nearly 16 rotations. We then can specify the cycle phase time t of photographs taken each rotation on a scale from 0 to 1. However in the diagrams we specify the time as rotations (1 to 16) past the beginning of the cycle corresponding to the particular series of surface photographs.

A longitudinal grid moving at the same speed as the wave is utilized. The zero point of this wave longitude grid is chosen to be the midpoint between the outward and inward surface jet maxima at midradius. Again without detailed measurements of the streaks one is able to specify the position λ of a streak (or a thermocouple) with respect to wave zero longitude (WZL). Of course the latitude is specified in terms of equal radial increments.

Data in a coordinate system moving with the wave can be converted to a coordinate system fixed to the pan knowing the velocity of the system. Table 1 shows the displacement of the WZL (defined at midradius) versus cycle time. Because of the tilt of the trough, the local wave speed varies with radius.

Table 1
Wave speed ($^{\circ}$ deg long./revolution) vs cycle time

T = 1	5.6	T = 9	5.45
3	4.55	11	5.9
5	4.45	13	6.25
7	4.85	15	6.3

Figures 2a to d show the isotach analyses derived from the streak measurements. Largest velocities of 9 per cent of the rim speed are reached very near the inner cold wall. This jet at the inner

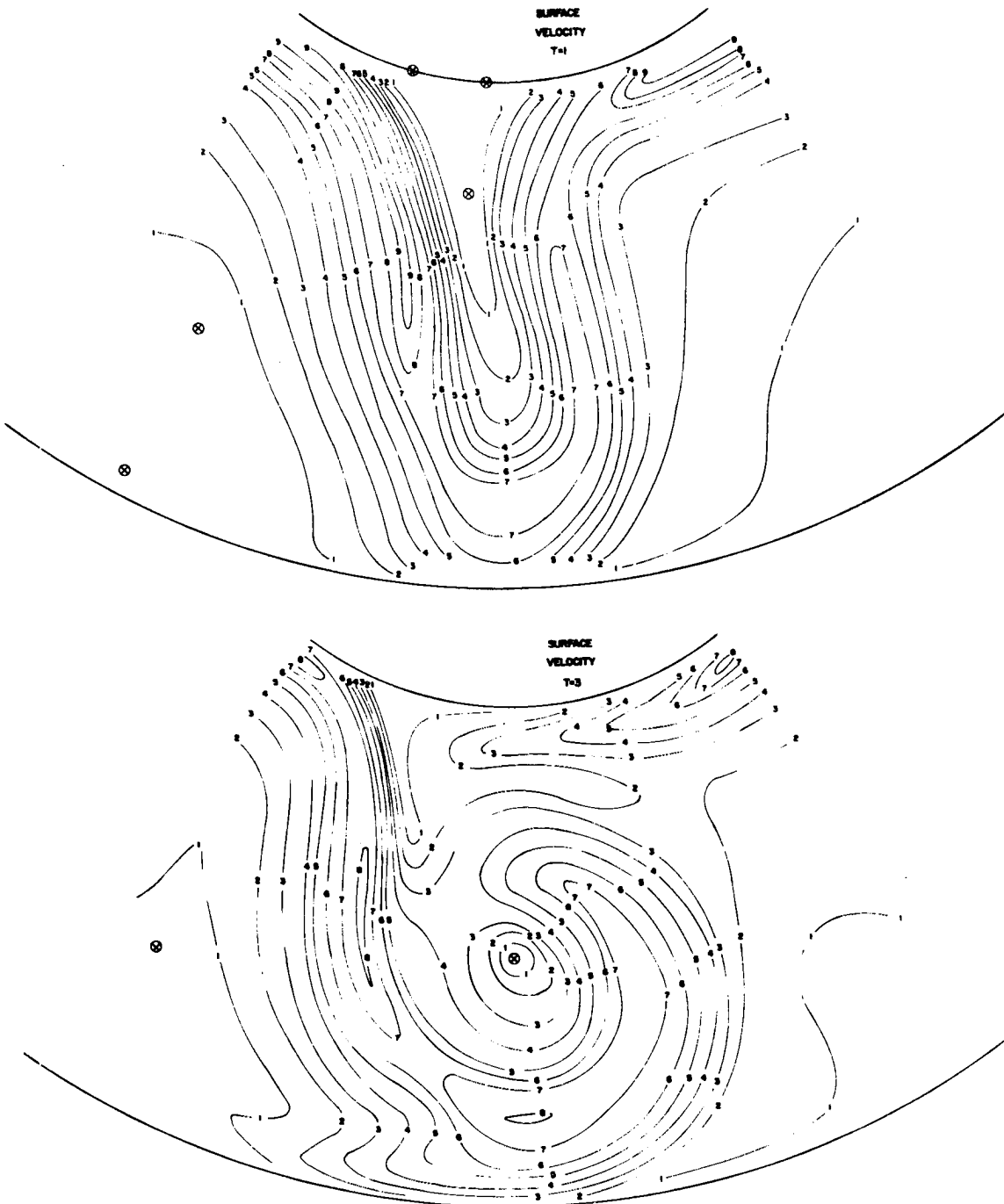


Fig. 2a Velocity of top surface from length of aluminum powder streaks, expressed as per cent of equatorial (outer) rim speed. $T = 1$ (top) and $T = 3$.

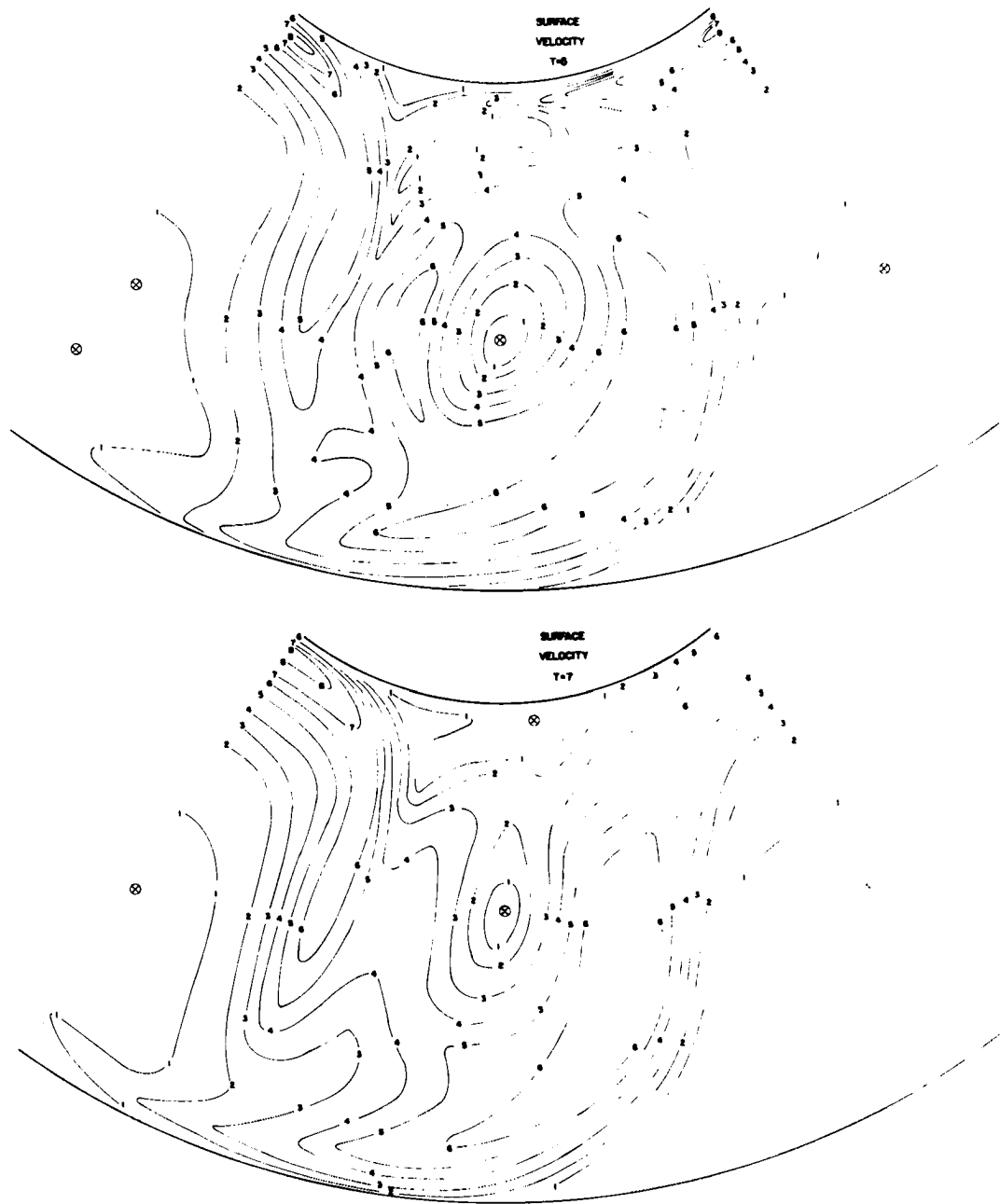


Fig. 2b Same as Fig 2a for $T = 5$ (top) and $T = 7$

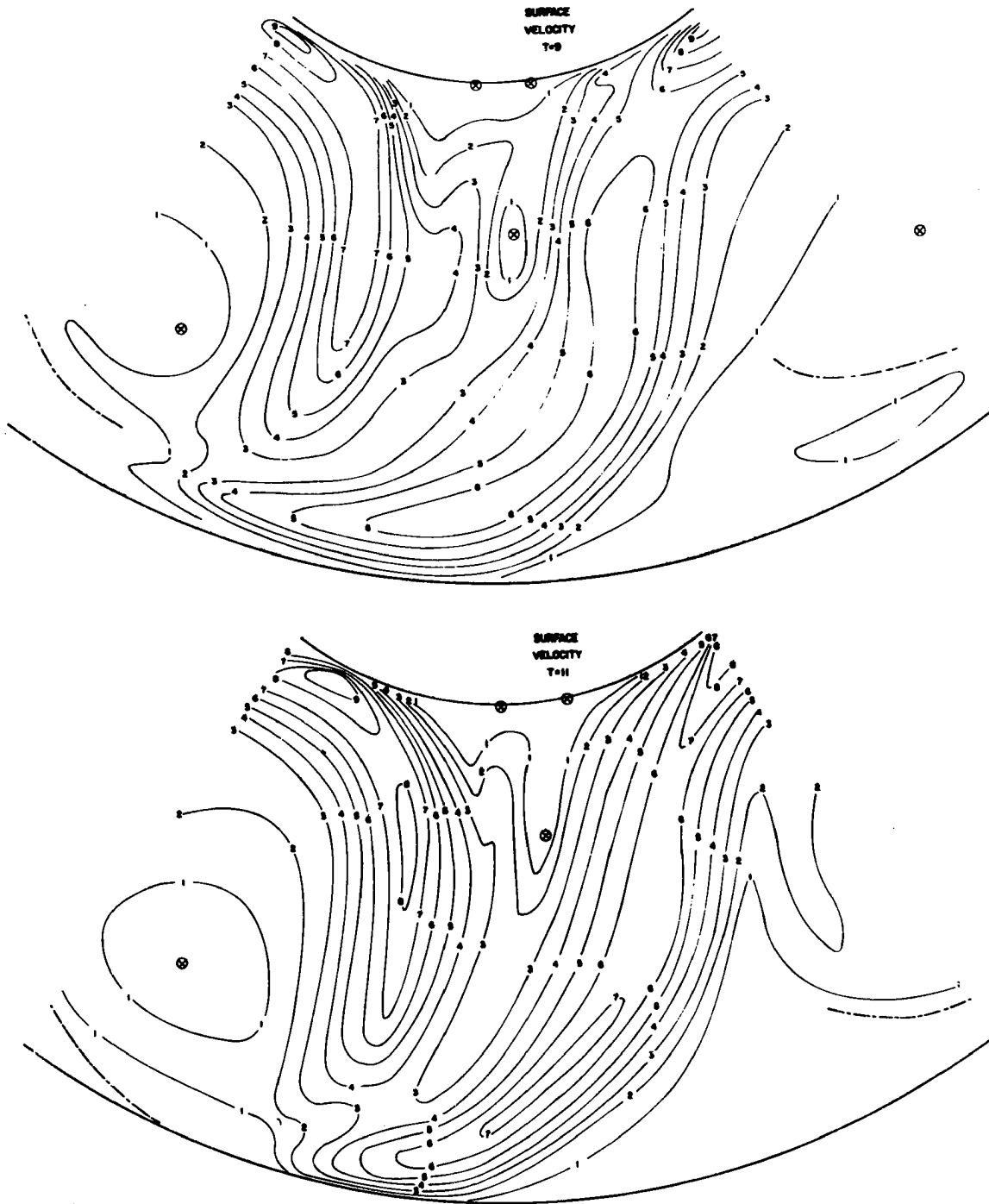


Fig. 2c Same as Fig 2a for $T = 9$ (top) and $T = 11$

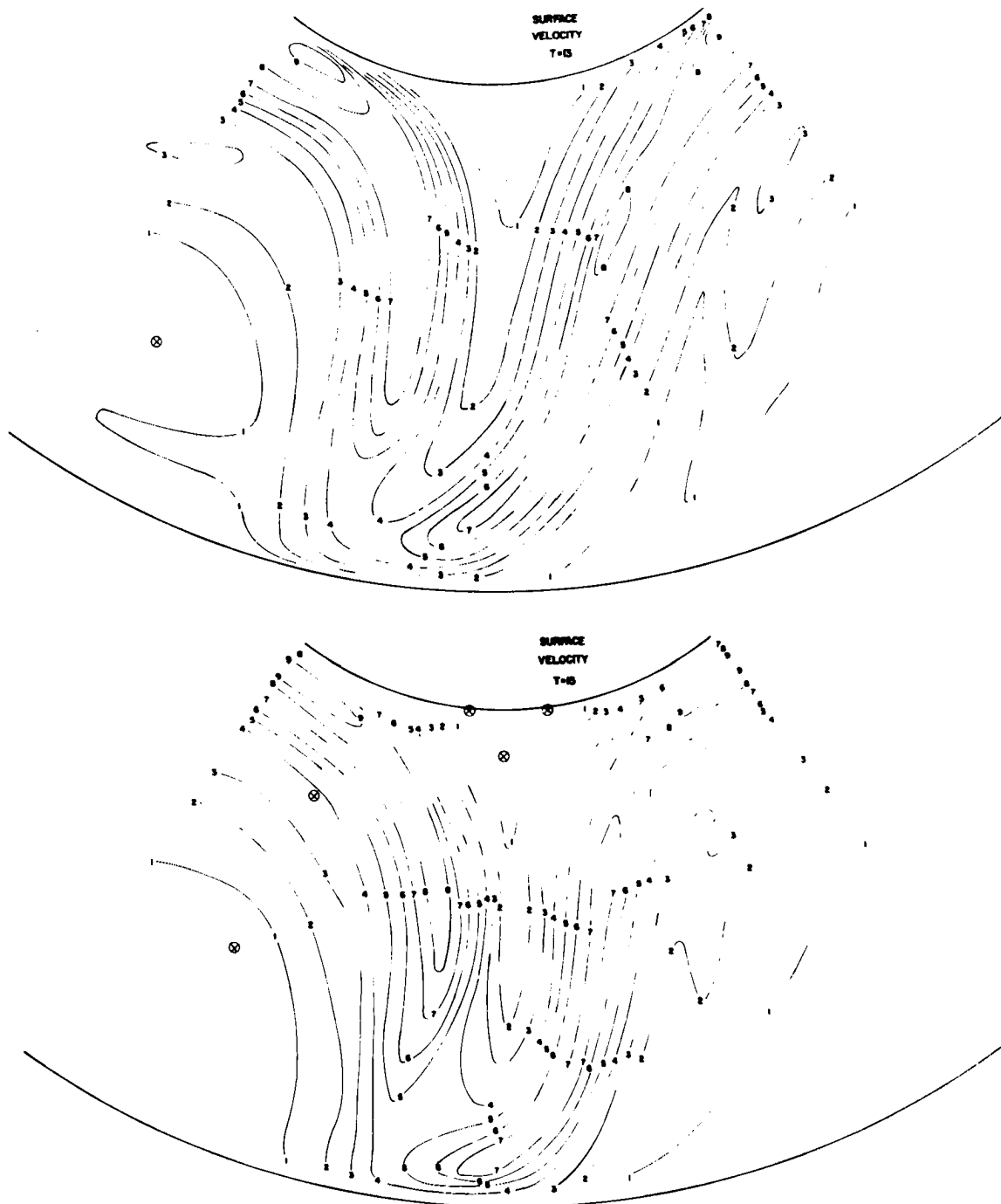


Fig. 2d Same as Fig 2a for $T = 13$ (top) and $T = 15$

wall is a permanent feature, reaching maximum speed in the open wave stage and minimum in the vortex stage of the flow. The surface flow is also marked by strong meridional jets. In the vortex stage, the jet wraps around the vortex with an easterly jet of five per cent to the north and five per cent in a secondary northerly jet on the west.

A second feature of the upper flow important to momentum considerations is evident. When the tilt of the wave axis is northwest-southeast with respect to a radial (north-south) orientation, the eddy flux of westerly momentum is directed outward since the outward flow has a larger westerly component than does the compensating inward flow. Later the tilt becomes northeast-southwest which Starr (1948) suggested was the orientation that large-scale atmospheric eddies assumed in order to transfer westerly momentum poleward (inward). At least in the upper layers, the vacillation has an associated reversal of angular momentum flux. We will later consider the importance of this reversal in maintaining the energy of the large-scale eddies.

Temperature. Measurements sufficient to define the three-dimensional, time-dependent thermal structure, with only a few thermocouples so as not to disturb the flow, require repetition of the experiment. Thus the requirement for closely controlled experiments and highly periodic vacillation. The technique by which a trace from a thermocouple stationary with respect to the annulus is converted to a longitude-cycle phase time diagram, and then to horizontal maps of the thermal field, is given in Appendix A.

Figure 3a shows the meridional cross-section of the overall mean temperature after removal of the mean vertical lapse rate shown

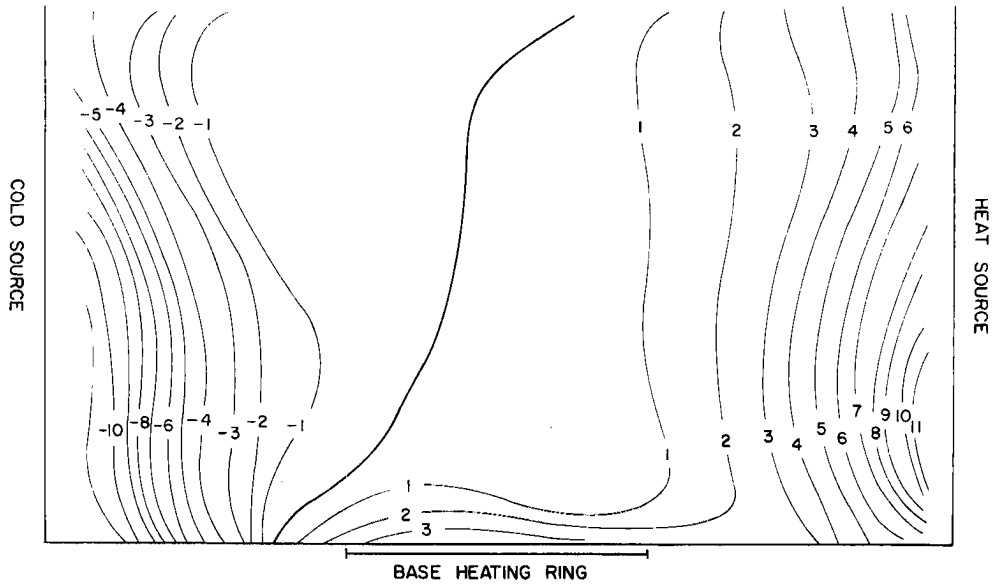


Fig. 3a Deviations (10^{-1}C) from overall mean temperature at each point in the meridional cross-section, after subtracting the lapse rate in Fig. 3b.

OVERALL MEAN LAPSE RATE

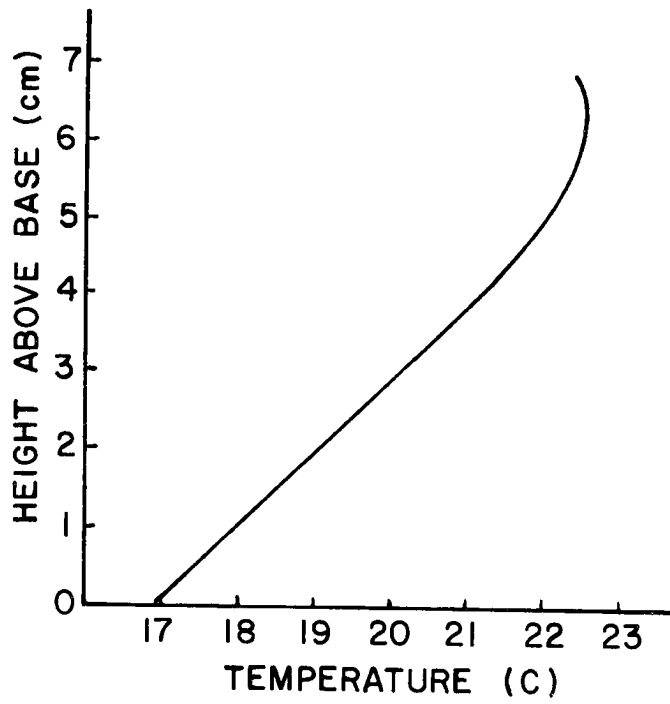


Fig. 3b Time- and horizontal space-averaged lapse rate.

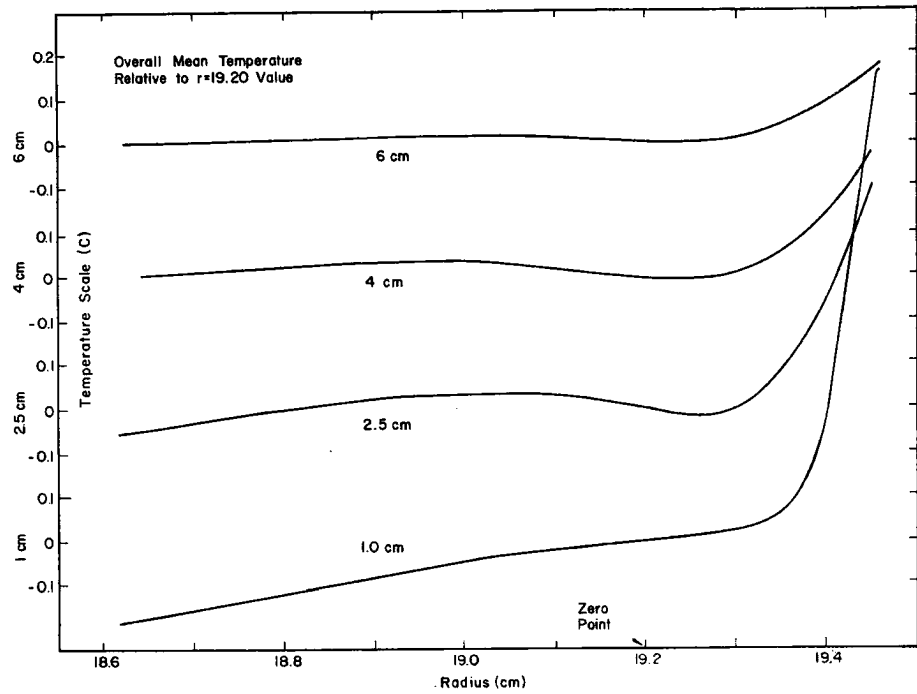
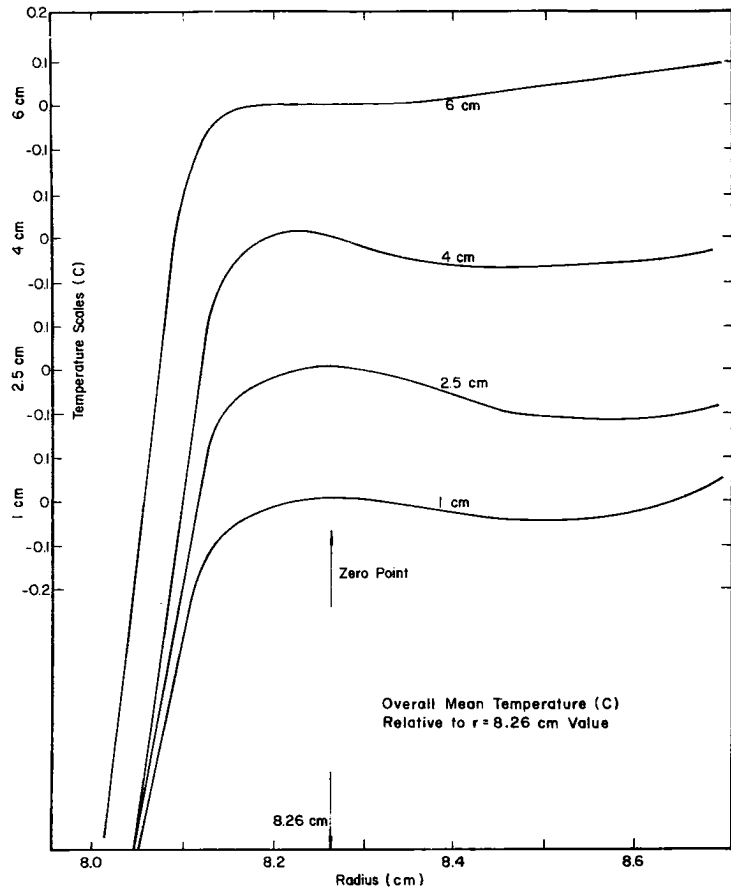


Fig. 4 Temperature, on a sliding scale, normal to the (a) cold, (left) and (b) warm wall at four heights $r_i = 7.825$ cm and $r_o = 19.525$ cm.

in Figure 3b. Over the midradius there is essentially no horizontal temperature gradient, all the gradient being concentrated near both walls. This is a dramatic difference from the atmospheric case, in which large horizontal temperature gradients exist throughout the middle latitudes. Regardless of this important difference, the jet streams in the annulus and in the atmosphere have comparable velocities in non-dimensional units.

Glass lids placed over the annulus reduced, but did not completely eliminate, the evaporation from the top surface. In the large anticyclonic regions with small velocities, the water is strongly cooled at the surface and results in an unstable mean lapse rate near the top. Ink traces in this layer appear to remain laminar, although with stronger evaporative layers, turbulent eddies are sometimes observed.

An important feature of the temperature field which does not appear in Figure 3a occurs near both walls. Figures 4a and b show the detailed temperature structure at the inner (cold) and outer (warm) walls. The double structure of the boundary layer is clearly shown in these overall time-averaged temperature values. A similar structure appears in the analytic (Hunter, 1967) and numerical (Williams, 1967) treatments as well as experimental observations of the symmetric regime. The secondary minimum near the cold wall can only be the result of up motion and it was this observation which prompted the use of a boundary condition of zero vertical motion in this region.

Figure 5 shows the temperature difference at $z = 2.5$ cm between $r = 8.20$ and 8.46 cm as a function of space λ and time t .

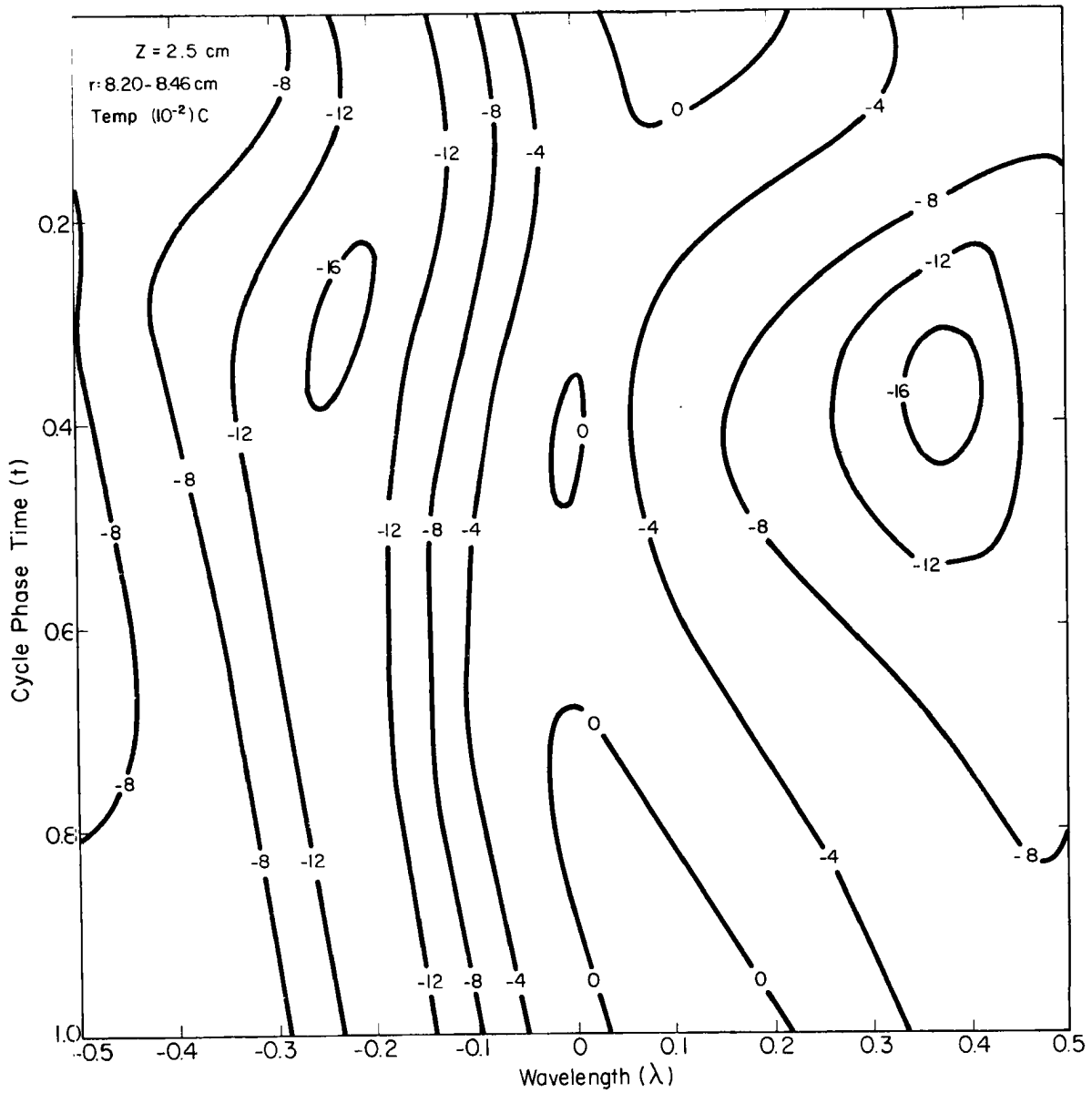


Fig. 5 Wavelength (λ)-cycle phase time (t) diagram at $z = 2.5 \text{ cm}$ for the temperature difference (10^{-2} C) between $r = 8.20 \text{ cm}$ and 8.46 cm . Negative values indicate colder water at 8.20 cm .

Although the overall mean temperature difference is negative (colder at 8.20) as is shown in Figure 4a, near $\lambda=0$ the difference is slightly positive, and a variation with time is evident. Consequently a maximum in the temperature profile would not be observed near $\lambda=0$ at this level. It is thus questionable whether the use of a boundary condition of zero vertical motion in this region is acceptable. However a complete treatment to determine the three-dimensional velocity structure in this secondary boundary layer would involve many data points and a more complex treatment than was felt to be warranted.

An important distinction between this case and the three-wave and symmetric cases is that the mean vertical lapse rate is $1^{\circ}\text{C}/\text{cm}$ compared with $2^{\circ}\text{C}/\text{cm}$ in the others. This appears to be mainly due to the difference in the method of heating since the total heat input is nearly the same. In the previous cases the heating was entirely at the outer vertical wall, but heating at the bottom leads to a less stable lapse rate. The actual lapse rate must be a balance between the externally forced lapse rate and internal adjustments due to convection. With the higher rotation rate, horizontal convection becomes more dominant and also contributes to reducing the mean stratification.

Horizontal temperature maps for cycle times at which we have analyzed surface velocity data are constructed by selecting the temperature data at the same cycle time from all $(\lambda-t)$ diagrams at a given z . Since temperature values at adjacent radii were separately obtained in different experiments, some smoothing was required.

Temperature fields were constructed for 11 heights ranging from 0.1 to 6.9 cm, and at the eight cycle phase times corresponding to the surface isotach analyses shown in Figure 2. Not all of these can be shown, but a representative selection for four heights at four times is shown in Figures 6a to d.

A striking feature of these temperature fields is the small horizontal temperature gradients. In the three-wave case, a range of 3 to 6 C was present over the horizontal surfaces. Here isotherms range over only 1 C at the top to 2 C near the bottom. Association of these isotherms with the surface isotachs (Figure 2) is easy since the tilt and amplitude of the patterns are rather parallel. This has important implications for the horizontal eddy heat transfer which depends on the phase lag between streamlines and isotherms.

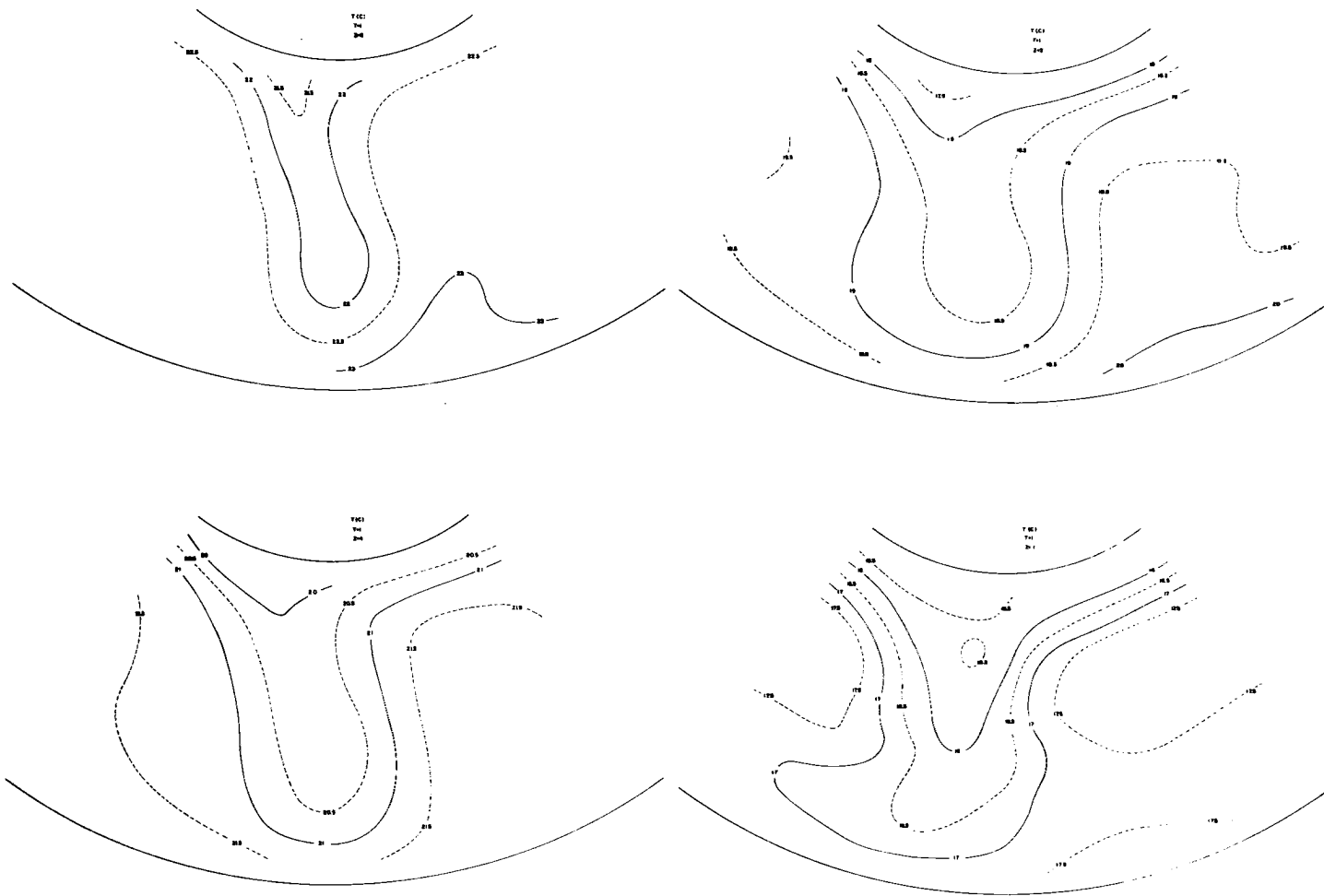


Fig. 6a Horizontal temperature fields at $T = 1$ for $z = 6$ (upper left), 4 (lower left), 2 (upper right), and 0.1 cm. Full lines are 1°C intervals; dashed, 0.5°C intervals.

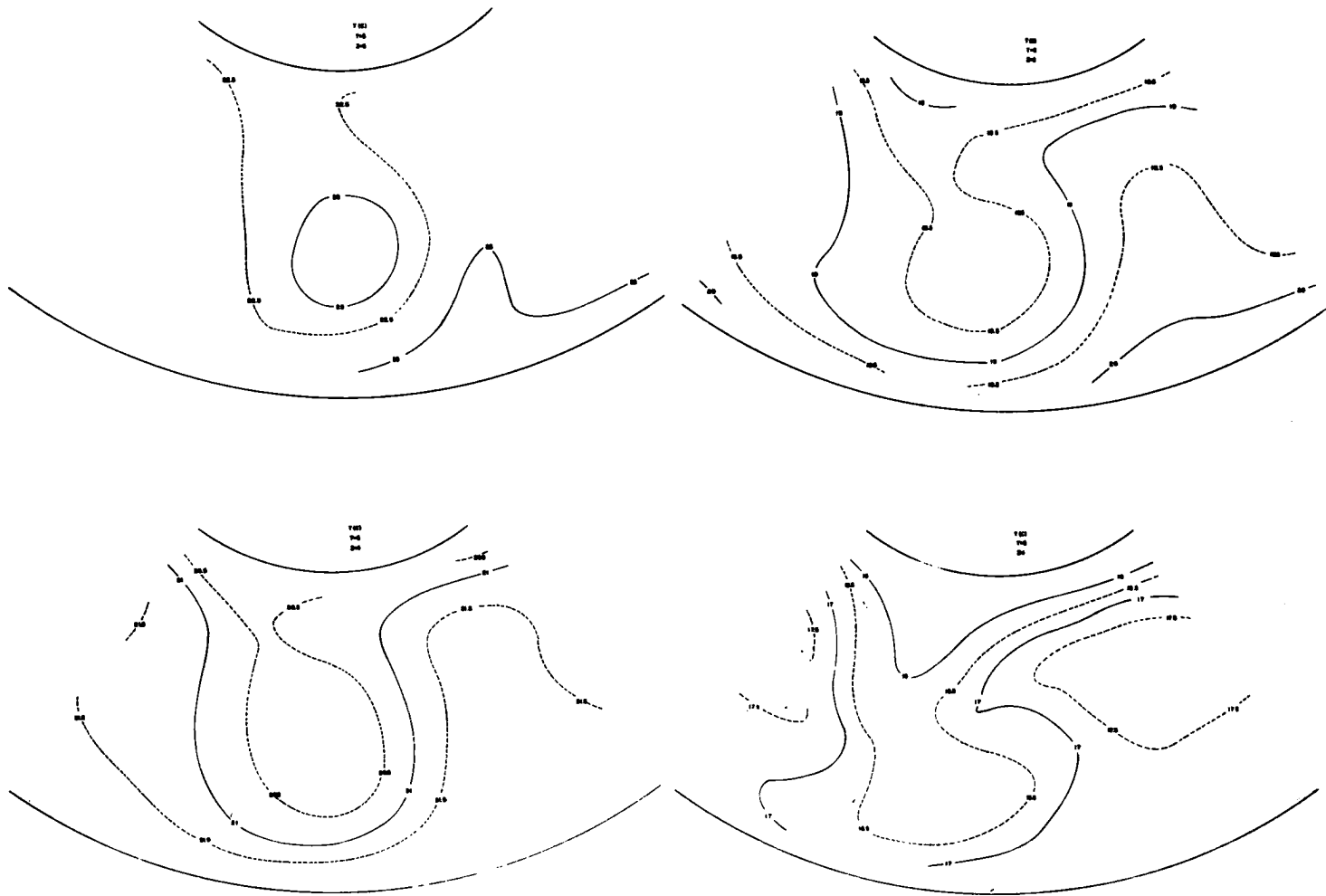


Fig. 6b Same as Fig. 6a at $T = 5$

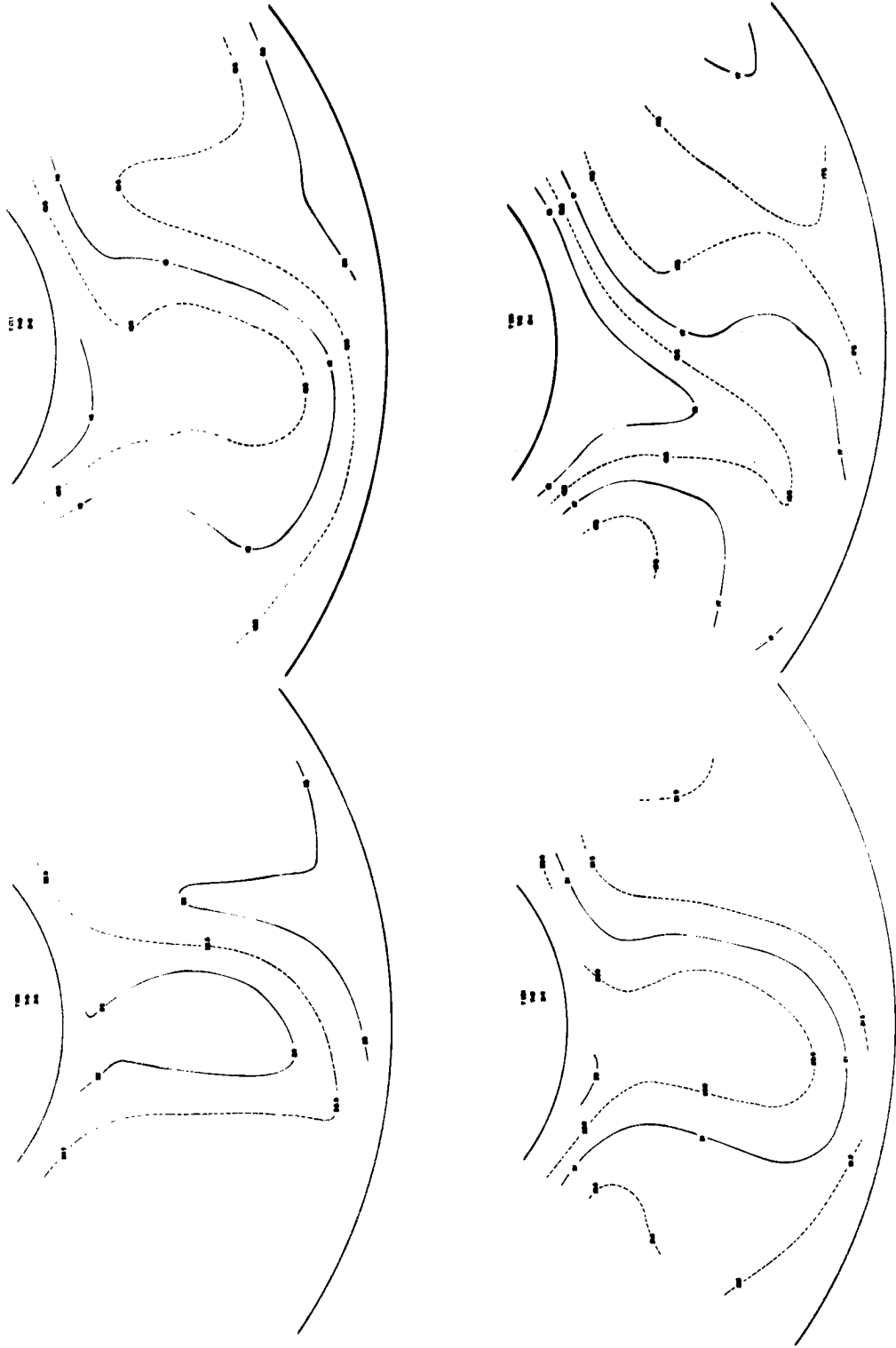


Fig. 6c Same as Fig. 6a at $T = 9$

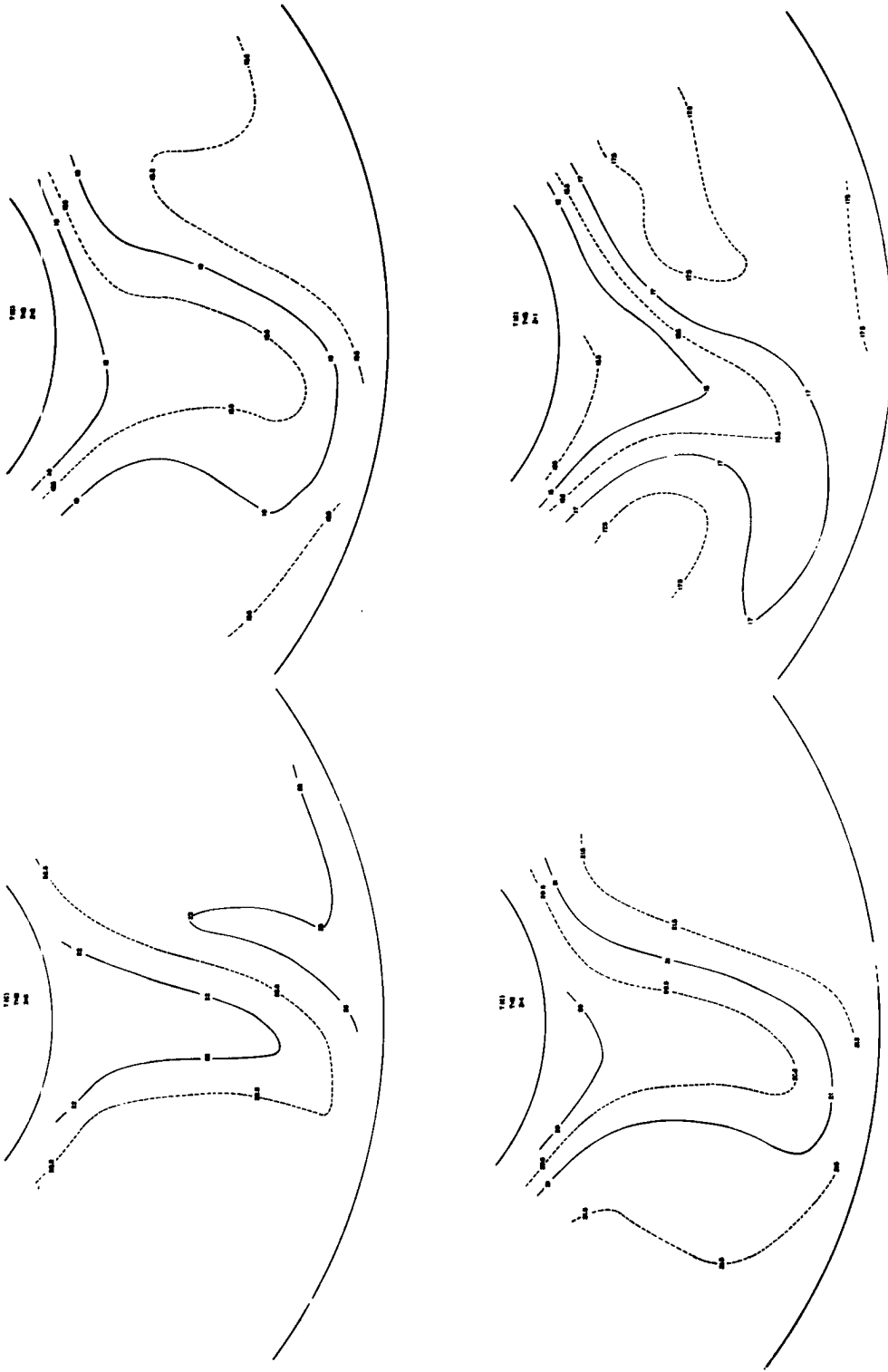


Fig. 6d Same as Fig. 6a at $T = 13$

PART A. STRUCTURE OF THE FLOW

CHAPTER III

TOPOGRAPHY OF TOP SURFACE

Following Riehl and Fultz (1957) we compute the vertical pressure distribution using the three-dimensional temperature field once the surface configuration is computed from the surface velocities. Since the vertical velocity is very nearly zero at the top surface, our knowledge of the horizontal velocity is sufficient to compute all the terms in the complete horizontal equations of motion except the desired pressure term and those frictional terms involving derivatives with respect to height. Measurements in the Ekman boundary layer at the top surface are sufficiently difficult that no quantitative ones have been attempted. We then must choose between equations ignoring only the boundary layer effects, or modify Hide's (1964, 1965) equations for this boundary layer, at the cost of neglecting the inertial terms compared to the Coriolis term. Since the ratio of these terms, the kinematic Rossby number, is small, we choose to neglect the inertial terms.

Hide (1964) solved the boundary layer equations for the vertical variation of the velocity components. Assuming the baroclinic interior flow is geostrophic, and the surface stress-free, the resulting solutions are similar to Ekman solutions (see Appendix B). Both the three-wave and symmetric experiments indicated that the top surface was not free, the air above the water exerting a drag on the surface. Possible contributions from surface viscosity in the presence of surface-active agents are not known. From Väisänen's (1961) published momentum balance we can obtain a value for the drag coefficient

($C_D = 0.01$). Including the effect of a stress at the surface changes only the boundary condition on Hide's solution. As the actual vertical variation represented by this solution is not important to the present discussion we leave the details to Appendix B. The velocity components evaluated at the surface are a function of the pressure force and the turning in the boundary layer due to baroclinic and frictional effects. To then solve for the pressure height h field by relaxation techniques, we take the cross derivatives to form the Laplacian of h . From

Appendix B the resulting equation in non-dimensional form is

$$\nabla^2 h = \frac{2\Omega}{g} \zeta - \frac{\delta^*}{2\alpha} \nabla^2 \alpha - \frac{C_D}{g\delta^*} \{-V(\zeta - D_h) + (v_\theta - v_r) \frac{\partial V}{r\partial\theta} + (v_\theta + v_r) \frac{\partial V}{\partial r}\}_{D=0} \quad (1)$$

where $\nabla^2 = \frac{\partial^2}{\partial r^2} + \frac{\partial}{r\partial r} + \frac{\partial^2}{r^2\partial\theta^2}$, $\zeta = \frac{\partial v_r}{\partial\theta} - \frac{v_\theta}{r} - \frac{\partial v_\theta}{\partial r}$ is the relative

vorticity, $\delta^* = (\frac{v}{\Omega})^{1/2}$ is the Ekman depth, α is specific volume,

$C_D = 0.01$ is the drag coefficient, $D_h = \frac{1}{r} \frac{\partial(v_r r)}{\partial r} + \frac{\partial v_\theta}{r\partial\theta}$ is the two-

dimensional divergence, and $V^2 = v_\theta^2 + v_r^2$ is the square of the total

velocity relative to the pan. This and the following equations are

made non-dimensional using the technique of Fultz, et al (1959).

A balance between the term on the left and the first on the right

would denote geostrophic balance. The second term on the right is the

baroclinic or thermal wind turning, and the last is the frictional

stress contribution. All terms on the right side of this equation

are known and standard relaxation methods of solution may be used

once the boundary conditions on h are specified.

Figure 7 shows the grid on which the solution was obtained.

Since the grid repeats from one wave to the next, a cyclic boundary

condition may be used along the radial boundaries. Along the first

row of grid points adjacent to the walls, $\frac{\partial h}{\partial r}$ determined from the

velocity and temperature fields with the analytic solution for v_θ

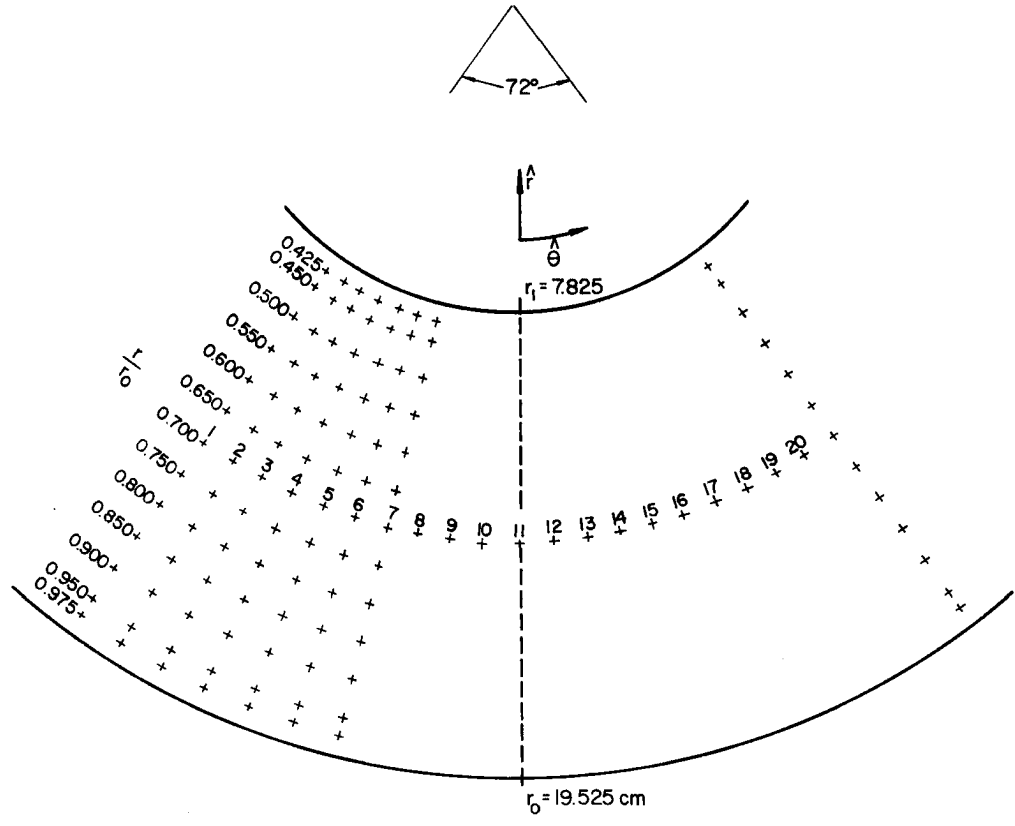


Fig. 7 Horizontal grid over one wavelength. Note the orientation of the r, θ coordinates.

(see Appendix B) is the required boundary condition for the relaxation solution:

$$\frac{\partial h}{\partial r} = \frac{2\Omega}{g} v_{\theta} - \frac{\delta^*}{2\alpha} \left\{ -\frac{\partial \alpha}{\partial r} + \frac{\partial \alpha}{r \partial \theta} \right\} + \frac{C_D}{g \delta^*} \{v_{\theta} V + v_r V\}$$

Relatively small deviations from geostrophic flow are shown by the height contours (not shown) which nearly coincide with the streaks of Figure 1. Thus a balance between only the first two terms in the equation would be adequate over most of the surface. In the region of the jet the frictional term is at most 10 per cent of the vorticity term.

One feature of the surface flow which is not represented by the above technique is the observation of mean meridional aluminum powder velocities outward at most radii. The frictional term results in inward drift as would the surface tension, considered by Hide (1965). For the rotation rate in this experiment and with the use of a detergent solution, the additional force due to surface tension is likely to be small. We will show later that outward surface flow is a reflection of a strong indirect cell in the interior of the fluid. Consequently the assumption of geostrophic flow in the interior foregoes any computation of net outward surface flow.

CHAPTER IV

INTERIOR HORIZONTAL FLOW

Having computed the height configuration of the upper surface, and knowing the three-dimensional temperature (specific volume) field we use the hydrostatic equation to compute the height configuration at any interior level. To derive the horizontal flow velocities we use the so-called balance equation.

Given the pressure interval δp between two isobaric surfaces, $\alpha \delta p = -g \delta h$. For standard specific volume α_s , we may write $\alpha_s \delta p = -g \delta h_s$. Eliminating δp and integrating from the top surface down, the height of any constant pressure surface is $h = h_{\text{top}} - \frac{\hat{\alpha}}{\alpha_s} \delta h_s$ where $\hat{\alpha}$ is the pressure-averaged specific volume. Now α_s may be taken as 1.0 and δh_s is the interval between the standard levels. These heights are made non-dimensional by division by r_0 .

In cylindrical coordinates the divergence equation obtained by taking the divergence of the inviscid, horizontal vector equation of motion may be written

$$\frac{d}{dt}(D_h) + D_h^2 - 2J(v_\theta, v_r) - \frac{\partial}{r \partial r}(v_r^2 + v_\theta^2) + \frac{\partial \omega}{r \partial \theta} \frac{\partial v_\theta}{\partial p} + \frac{\partial \omega}{\partial r} \frac{\partial v_r}{\partial p} - 2\Omega \zeta = \alpha \nabla^2 h$$

where $D_h = \frac{\partial v_\theta}{r \partial \theta} + \frac{\partial v_r}{r \partial r}$ and the Jacobean $J(v_\theta, v_r) = \frac{\partial v_\theta}{r \partial \theta} \frac{\partial v_r}{\partial r} - \frac{\partial v_r}{r \partial \theta} \frac{\partial v_\theta}{\partial r}$

and $\omega = \frac{dp}{dt}$ is the vertical velocity in pressure coordinates.

Assumption of geostrophic motion in the interior would imply dropping all but the last two terms. The usual meteorological quasi-geostrophic balance equation retains a term involving the gradient of the Coriolis force, which is zero for this geometry. A more complete form which retains the Jacobean term and the curvature terms will be used here.

That is we neglect the terms involving D_h and ω which are small compared to the remaining terms.

We define the streamfunction ψ by the relations $v_\theta = -\frac{\partial\psi}{\partial r}$ and $v_r = \frac{\partial\psi}{r\partial\theta}$ (where r is positive inward) and noting that $\zeta = \nabla^2\psi$ the balance equation is

$$2\Omega \nabla^2\psi = -g\nabla^2h - 2 J(v_\theta, v_r) - \frac{\partial}{r\partial r} (v^2) \quad (2)$$

With ellipticity conditions comparable to those given by Shuman (1957) for the atmospheric case, this equation may be solved by an iterative relaxation technique. No corrections were necessary at any level to prevent the equation from becoming hyperbolic. The initial guess for ψ was the geostrophic field, and geostrophic flow across the inner (0.425) and outer (0.975) radii specified the boundary conditions there. Successive iterations included better approximations to the Jacobean and curvature terms until only very small changes ψ occurred. Five iterations were judged to be sufficient. A technique for evaluating the Jacobean which also accounts for the variable grid lengths in cylindrical coordinates was derived following Bring and Charasch (1958).

Figures 8a-d show the streamfunction at the levels 6, 4, 2, and 0.1 cm for only $T = 1, 5, 9,$ and 13 . Concentrated streamflow associated with the jet at the surface is evident at $z = 6$ cm. In lower layers this open wave gives way to a closed cyclone under the inflection point of the upper jet. Also in the lower layers the motion is predominantly from the east near both walls. At $T = 5$ a relatively huge vortex extends throughout the fluid, with consequent shrinking of the anticyclonic cells. At $z = 6$ and 4 cm for $T = 9$ the wave tilt is from southwest to northeast, but in the lower layers, the

wave tilt is still northwest-southeast. This continues to be true at $T = 13$, indicating that these lower layers do not go through the large oscillation in wave tilt which typifies the vacillation in the upper layers. The base heat source may help hold the patterns more stationary, which has important implications in the angular momentum balance of the whole wave.

In regions of large zonal velocity the speeds computed from the streamfunctions were checked by releasing dye at 10-20 points for four different times. Because the patterns are time-dependent, measuring the displacements over sufficiently long time intervals introduces space and time location errors. The computed velocities above about one cm depth are within the accuracy of these measurements. It is easier and quicker to check the direction of the dye streaks for transition between easterly and westerly components. These checks and the orientation of the dye streaklines further substantiate the flow patterns illustrated by the streamfunction fields.

It should be noted that the vertical variation of the streamfunction and the location of the cycle relative to the upper level flow are in agreement with the structure of atmospheric disturbances. The most significant difference lies in the strength of the low-level easterlies on the outer side of the high pressure cell. Riehl and Fultz (1957) found easterlies over the entire bottom which they related to the pattern at perhaps 1,200 mb in the atmosphere. We now compute the vertical motion as a further check on the analogy between laboratory and atmospheric circulations.

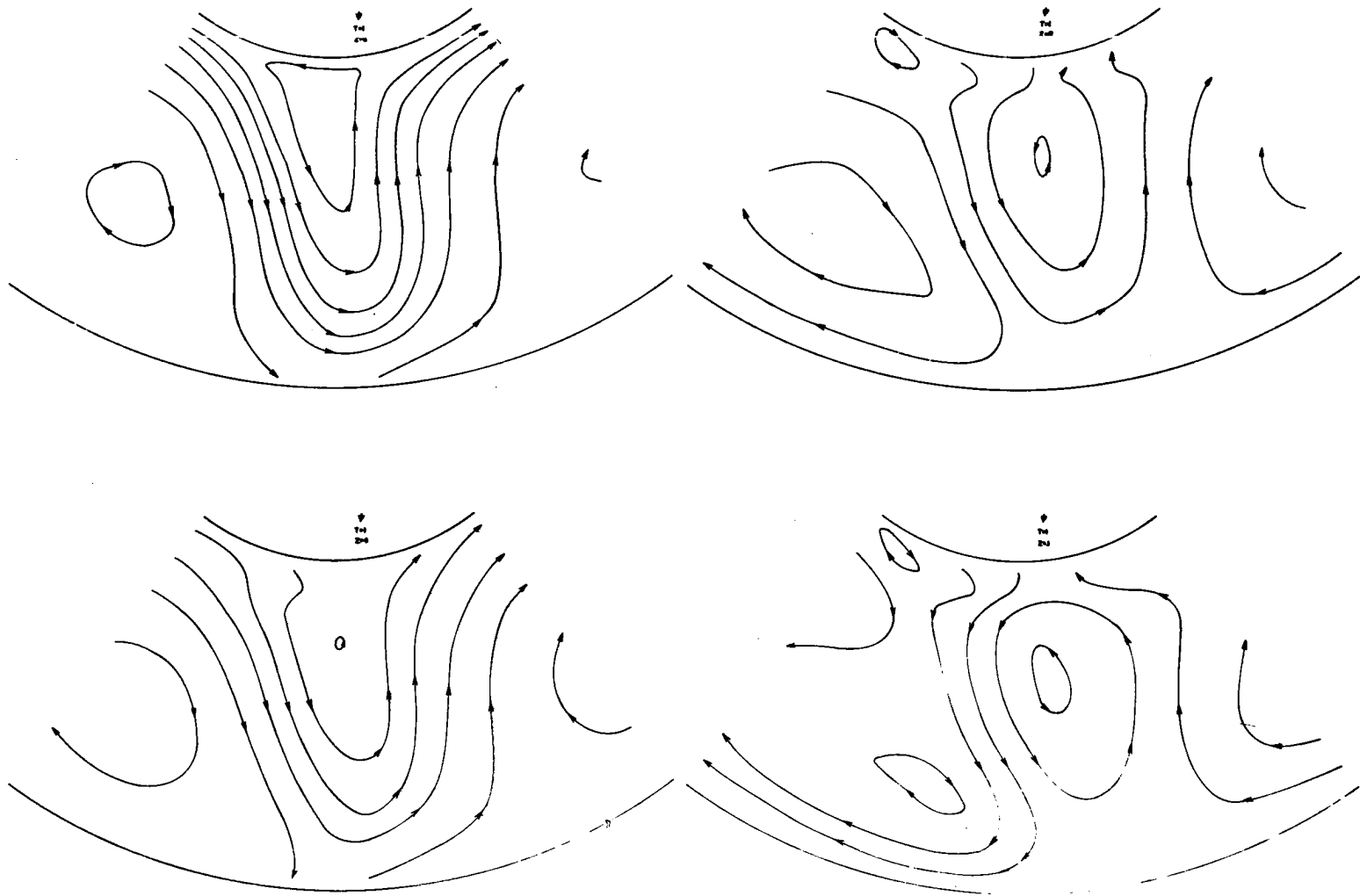


Fig. 8a Streamfunction at $T = 1$ for $z = 6$ (upper left), 4 (lower left), 2 (upper right), and 0.1 cm.

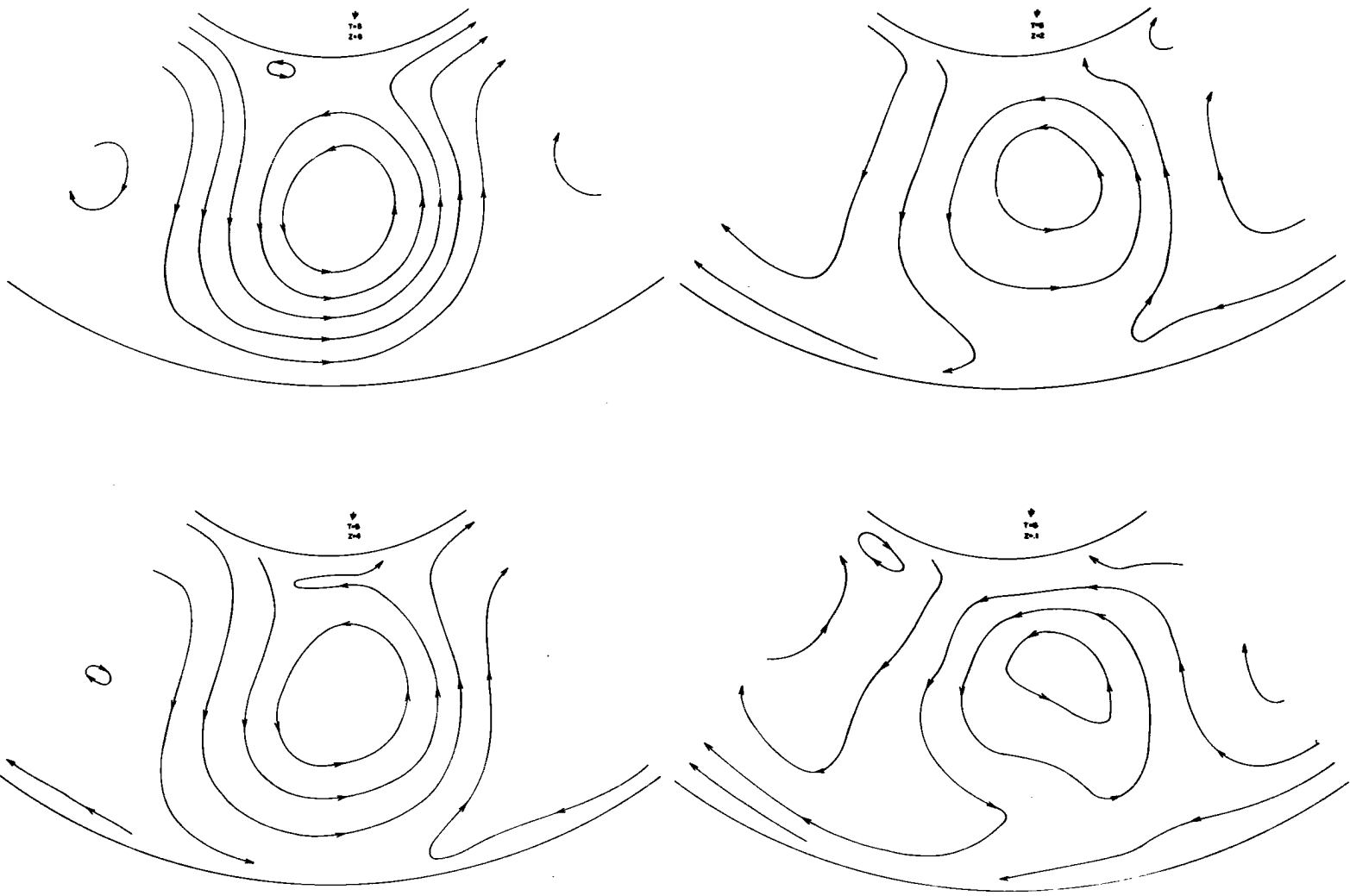


Fig. 8b Same as Fig. 8a at $T = 5$

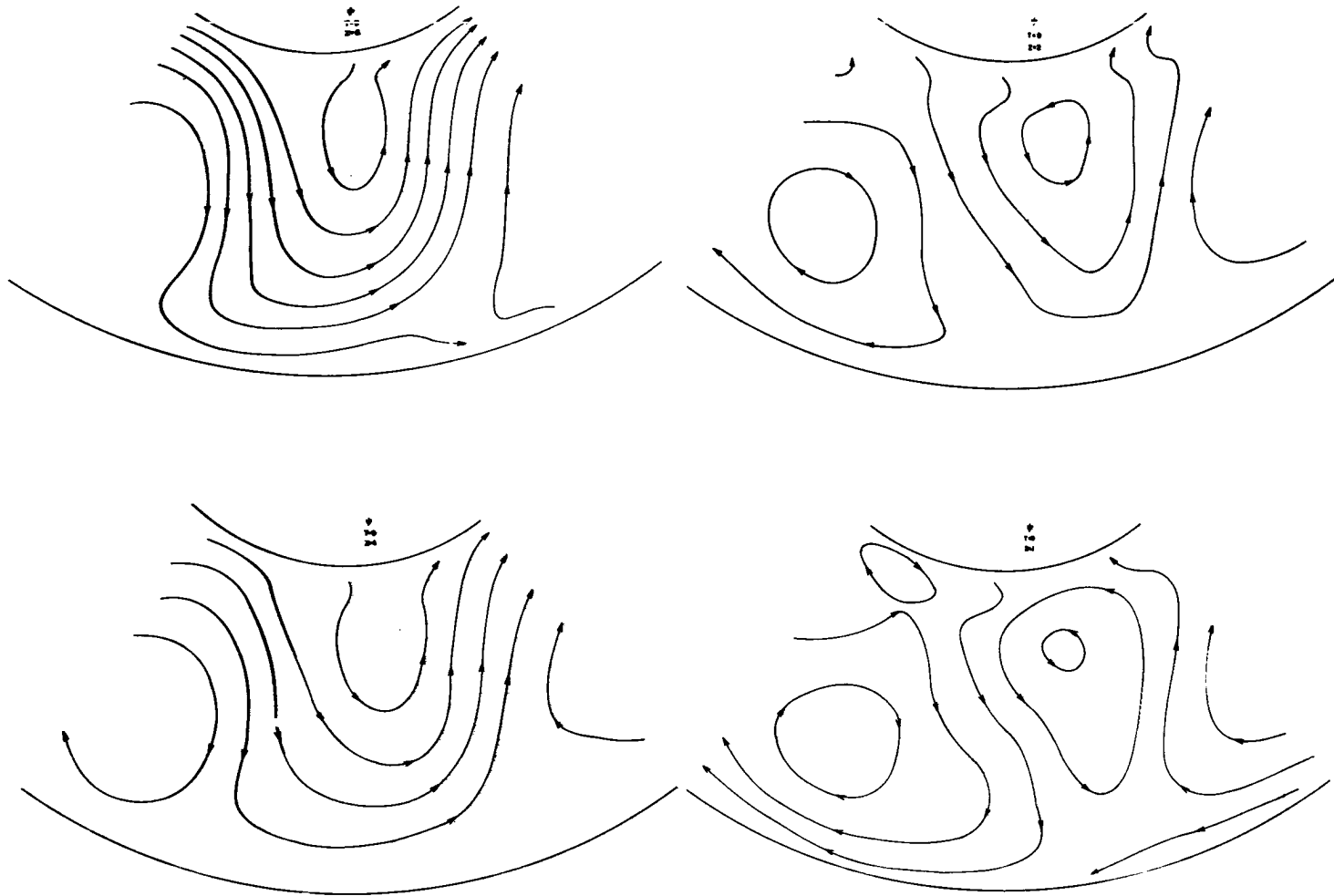


Fig. 8c Same as Fig. 8a at $T = 9$

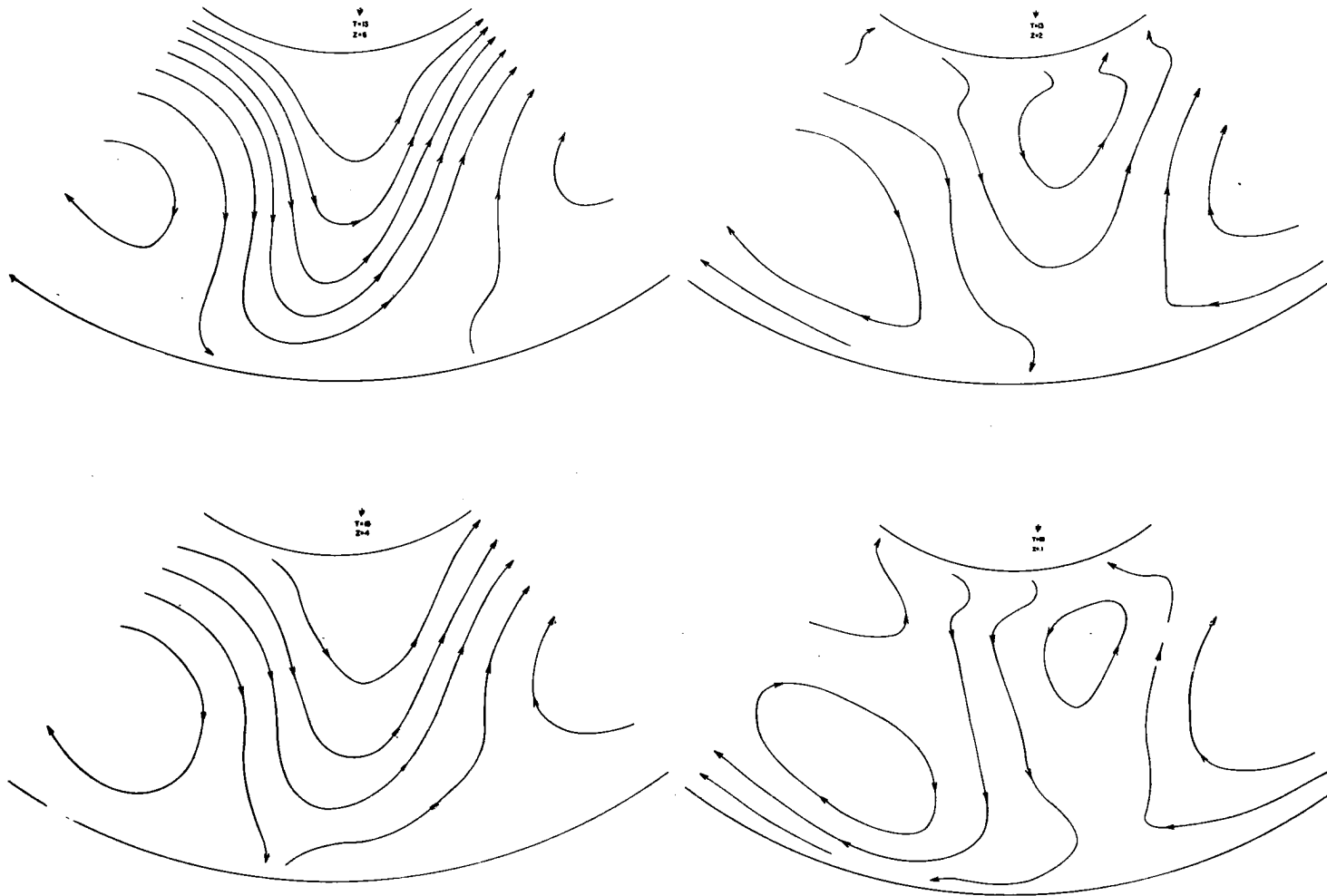


Fig. 8d Same as Fig. 8a at $T = 13$

CHAPTER V

VERTICAL MOTION

Riehl and Fultz (1957) computed the vertical motions with the assumption of conservation of heat, in that case, temperature.

Because the three waves were steady this reduced to a statement that horizontal and vertical components of temperature advection must balance. Along isentropic (isothermal) surfaces the horizontal velocity components along the gradient of the Montgomery streampotential have to be balanced by vertical motion to maintain the stationary isotherm pattern.

In the present case the isotherms are not stationary and the computation becomes more complex. Furthermore frequent observations of the temperature must be made to determine the time changes. While this is clearly possible from the λ - t analysis of the temperature at each (r,z) , we adopt a procedure in which the time change of temperature is not required. By using the quasi-geostrophic ω equation we use data at only one time. Here ω is the vertical motion in pressure coordinates which may be related to vertical motion w in height coordinates by $\omega = -\rho gw$ where ρ is the density.

The derivation of the complete ω equation occurs in various places in the meteorological literature and the reader is referred to Appendix C for the derivation and other details as to its use in this analysis. Although ψ from the balance equation is used, only the quasi-geostrophic forcing terms in the ω equation are retained. We also assume a linear relation between the specific volume and temperature. The streamfunction was converted to one relative to the wave ψ_c by

subtracting the wave speed in Table 1:

$$\nabla^2(\omega\sigma) - (2\Omega)^2 \frac{\partial^2 \omega}{\partial p^2} = \nabla^2 \{-J(\psi_c, \alpha)\} - 2\Omega \frac{\partial}{\partial p} \{J(\psi_c, \nabla^2 \psi)\} \quad (3)$$

Here $\omega \cdot \frac{dp}{dt}$ and $\sigma \cdot \frac{\partial \alpha}{\partial p}$ which was allowed to vary even though the term which would offset this variation has been omitted from the right side. Once the boundary conditions on ω are specified, three-dimensional relaxation techniques are used with the horizontal grid in Figure 7 at eight equally spaced levels in the vertical.

It is clear that at the top and bottom levels we may specify $\omega = 0$. The coarseness of the vertical spacing ignores the frictional and, at the bottom, thermal boundary layers. Again we use cyclic boundary conditions on the radial boundaries, but other considerations must be used near the walls. At the walls ω is identically zero, but the ω equation does not apply for the intense vertical motions in the boundary layers near the walls.

We showed earlier (Figure 4) that the long-term average temperature showed a minimum/maximum as the outer/inner walls are approached. A theoretical analysis by Hunter (1967) of the boundary layers for the symmetric regime also showed this double structure, as did a numerical study by Williams (1967). It was thus assumed that at some point just outside of each boundary layer, $\omega = 0$. However, a later, more careful experiment showed that the maxima and minima varied with longitude, and cast doubt on the assumption of $\omega = 0$ at each gridpoint adjacent to the inner and outer walls.

Three main features appear for each time in the ω diagrams in Figures 9a-d. These are two maxima of sinking (positive ω) motion and one maximum of upward motion. One center of sinking motion is located



Fig. 9a Vertical motion (negative is upward) at $T = 1$ for $z = 5$ (top) and 2 cm. Units are in mille of the equatorial rim speed.

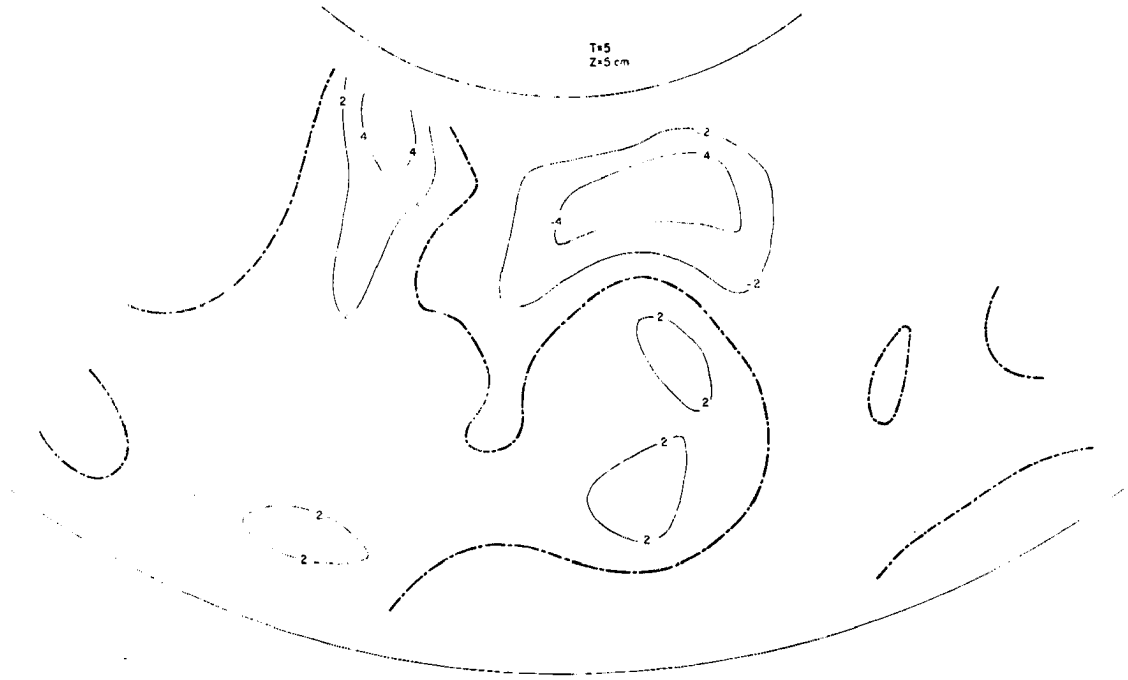


Fig. 9b Same as Fig. 9a at $t = 5$

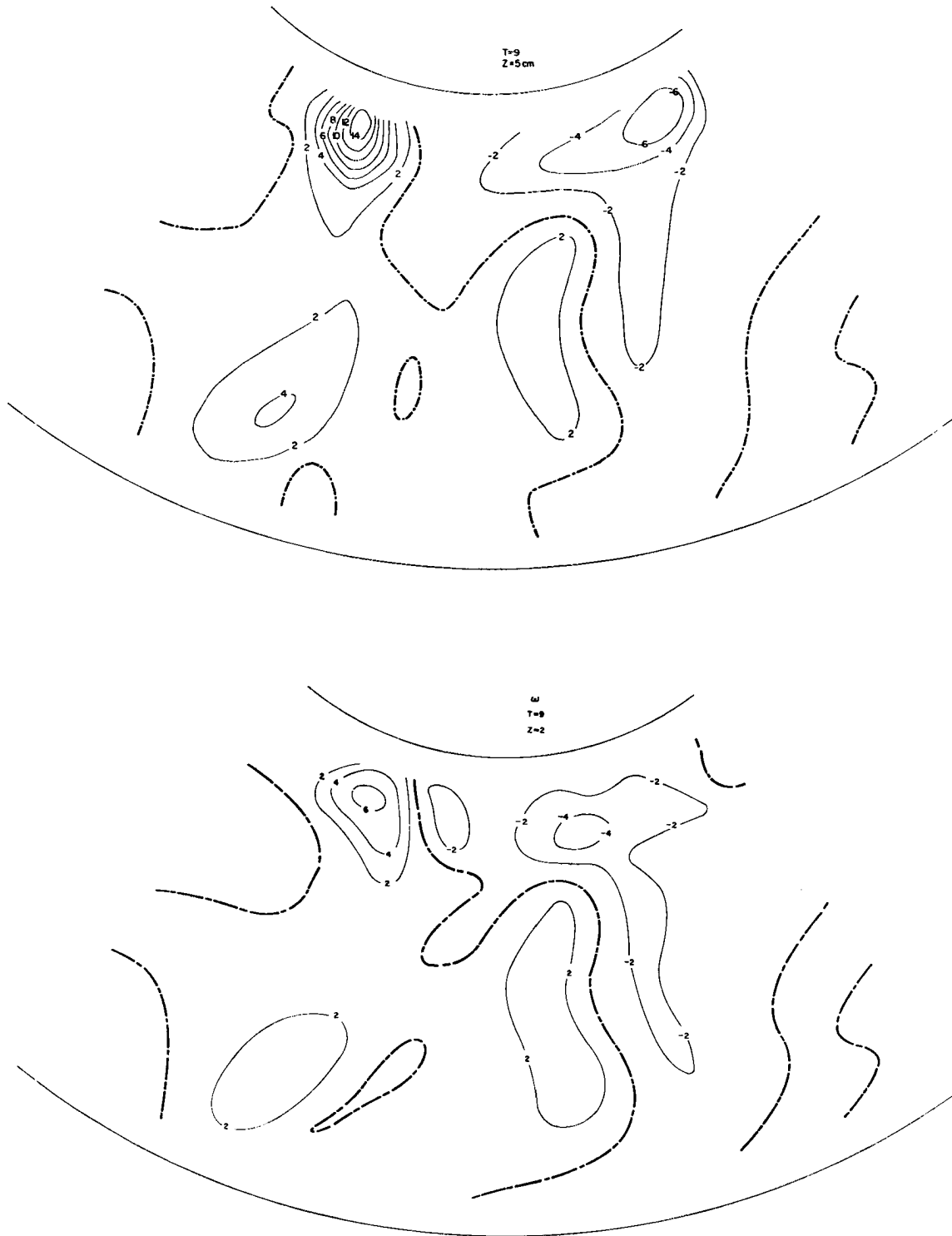


Fig. 9c Same as Fig. 9a at $T = 9$

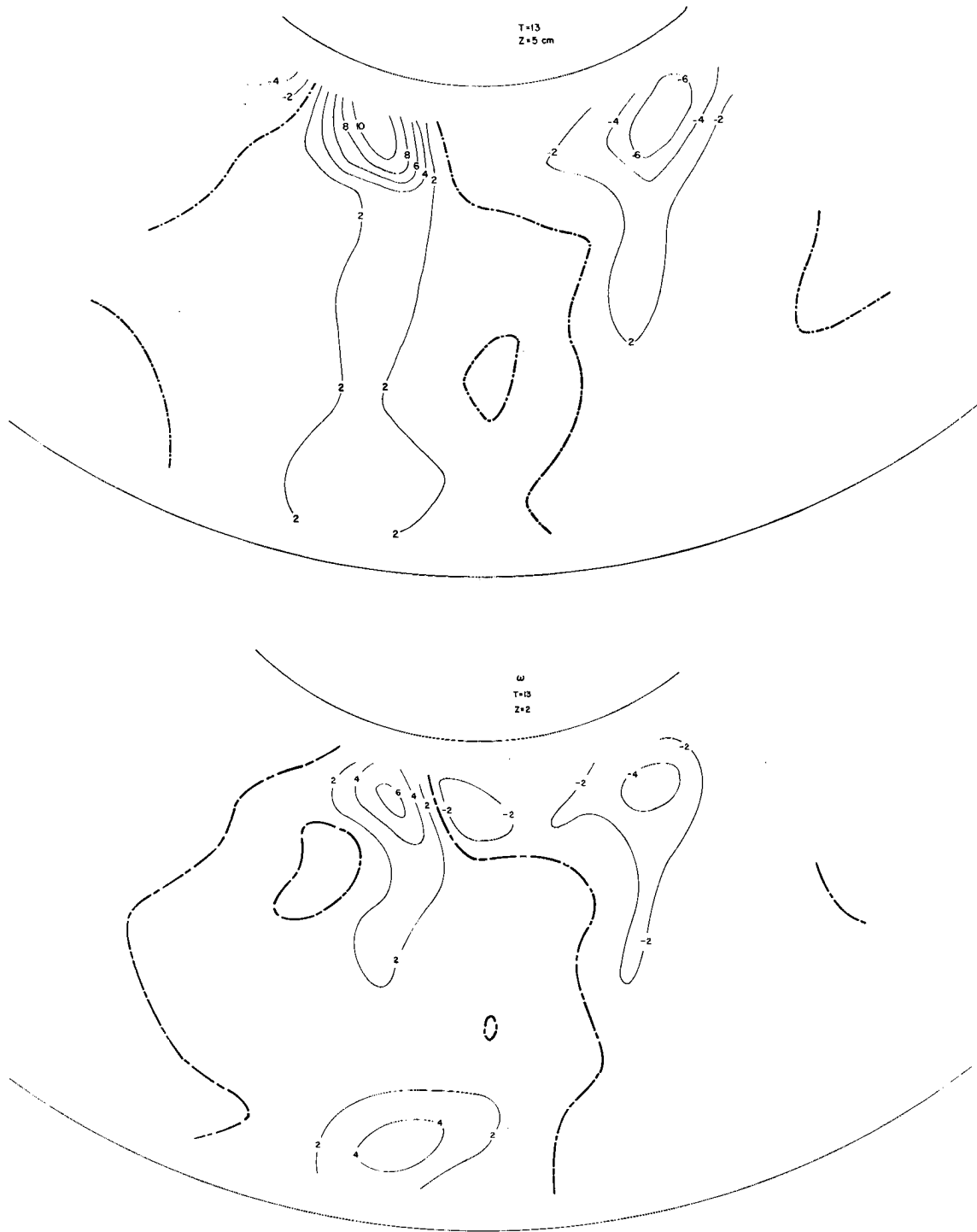


Fig. 9d Same as Fig. 9a at $T = 13$

at the point where the jet flows away from the cold wall. The other two vary in position but are generally in the region of maximum cyclonic (descent) and anticyclonic (ascent) curvature of the jet. Away from the maximum sinking motion near the cold wall, the maximum vertical motions, and thus the level of non-divergence, occurs near mid-depth. With the distribution of vertical motion with respect to the wave, this leads to divergence (convergence) in advance (to the rear) of the wave trough at upper levels.

Thus the patterns of convergence and divergence, locations of maxima both horizontally and vertically, and magnitudes of the vertical motions are analogous to the atmosphere disturbances. To compare numerical values, we need to consider the difference in vertical and horizontal scales between atmosphere (1:1000) and annulus (1:3), as in Fultz, et al (1959). A value of 20 mil of the equatorial speed near the maximum of sinking after division by 333 would correspond to an atmospheric value of 3.0 cm/sec, which is perhaps on the low side.

Divergent part of the velocity. Having computed the vertical motion, we can use relaxation techniques to compute the divergent streampotential χ from the equation of continuity in the form $\nabla^2 \chi = \frac{\partial \omega}{\partial p}$. From the definition of χ the additional radial and tangential components of velocity due to the divergent part of the motion are obtained. Averaged over a wavelength the v_r component does not vanish, leading to a mean meridional motion.

To be consistent with the boundary conditions on ω , we force $\chi = 0$ at the first gridpoint adjacent to the walls. This clearly cannot be true in the mean since the boundary layers would be isolated

from the interior. However we have no information about the divergent radial component v_r along the wall which would be required to specify a gradient boundary condition on χ .

Since the divergence is small, the additional components due to the divergent part of the velocity are generally less than 1 mille of the equatorial speed. Consequently the only important result is the mean meridional motion.

Mean meridional motion. Since $\frac{\partial \omega}{\partial p}$ is evaluated over two vertical gridlengths, only the \bar{v}_r between 1.0 through 6.0 cm could be determined. Having the surface values of \bar{v}_r , the intention was to vertically integrate the \bar{v}_r profile to determine the value just above the base since the mass must be conserved. However the surface values profiles were sporadic and could not be matched with the mean vertical motion and the corresponding \bar{v}_r value at 6.0 cm. Just as in the atmosphere the errors in measuring the velocities are of the order of the mean meridional component. Therefore the requirement for a heat balance in the layer was used to determine the mean mass flow in the layer 6-7 cm, and thus also specify the flow between 0.1 and 1 cm. This calculation is discussed in Appendix D.

Figure 10 shows some examples of the Stokes streamfunction Ψ which is defined by the relations $\bar{v}_r r = \frac{\partial \Psi}{\partial z}$ and $\bar{w} r = \frac{\partial \Psi}{\partial r}$ in non-dimensional units. Of course the computation does not extend into the boundary layers, where the strong vertical motion is indicated by the double arrows. The three cell structure of the flow is then evident, with varying intensity of direct, as well as the indirect, cells.

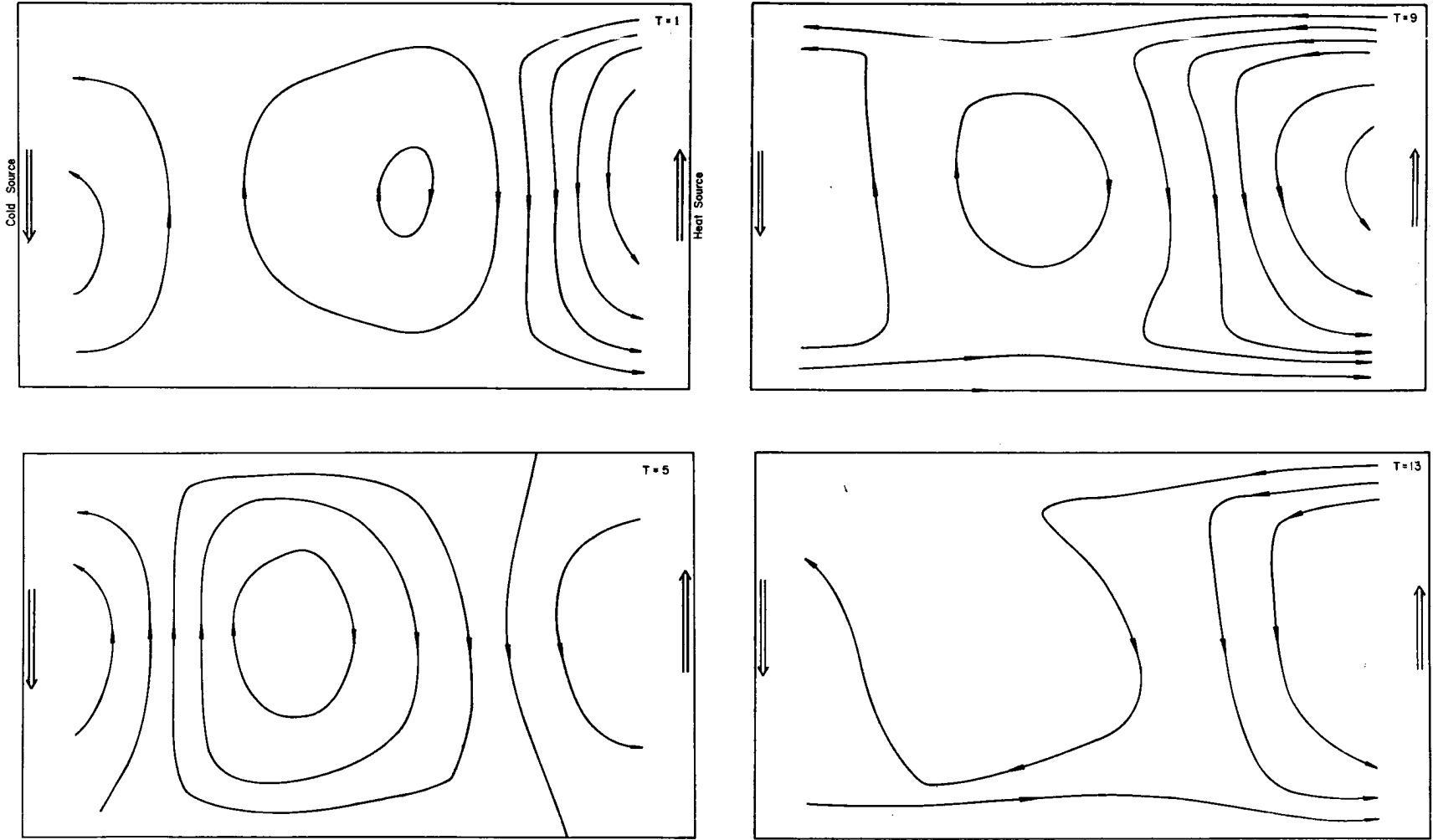


Fig. 10 Stokes streamfunction of the meridional circulation. Double arrows indicate the strong vertical motion in the boundary layers (a) $T = 1$, upper left, (b) $T = 5$, lower left, (c) $T = 9$, upper right, and (d) $T = 13$.

The inflow all along the top and outflow all along the bottom at $T = 9$ is entirely due to the assumption of heat balance for the derivation of the mass flow in these layers. But since it is only the gradients which enter, the circulation in the interior is not affected by the calculation in the top layer. Although these diagrams must be regarded as tentative until verified by the attainment of heat and energy balances, the nature of the mean meridional circulation with its three cell pattern in the interior is established.

PART B. GENERAL CIRCULATION

After examining the various aspects of the structure of the waves in the annulus, we have noted basic similarities as well as important differences. In the introduction it was noted that the surface velocities in the jet were equivalent to those of a moderate atmospheric jet stream if both are scaled in terms of the equatorial speeds. In subsequent sections we showed that when a complete and consistent set of scale parameters (Fultz, et al, 1959) was used, other features of the kinematic structure computed from the balance equation were also analogous. A significant difference was the strong easterly currents along the base near both walls.

The strong thermal boundary layers near both walls, as well as the small temperature gradients in the central part of the fluid are significant deviations from the baroclinic structure of the atmosphere. The vertical motion in the vertical boundary layers of course has no counterpart in the atmosphere. However the magnitude of the vertical motion in the interior, and the resultant patterns of convergence and divergence are quite analogous. We now try to explain the mechanisms by which a system which is grossly similar to atmospheric waves, can vary in periodic manner, and the influence of the dissimilarities on these mechanisms.

CHAPTER VI
HEAT BALANCE

One of the requirements which the fluid motion must satisfy is the transfer of heat from the sources at the outer cylinder and at the base. Neither the spatial distribution nor the exact amount of heat supplied by each of these sources is known, and in part the fluid determines this heat flow by its very changes in structure. Indeed this feedback between the flow structure and the heat sources is no doubt an important feature in explaining the cycle through which the flow vacillates.

Nominal strength of the outer and base sources are 80 and 15 watts, respectively. As was noted earlier, evaporation occurs in the top layer, a cooling of 4.7 watts was estimated from the net loss of water over the length of the experiment. Thermocouples in the cold source measure the difference between incoming and outgoing water and thus the total amount of heat transferred by the fluid motion is computable.

Introducing the bar operator for the azimuthal average around the entire cylinder, and a prime for deviations from this zonal mean, we may write the heat balance equation as

$$2\pi \iint \frac{\partial \bar{\tau}}{\partial t} r dr dz + 2\pi \int_2 (\bar{v}_r \bar{\tau} + v_r' \tau') r dz + 2\pi \int_2 (\bar{w} \bar{\tau} + w' \tau') r dr = 2\pi \iint \bar{Q} r dr dz \quad (4)$$

using non-dimensional quantities τ for temperature and Q for the rate of heat addition. Here the subscript 2 on the second and third terms indicates two vertical and horizontal surfaces are implied in this integration. It can be shown that away from the thermal boundary layers, the molecular conduction terms are negligible. In this

formulation the roles played by the mean meridional circulation and the quasi-geostrophic eddies are distinct. In the latter there is no net mass flow across the surface, but heat is transferred by virtue of inflowing and outflowing masses having different temperatures.

In principle all the terms on the left in the above equation can be computed, at least down to volume sizes bounded by the grid-points in the meridional plane. Away from the boundaries of the fluid there is no heat source (a considerable simplification from atmospheric flows where radiational and latent heat sources are present internally), and the balance on the left should be achieved. In the volumes adjacent to the boundaries, the heat addition/extraction will be a residual. However we shall see that it was not possible to carry out the latter computation since the terms on the left are not sufficiently well-known as to give more than a qualitative estimate of heat sources.

Cycle mean heat balance. To illustrate the unbalance of the computed terms on the left-hand side of the heat balance equation, we also average each of the terms over the cycle so that the time change term goes out. Figure 11 shows the cycle mean heat balance. Eddy terms are represented by the right (lower) arrows on the horizontal (vertical) surfaces. Since mass balance is enforced, we only list the mean heat transport above a base value represented by the mean mass flow through the side times 273.16. That is we use mean zonal temperatures in Celsius units rather than Kelvin.

Looking first at the boxes (actually annular rings) in the interior of the fluid, we see that the unbalance represented by numbers enclosed by the smaller boxes is consistently positive near

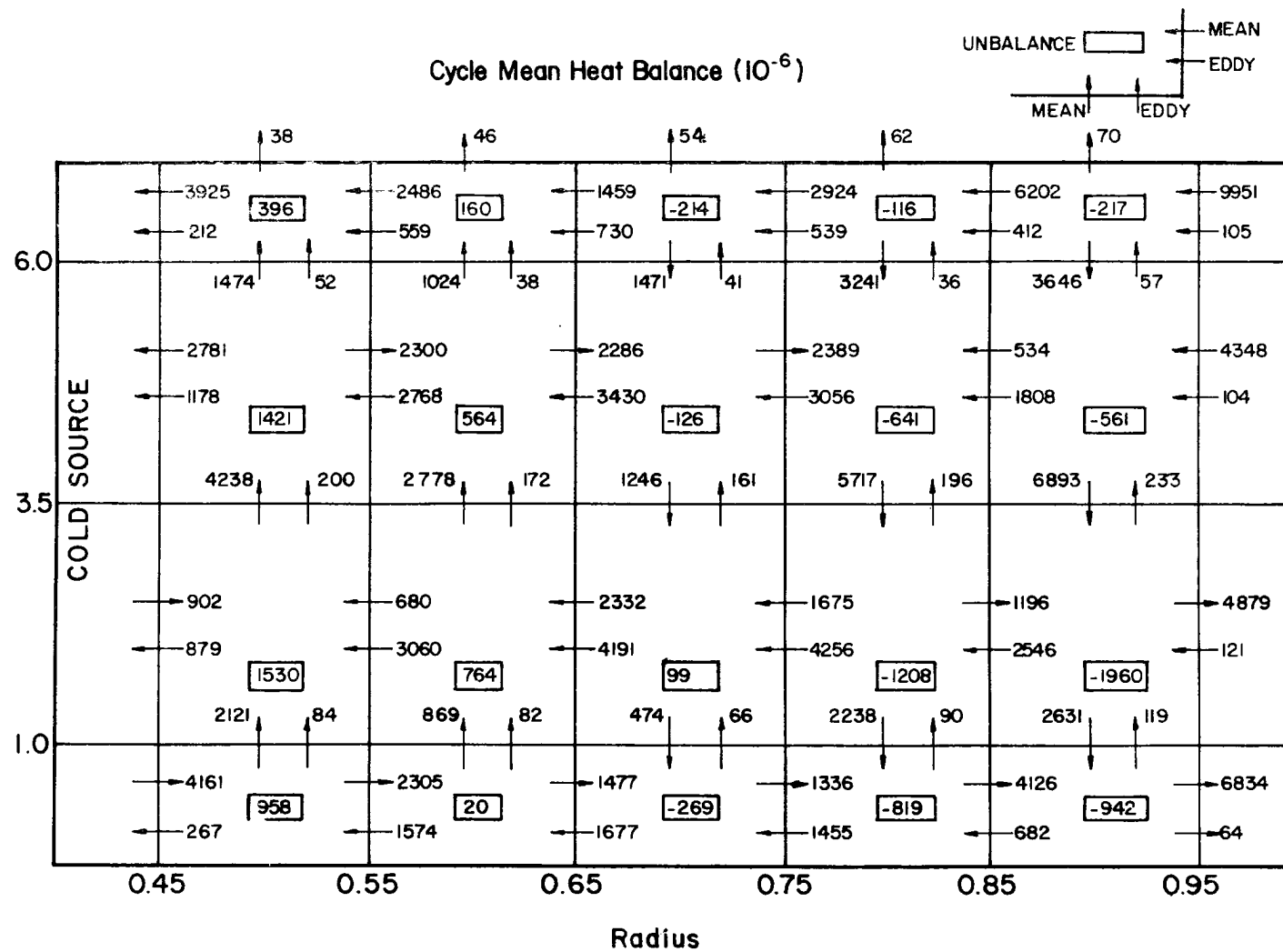


Fig. 11 Heat balance averaged over one vacillation cycle. For description of the arrows see model at upper right. Convert to watts by multiplying by $15.8 (10^3)$.

the cold source and negative near the heat source. The meridional circulation is arranged in such a way as to lead to convergence of heat at outer radii where the eddies lead to divergence, and vice versa in the inner regions. However the unbalance is, in nearly all boxes, such that the mean motion contribution is insufficient to offset the eddy term. As the eddy term is likely to be quite reliable, this pattern is a clear indication that the strength of the meridional cells is strongly underestimated. Since the horizontal and vertical mean flows are coupled by mass balance, the heat balance computed in the top layer in Appendix D must also be in error since it utilizes mean vertical mass and heat flows based on the computed $\bar{\omega}$ at 6.0 cm.

In the interior the mean radial flow was computed from the vertical motions (ω equation) using a divergent streampotential. First, the main source of error was likely to be the boundary condition on this streampotential which allowed no flow through $r = 0.425$ and $r = 0.975$. These are the radii with the largest radial mass flows since the direct cells must transfer the heat away from the heat source and to the cold source as the eddy term tends toward zero. Secondly the equation was simplified by omitting the effects of Ekman boundary layers at the top and bottom, and especially over the base heating ring. These effects acting over relatively thin layers induce vertical motions which should have been included.

Although the vertical motion calculation failed to satisfy the interior balance requirement, we do wish to examine the role played by eddies and mean motion in accomplishing the heat transfer. We adopt two approaches: in the first we assume that the calculated \bar{v}_r values are partially correct, and increase the strength of the

three cells to account for the vertically integrated unbalance between constant radii. All of the unbalance is then placed in an additional mean meridional motion. In the second we assume that the heat sources at the outer wall and the base are constants given by their nominal values and compute the heat transfer at the inner wall.

Additional mean meridional motion. We take the inner position of the direct cell near the outer rim heat source as being correctly given by the computed \bar{v}_r reversal in sign. Then setting the correction to the vertically integrated heat transfer to be zero at that position and accumulatively adding the unbalances in both directions, we assure heat balance. A second requirement to be met is that the cycle mean heat transfer at the inner wall be 90.8 watts. This amounts to a constant offset of the additional mean term and does not affect its time variation. It should also be noted that the first assumption does not require specification of the base heat source but lumps its value into the additional mean term.

Figure 12 shows the resulting radial distribution of the heat transfers. While the corrections are somewhat arbitrary, the important point in these diagrams is that the eddy heat transfer is large in the interior regions and at $T = 13$ is nearly twice the total heat transfer. Independent of the particular assumptions above, this excess heat transfer must be balanced by an indirect cell. Also nearer the walls the eddies become less efficient and there must be a direct cell in these regions to maintain balance. It is clear that the computed mean term is deficient both in the direct and indirect regions. The additional mean term makes up the deficiency to insure that the heat transfer balances.

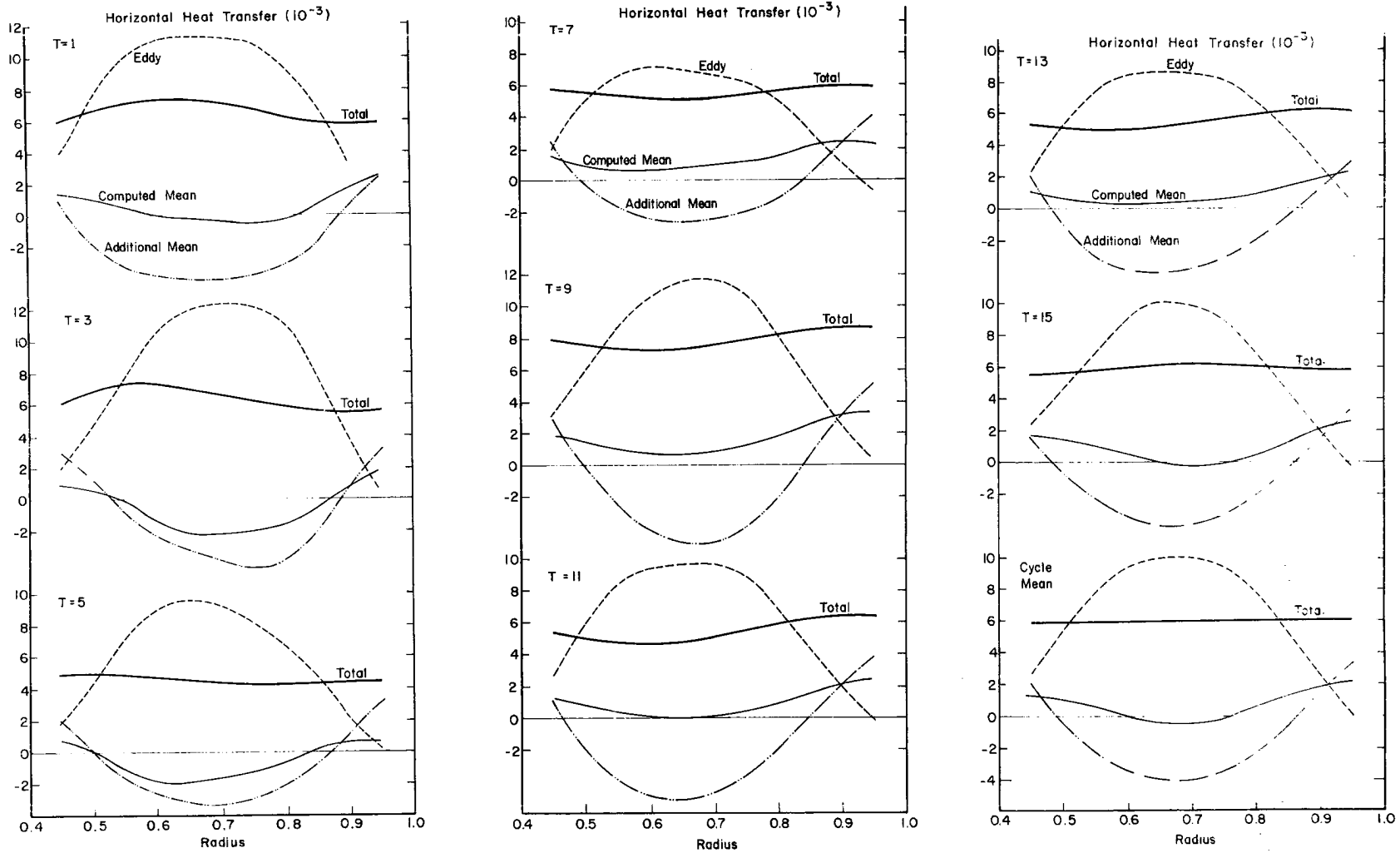


Fig. 12 Horizontal heat transfer versus radius for each time and the cycle mean.

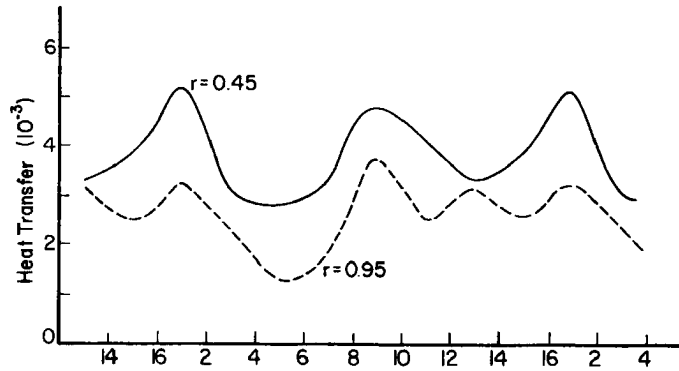
As mentioned above the additional mean, and thus the total heat transfer, curves in Figure 12 have included in them the base heat source. Even so the total heat transfer curve is not a constant since the evaporation and time change in heat storage have not been included. Generally there are nearly offsetting regions of warmer and cooler water which explains the curvature in the total heat transfer curve.

Riehl and Fultz (1958) also computed an excess of eddy heat transfer over the constant source to sink requirement. This occurred in a smaller region near mid-radius and was balanced by a weaker indirect cell. That the eddy heat transfers are so efficient was already suggested by the near vanishing of the zonal temperature gradient in the middle of the annulus. With the smaller lapse rate (1 C/cm) in this case, a stronger indirect cell is required to transfer the same amount of heat outward needed to balance the excess eddy heat transfer.

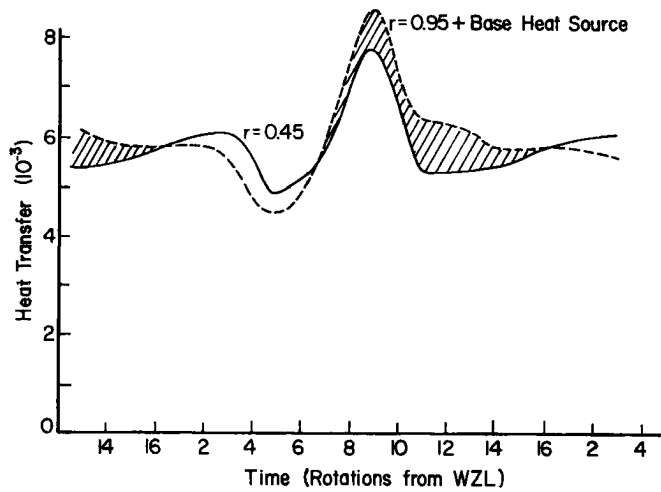
To relate the heat transfer to the vacillation cycle we look at the computed inflow and outflow of heat from the fluid. Figure 13a shows the vertically integrated total heat transport at $r = 0.95$ and $r = 0.45$. These are the computed values without the additional mean and without inclusion of the base heat source. The dominant part of the mean comes from the top and bottom layers whose \bar{v}_r values are listed in Appendix D. Two corresponding peaks in the outflow of heat at 0.45 are also predicted. Even with the inclusion of a base heat source of 15 watts, the evaporation and the time changes, heat balance is not achieved between the 0.45-0.95 radii.

Total Heat Transfer Through $r = 0.45, 0.95$

(a) As Computed



(b) With Additional Mean Flow



(c) With Constant Heat Source

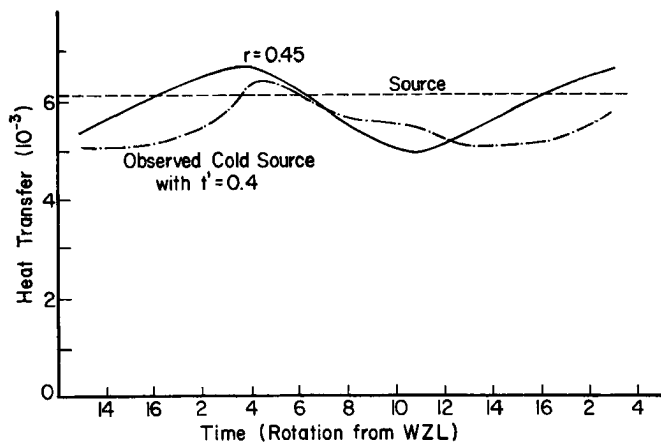


Fig. 13 Vertically-integrated total heat transfer through $r = 0.45$ and $r = 0.95$. Cross-hatching indicates times when heat inflow exceeds outflow.

Inclusion of the additional mean heat transfer as in Figure 13b will satisfy heat balance. Since this technique appears to put in all the heat at 0.95, the difference between the two curves gives the net heat transfer. This difference is made up of a constant evaporation and the time change integrated over the volume between 0.45-0.95. The hatched region indicates the times when the mean temperature is increasing since there is less heat being transferred out of the volume than is being put in. Conversely in the developing vortex stage ($T = 1$ to 5) the heat transfer at $r = 0.45$ exceeds what is coming in at $r = 0.95$. This agrees with our conception that at least one function of the vortex stage is to increase the heat transfer.

Variations of heat input of the magnitude predicted in Figure 13b are unlikely since they represent deviations of up to 35 per cent of the nominal total heat input of 95 watts. As we indicated earlier these variations, if they exist, could have been computed if the \bar{v}_r would have been correct. However with \bar{v}_r unknown, it is not possible to test these variations. One further indication that this large of an input variation is not likely is that the temperature--time trace near the heat source has a much smaller amplitude than that near the cold source. This would indicate that heat storage near the heated wall is not sufficient to explain variations of the heat inflow comparable to the outflow.

Constant heat sources. If we integrate over the volume of the fluid, the integrated time change of heat content must be equal to the net external heating and cooling. Since we specify input and evaporation, the knowledge of the time changes leads directly to the

outflow at $r = 0.45$. This is shown in Figure 13c by the solid line. As before there is more outflow than inflow in the vortex stage, which is being replenished over the remainder of the cycle.

For comparison we have entered an estimate of the amplitude and phase variations from the observed temperature changes in the cold source. Because of the mass of water in the cold source, the amplitude and time variations actually existing at the cold wall are strongly damped. Although the cycle mean heat transfer is well known, its time variations are subject to interpretation. Various tests were made of the time for an impulsive change at the inner wall to be noted at the thermocouples in the cold source. Then a graphical method of lagging the observed curve with a time constant of 0.4 of a cycle gives the curve in Figure 13c. While the amplitudes are comparable, there is a phase difference.

Summary of the heat balance. The eddy heat transfer is extremely efficient in the middle of the fluid, transferring more heat than is required. A compensating indirect cell must be set up to balance this excess heat transfer. Since the mean meridional motion computed from the divergent part of the motion is not intense enough to balance the eddy transfer, an additional mean transfer is computed. A stronger mean transfer is required in both of the direct cells and the indirect cell.

A time variation of the heat sources is suggested by the computed mean plus eddy transport. However a computation specifying constant heat sources and evaporation leads to an estimate of the heat outflow whose amplitude and phase are nearer to the observed variation with time. This does not exclude time variation in the

heat sources, but indicates the amplitude must be smaller than that suggested by the computed mean plus eddy transport.

As an integral requirement of the fluid to transfer the heat, the variation with time is specified by the time changes of heat content. The heat content is decreasing during the vortex stage and increasing during the remainder of the cycle (see Figure 13c). The net change in heat content is the sum of increases in one region being either stronger or weaker than the decreases in the remainder of the fluid. It might also be noted that the heat transfers occur nearly uniformly with height at any radius, thus keeping the stability or lapse rate nearly the same.

CHAPTER VII

ANGULAR MOMENTUM

A balance of angular momentum showing the internal redistribution of momentum by eddy and mean motions was not successful. In part this was due to the bias in the mean meridional motion, but was also caused by inaccuracies in evaluation of the time change of momentum. Compared to time changes of temperature or heat content, the changes in angular momentum are rapid and are not resolved by taking centered differences over large intervals, in this case four rotations. Thus we concentrate on estimates of the source/sink at each surface.

At the top and bottom surfaces (S) the torque due to frictional stress $\tau_{\theta z}$ acting at radius r may be expressed as $\int \rho C_D v_{\theta} V r dS$. At the top we previously used $C_D = 0.01$ based on two estimates from Väisänen's (1961) data, and at the bottom a value of 0.05 was estimated from data on channel flow over a flat surface. Because the velocity data did not extend into the wall regions, another approach was taken there. If the time changes of momentum are small within the boundary layers, the source/sink must be equal to the momentum transferred away from/to the wall by the eddy or mean motion. And if the eddy term is small close to the wall, we can use the mean meridional circulation required for heat transfer to compute the momentum transport. The mean zonal velocity values necessary to calculate the momentum transport can be interpolated more accurately than the product $v_{\theta} V$. In fact we assume a linear decrease from the first gridpoint at which the velocities are known.

Averaged over the whole cycle the sources and sinks should balance, but we see in the sketch at the top of Figure 14a that there

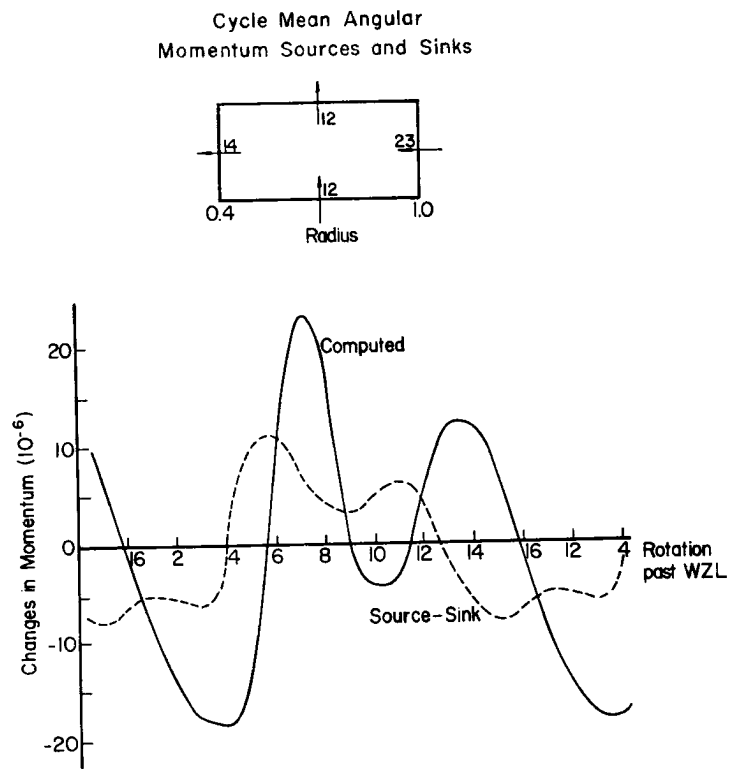


Fig. 14a Angular momentum sources and sinks at the walls and top and bottom surfaces (above). Difference between source and sink compared with changes computed from observed total momentum (full line).

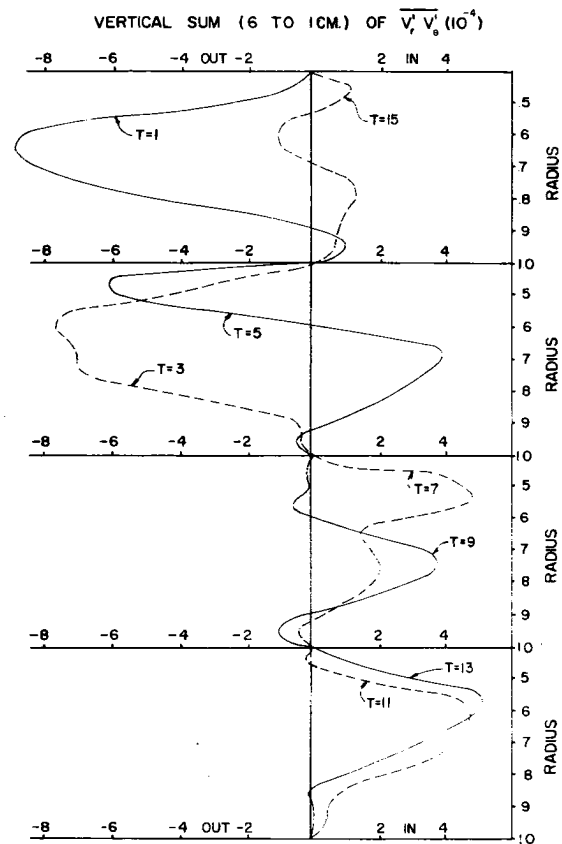


Fig. 14b Vertical sum of $\overline{v_r^T v_\theta^T}$ (10^{-4}) versus radius for different cycle times. Negative values indicate momentum flux outward.

is an unbalance of nine units. This is not bad considering the crudeness of the computation, and we assign the unbalance to the sink at the top by increasing C_D from 0.01 to 0.0175. Then in the lower half of Figure 14a we compare at each time the unbalance of source and sink with a smoothed time change computed from the total momentum integrated over the volume. The source-sink unbalance varies more regularly than do the computed changes which, as we noted above, are the differences between large numbers.

Even though momentum balance in the interior was not achieved, the vertical sum of the eddy momentum flux $\overline{v_r'v_\theta'}$ versus time is shown in Figure 14b. This dramatically illustrates the reversal of the flux, changing from the large outward flux at $T = 1, 3$ and 5 to the smaller inward flux at the remaining times. Wiin-Nielsen et al (1964) show that north of about $50-55^\circ$ lat. the eddy flux is southward, but the magnitude is smaller than the maximum northward flux at 35° . Because of the relative magnitude of the jet velocity and the tendency for outward momentum transfer, this experiment would seem to be more nearly analogous to upper middle latitude flows.

In the next section we use the eddy momentum flux to compute the transformation between zonal mean and eddy kinetic energy. The reversal of $\overline{v_r'v_\theta'}$ then implies a reversal in the direction of the transformation of energy.

CHAPTER VIII

ENERGY CYCLE

A convenient method of summarizing the energy cycle integrated over the whole volume is the splitting of the energy quantities into their zonal and eddy components. Lorenz (1955) derived expressions for these components and the conversions between available potential energy and kinetic energy. These expressions, adapted for the particular model, serve to describe the development of numerical simulations of the general circulation. A number of studies of the energetics of the atmosphere have been carried out to compare with models. We will present here the results of computations of the energetics for the annulus using expressions (derived in Appendix E) analogous to those of Lorenz (1955).

We define the zonal and eddy kinetic energies by the relations

$$\langle \bar{K} \rangle = \frac{2\pi}{g} \int_{p_s}^{p_B} \int_{r_0}^{r_i} \frac{1}{2} \bar{V}^2 r dr dp$$

$$\langle K' \rangle = \frac{2\pi}{g} \int_{p_s}^{p_B} \int_{r_0}^{r_i} \frac{1}{2} \overline{V'^2} r dr dp$$

where r_i and r_0 are the radii of inner and outer walls, the integration $\langle \rangle$ being over the whole mass of fluid. Also we use p_s and p_B as the pressures at the top surface and the bottom. The zonal kinetic energy can then be expressed (see Appendix E)

$$\frac{\partial \bar{K}}{\partial t} = C(K', \bar{K}) + C(\bar{P}, \bar{K}) + D(\bar{K})$$

where $C(K', \bar{K}) = \langle \overline{v_r' v_\theta'} \frac{\partial \bar{v}_\theta}{\partial r} + \overline{\omega' v_\theta'} \frac{\partial \bar{v}_\theta}{\partial p} \rangle$

$$C(\bar{P}, \bar{K}) = -\langle \bar{\omega} \bar{\alpha} \rangle \quad \text{and} \quad D(\bar{K}) = \langle \bar{v}_\theta \bar{F}_\theta + \bar{v}_r \bar{F}_r \rangle$$

are respectively the conversions between eddy and zonal kinetic energy and between zonal potential energy and zonal kinetic energy, and the dissipation since F is the frictional force per unit mass. Subtracting this equation from the total kinetic energy integrated over the mass generates the eddy kinetic energy equation

$$\frac{\partial K'}{\partial t} = -C(K', \bar{K}) + C(P', K') + D(K') \quad \text{where}$$

$$C(P', K') = -\langle \overline{\omega' \alpha'} \rangle \quad \text{and} \quad D(K') = \langle \overline{v_{\theta}' F_{\theta}'} + \overline{v_r' F_r'} \rangle$$

Therefore the conversion of eddy to zonal kinetic energy appears in each equation but with an opposite sign. In the total kinetic energy equation, i.e. the sum of these two equations, this term disappears since the advection terms disappear upon integration over all the mass.

The expression for zonal available potential energy is derived as $\frac{\partial \bar{P}}{\partial t} = -C(\bar{P}, \bar{K}) + C(P', \bar{P}) + G(\bar{P})$ (6)

Here we have defined

$$\langle \bar{P} \rangle = \langle \frac{\beta^*}{2\sigma} \bar{\tau}^2 \rangle \quad \langle P' \rangle = \langle \frac{\beta^*}{2\sigma} \tau'^2 \rangle$$

$$\beta^*(p) = \frac{\alpha}{\tau} \quad \sigma(p) = \frac{\partial \tau}{\partial p}$$

$$C(P', \bar{P}) = \langle \frac{\beta}{\sigma} \{ \overline{v_r \tau} \frac{\partial \tau}{\partial r} + \overline{\omega' \tau'} \frac{\partial \tau}{\partial p} \} \rangle$$

$$G(\bar{P}) = \langle \frac{\beta \bar{Q}}{\sigma C_p \bar{\tau}} \rangle$$

While the zonal available potential energy \bar{P} depends on the tilt of the isotherms in the meridional plane, the eddy term P' depends on the tilt of the isotherms in east-west plane, that is, on the alternating warm and cold pools of water. The conversion from eddy to zonal available potential energy contains the product of the heat

transfers and the respective zonal temperature gradients in the horizontal and vertical. It should be noted that the horizontal heat transfer includes both mean and eddy terms, while only the eddy vertical heat transport appears. Generation of \bar{P} depends on the product of the zonal temperature and zonal heating rate and will be positive if the heat is added at higher temperature than it is taken out.

Again subtracting the zonal equation from the total equation yields the eddy available potential energy equation

$$\frac{\partial P'}{\partial t} = - C(P', K') - C(P', \bar{P}) + G(P')$$

where $G(P') = \langle \frac{\beta^* Q' \tau'}{\sigma C_p} \rangle$ depends on the correlation of the deviations of the heating rate and temperature from their zonal averages.

Evaluation of the energy cycle quantities. Of the eight conversion, generation and dissipation terms, only the four conversions can be directly evaluated. For the other terms, the exact distributions of heating and friction necessary for evaluation are lacking. But the four unknowns can be determined from the four equations since we can determine the remaining terms. From the integrated energy quantities versus cycle time we can evaluate the terms on the left of each equation and we compute the conversion terms.

Integration over the entire mass was necessary in the derivation of the equations to eliminate advection of energy into the volume. Such quantities are difficult to evaluate, but we are now required to determine the conversions within the boundary layers. This is particularly important for $C(\bar{P}, \bar{K})$ since the intense vertical motions in the boundary layers prove to be the dominant influence. Of course

the indirect cell in the interior works against the direct cells at the walls. To obtain a consistent estimate of $\bar{\omega}$ throughout the fluid, a simple heat balance model based on linear profiles of \bar{v}_r and $\bar{\tau}$ with height was used. This is equivalent to Riehl and Fultz' (1958) calculation of $\bar{\omega}$ in the interior knowing the eddy heat transfer and assuming minimum energy in the \bar{v}_r profile.

Because of the inconsistencies in the vertical motion calculations, the magnitude of $C(P',K')$ is questionable. Another such term is that dependent on the vertical heat transfer in $C(P',\bar{P})$. In the atmosphere this term is generally taken to be small, but it is relevant in the annulus because of the coupling of the vertical heat transfer with the vertical temperature gradient. The horizontal and vertical heat transports act in the opposite sense, acting down the temperature gradient in the horizontal and up the gradient in the vertical. Integrated over the mass the vertical term is about the same magnitude as the part of the horizontal heat transfer term which is due to the mean motion.

Since we take $\beta^* = \beta^*(p)$ only, we evaluate this coefficient in the equation of state for the standard profiles of τ and α , with the result $1.8 (10^{-4}) < \beta^* < 2.4 (10^{-4})$. Although β^* is nearly constant, the lapse rate σ varies greatly, including passing through zero in the evaporating surface layer. To prevent this singularity, a profile of β^*/σ is extrapolated to the upper surface for use when data at 7.0 cm is included. The main effect of this factor is to increase the importance of the layer 6 to 7 cm in the weighting before vertical integration, perhaps distorting the actual magnitudes. However our interest here is to determine the trends rather than attempt exact correspondence.

Energy quantities versus cycle time. The variation which we are trying to explain is shown in Figure 15. Of the four energy quantities the most regularly varying is the zonal potential energy, which decreases rapidly with the initiation of the vortex stage and then steadily grows to its maximum near $T = 15$. Exhibiting the identical phase variation (not 180° out of phase) is the zonal kinetic energy.

The eddy kinetic energy has a maximum in the early vortex stage and then decreases strongly before reaching a secondary maximum at $T = 9$. We also note the ratio of nearly three between eddy kinetic and zonal kinetic energy. In the atmosphere there is typically equal energy in eddy and zonal mean components.

Almost no variation is shown in the eddy potential energy, indicating that the east-west tilt of the isotherms remains nearly constant throughout the growth and decay of the vortex. It can be shown that the contributions to the time variation of the other three quantities from the various layers are in phase. For the eddy potential energy the layers are partially out of phase. Table 2 shows the time deviations of the eddy temperature variance for the upper and lower layers compared to that in the interior of the fluid. While the vertical displacement of the maximum and minimum are not a proof of vertical propagation, which would require computation of the advection of energy, the trend is suggestive and indicates that different levels may participate in the conversion from P' to K' at different times to maintain P' approximately constant.

The sum of the four energy quantities, that is, the total energy of the fluid is not a constant but is determined by the external

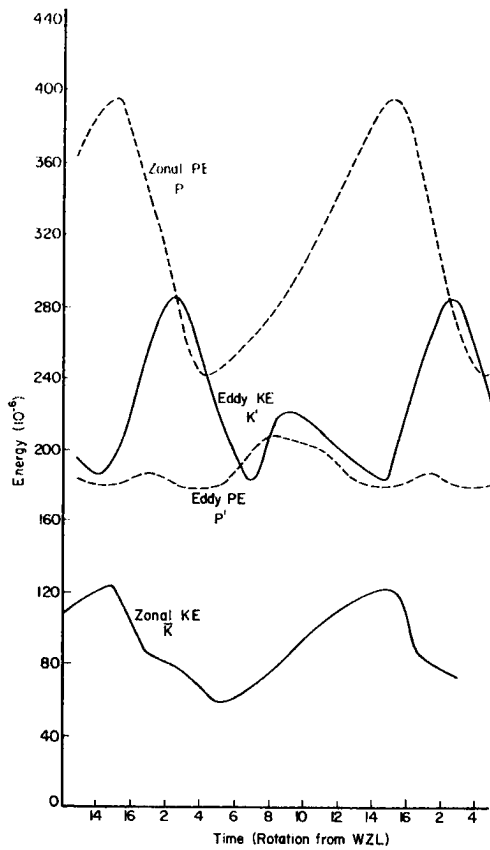
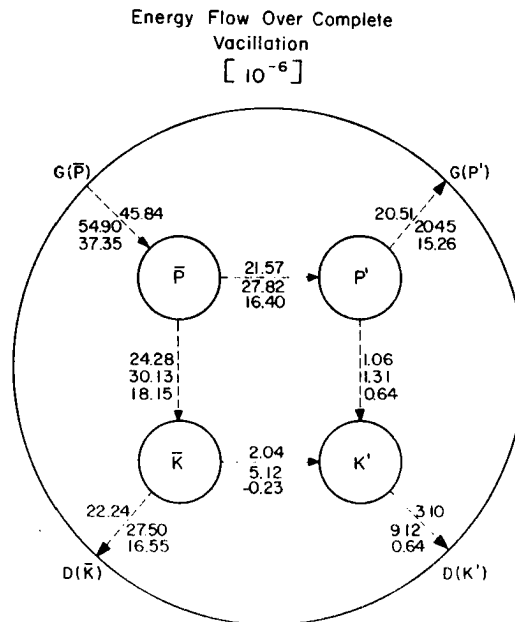


Fig. 15 Kinetic and available potential energy versus cycle time.

Fig. 16 Energy flow averaged over the cycle, upper value. Lower two numbers are the maximum and minimum values, G-Generation, D-Dissipation.



Net Generation Averaged Over Cycle
 $- 25.33 \left\{ \begin{matrix} 33.73 \\ 18.00 \end{matrix} \right\}$

Net Dissipation Averaged Over Cycle
 $- 25.33 \left\{ \begin{matrix} 34.75 \\ 18.14 \end{matrix} \right\}$

Table 2

Time deviations of eddy temperature variance σ^2 (10^{-6})

T/layer	7 + 6 cm	5 to 1 cm	0.1 cm
1	-869	-28	3272
3	-2317	1048	3062
5	-1820	649	2153
7	499	2630	-70
9	1881	2627	-1642
11	1782	34	-2971
13	754	-3145	-3642
15	91	-3817	-166

forcing. Visual inspection shows that the minimum total energy is reached between $T = 15$ and 7 when each of the four quantities is near its minimum. The maximum is reached near $T = 15$ when the zonal components at their maxima dominate over the eddy terms at their minima. This variation is the result of unbalance between generation and dissipation of energy which may be estimated from the energy cycle equations.

Energy cycle over a complete vacillation. Over the complete vacillation the time change quantities go to zero. Thus Figure 16 indicates the magnitudes of the energy transformations necessary to have a steady state with the cycle mean energies. Also included is the maximum and minimum values of each transformation. The overall mean of the generation and dissipation must be equal, but the dissipation range is slightly larger than the range in generation.

It is logical to begin the discussion with $G(\bar{P})$ since, as in the atmosphere, the heating of the fluid at warmer temperatures and cooling at colder temperatures is the basic driving force of the circulation. Again following the normal atmospheric cycle, the conversion $C(P', \bar{P})$ is such as to develop thermal gradients in the

east-west direction at the expense of zonal thermal gradients. An important difference between annulus and atmosphere is the extent to which the eddy potential energy P' is used to maintain the flow. In the atmosphere this energy is predominantly converted to eddy kinetic energy, although some P' is lost, mainly because of radiational cooling. A compensating heat source which acts to increase P' is the release of latent heat in the warm sectors of cyclones. In the annulus the base heating ring, although adding energy to the fluid, does so in an inefficient manner since it acts to destroy P' . By restricting the buildup of east-west temperature gradients it retards the development of strong vertical shear, although at the same time tending to decrease the vertical stability (which increases the possibility of vertical overturning). In this way the fluid maintains nearly the same local Richardson's number.

Only a small amount of potential energy is converted to K' , and the dissipation $D(K')$ can be larger than this amount only if the zonal motion drives the eddies. This occurs at all times except one, indicated by the $-.23$ value, when the eddies drive the zonal motion. Examination of only the surface photographs would suggest that the direction of angular momentum flux was equally divided between inward and outward flows. However the troughline tilt in the lower levels clearly indicates that the flux is outward through most of the cycle. The upper layer vacillates to enhance or offset the lower flux to convert the correct amount of energy to maintain K' against dissipation.

A more fundamental difference between the annulus and the atmosphere is the effect of the input/output of heat in thin boundary

layers. These intense direct cells convert into \bar{K} a large amount of \bar{P} generated in those layers. This is to some extent offset by the indirect cell in the interior which tends to convert \bar{K} to \bar{P} . Given the accuracy of estimating the vertical motion from the heat balance model, the direct cells dominate. However this energy is not necessarily available to the interior fluid since a large proportion must be used up in the same boundary layers where it is generated and converted to maintain the flow against dissipation. The remainder is advected into fluid and is used to maintain K' and the indirect cell.

Time dependent energy cycle. Having gained a feeling for the importance of various terms in the mean energy cycle, we examine the time variation of each energy component equation. A pictorial representation (Figure 17a and b) will be used in which the time change term is the sum of two conversion terms plus the generation/dissipation term.

Summarizing the energy cycle with time we note that the \bar{K} and P' balances are distinguished by near equilibrium between two large opposing terms. In the third balance \bar{P} has a small percentage variation since the two conversion terms are offset by the generation. An obvious correlation with the vacillation is shown by the K' balance. The time change as a function of the unbalance between the conversion $C(K', \bar{K})$ and dissipation $D(K')$ may be seen in the top surface photographs (Figure 1). As we indicated earlier, the variation of the total energy is balanced by the sum of the generation and dissipation terms. The dissipation terms exceed the generation in the vortex

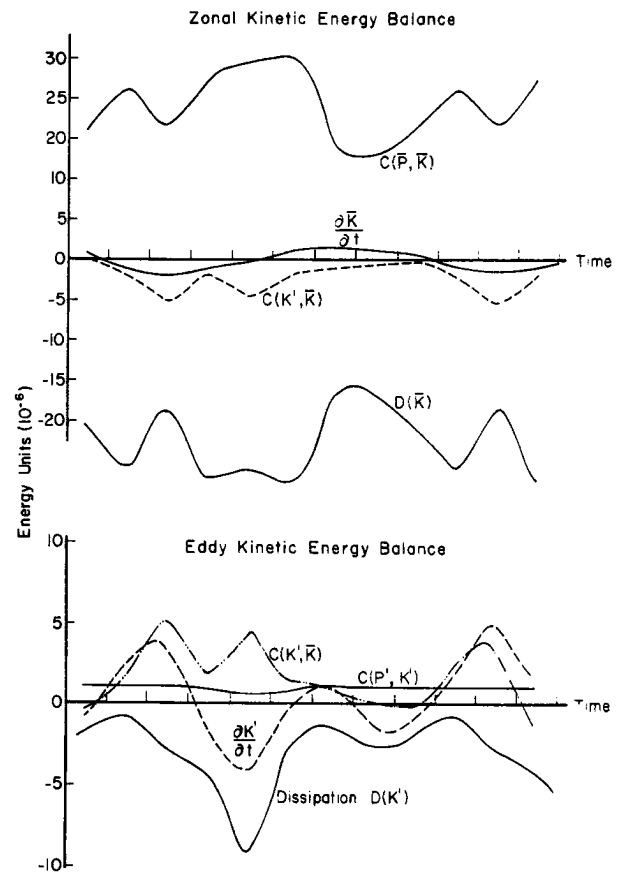
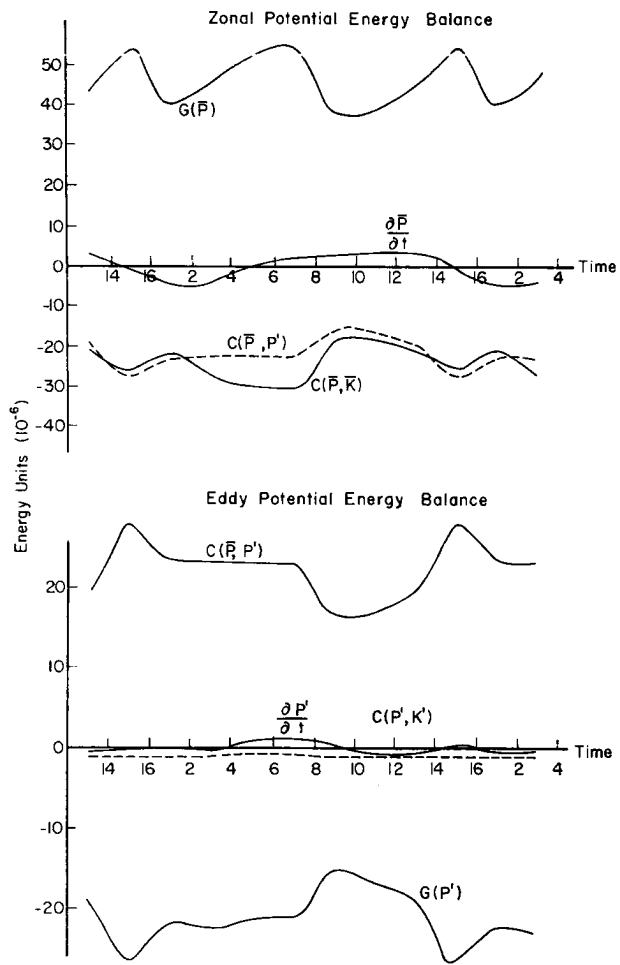


Fig. 17 Individual energy balances versus time. The local change term is the sum of the other three terms. Note the different scales on the ordinates.

stage, and vice versa from $T = 7$ to $T = 15$. Although the individual terms are complex, the total energy variation is in phase with the heating curve.

Pfeffer et al (1967) have suggested that vacillation is the result of an available potential energy cycle varying between maximum and minimum radial temperature profiles. For a given total zonal energy (held constant) which exceeds a critical value dependent on the boundary conditions, they are able to compute the maximum and minimum profiles. Figure 18a illustrates a typical distribution.

For comparison we plot in Figure 18b the temperature distribution near mid-depth at the time corresponding to maximum ($T = 15$) and minimum ($T = 7$) \bar{P} . We expect a sharp decrease in \bar{P} upon the release of baroclinic instability. Pfeffer's theory predicts that the fluid over a wide range of radius (latitude) participates in the redistribution of mass, so that inner and outer regions are nearly symmetric about the midpoint, except the inner region has a larger variation (Figure 18a). This picture is not confirmed in the present case. As expected the radial temperature gradient at inner radii is much larger at $T = 15$ before the vortex stage than at $T = 7$. However the situation is just reversed at outer radii with the larger radial temperature gradient at $T = 7$. This indicates that the temperature profile associated with minimum \bar{P} is continuing throughout the cycle and the growth of the vortex does not make maximum usage of the available potential energy.

Two features of the theory are clearly at variance with the observations. First the endpoints of the temperature profiles are not constant throughout the cycle. Second if the total zonal energy

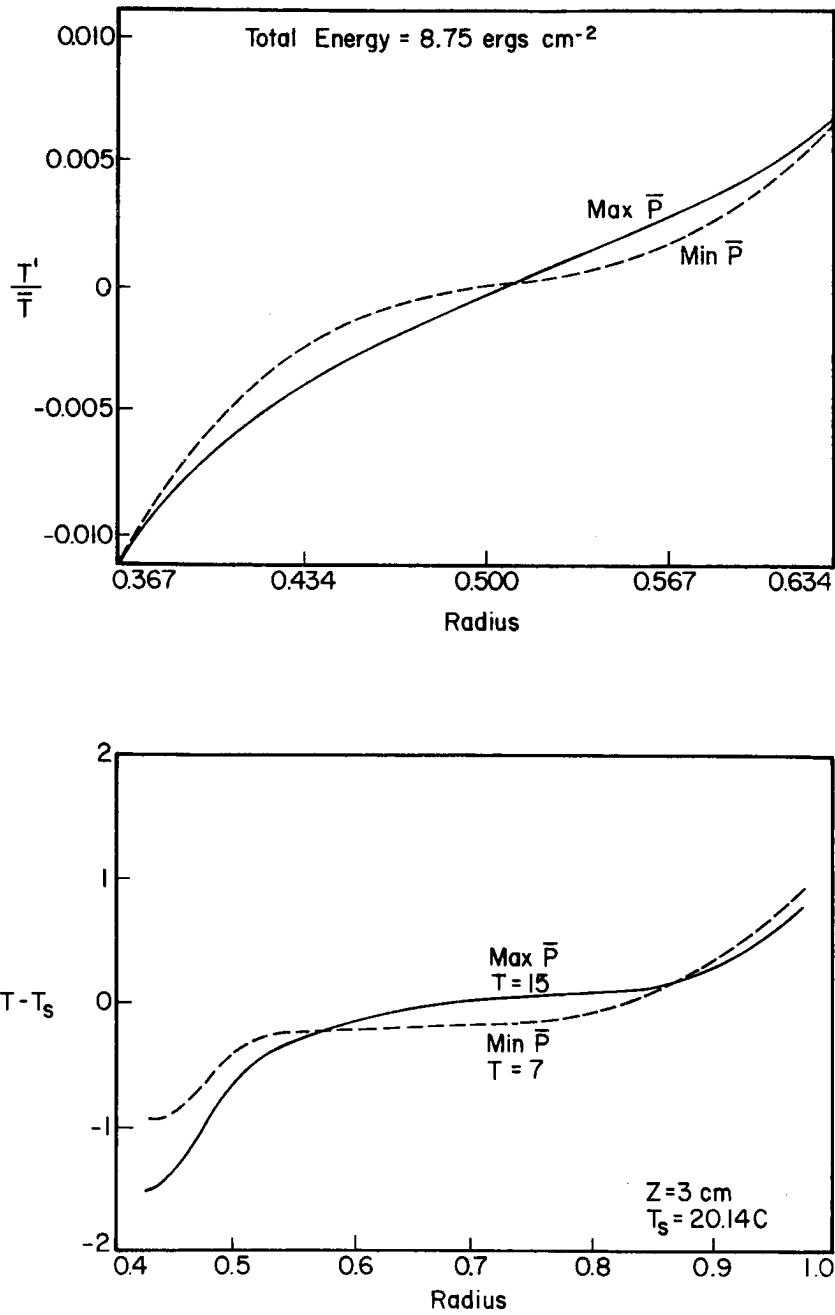


Fig. 18 (a) Temperature profiles corresponding to maximum solid and minimum zonal available potential energy as computed by Pfeffer, et al (1967). (b) Corresponding profiles at $z = 3$ cm for this case.

were constant \bar{P} and \bar{K} changes would be out of phase. We noted in Figure 15 that \bar{P} and \bar{K} are in phase. Vacillation cannot be described as a simple oscillation between \bar{P} and \bar{K} forms of energy.

Comparison with atmosphere. The most complete investigation of the atmospheric energy quantities during a cycle which approximates this experiment was that of Winston and Krueger (1961). Temperatures at 700 mb only and 500 mb geostrophic winds were utilized. The main feature of the cycle was the strong buildup of zonal available potential energy, followed by a sharp decline and associated increases in eddy available and eddy kinetic energy. Only small changes in the zonal kinetic energy occurred. Some of the differences between these observations and the results from the annulus can be ascribed to the presence of five identical waves in the annulus. Integration over the Northern Hemisphere northward of 30° lat. includes waves in various stages of development. In fact when the authors examined the quantities on a regional basis, the events were almost completely dominated by developments over North America and vicinity.

Qualitative comparison of the two cases shows as good agreement as can be expected. Of course the intent of the laboratory experiments is to isolate the phenomena, but our computations have indicated that the energy cycle is not simple. In hopes of clarifying these transformations we will describe some calculations using the jet axis as a reference frame.

Release of potential energy in jet coordinates. Riehl and Fultz (1957, 1958) emphasized the difference in interpretation one gains from examining the vertical motion and the energy transformations in coordinates aligned along the jet axis. For the steady wave these

coordinates are well-defined, but in the time-dependent problem the increased complexity of the equations is a hindrance. Furthermore with the jet impinging on both walls over considerable lengths, the difference in number of data points on either side can seriously distort the computations. Therefore we perform our computations on a grid placed on the inward and outward flowing branches of the surface jet with the requirement that three gridpoints spaced at 0.05 units are present on either side of the jet axis. Because of curvature these gridpoints do not always represent equal areas, but by staying away from the walls this deficiency is minimized.

Since the vertical motion profiles in the interior generally have maxima near mid-depth, correlation of w and temperature τ at $z = 4$ cm should represent the sign and trend in the release of potential energy. For this simple calculation we average the values at equal distances from the jet axis to obtain profiles of mean vertical motion and temperature at seven gridpoints normal to the jet axis for both inward and outward branches. Generally eight gridpoints along the jet were included in the mean quantities $[w]$ and $[\tau]$.

Figure 19a shows the profiles where we have subtracted out the mean quantities $[\tilde{w}]$ and $[\tilde{\tau}]$. Here we introduce the symbol $\tilde{}$ for the average normal to the jet axis. The outward branch is in a net sinking region, whereas the inward jet is in a net ascending region. The completely different character of the two branches is shown in the figure. Although the temperature gradient normal to the jet axis must be approximately the same, the position of relative sinking and rising motion is such as to produce an indirect cell in the outward branch and a direct cell in the inward branch. Maximum ascent relative to the

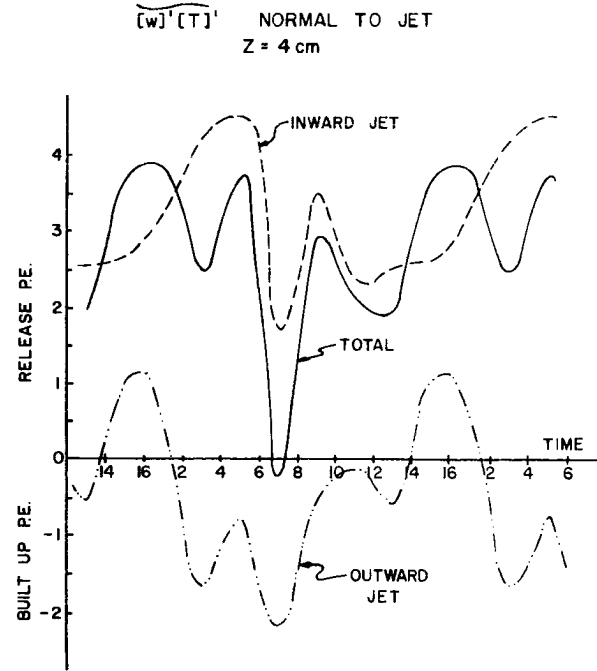
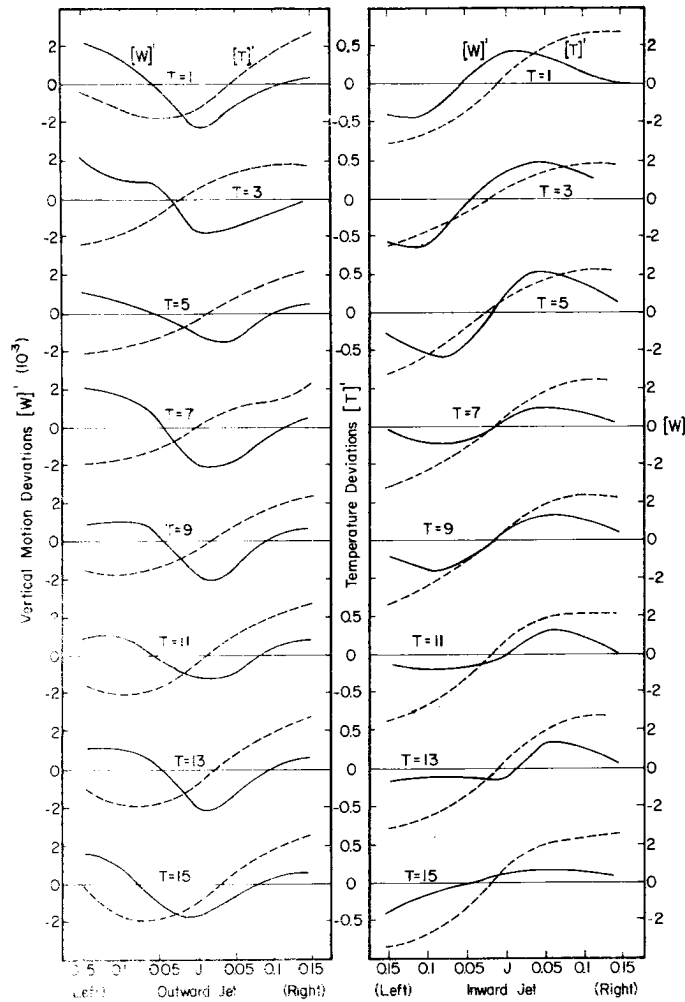


Fig. 19 (a) Vertical motion deviations (left and right scales, 10^{-3}) and temperature deviations (center scale, 10^{-3}) across the outward flowing and inward flowing jets on the left and right, respectively (b) Correlation of quantities in Fig. 19a for inward and outward jets, and their sum as a function of cycle time.

outward jet is to the left in the cold water, with maximum descent near the jet axis where the temperature deviation is small and of varying sign. By contrast in the inward branch the ascent is predominately to the right of the jet in the warmer water. To obtain a more quantitative indication of the release of potential energy in this coordinate system we compute the sum of the products of these deviations.

Figure 19b shows the correlation of $[w]$ and $[\tau]$ where the units are arbitrary. Positive values indicate ascent of warmer water or release of potential energy. The inward jet releases potential energy at all times reaching a primary maximum at $T = 5$ and a secondary maximum at $T = 9$. This variation depends primarily on the intensity of vertical motion rather than shifts in position. More variation is shown in the outward jet, changing from mainly building up potential energy to a release at $T = 15$ and $T = 1$. The minimum value at $T = 5$ occurs because of the secondary jet which has wrapped around the vortex and appears within the grid of the main outward jet.

For the jet system to maintain itself the release in the inward branch must exceed the energy consumption in the outward branch. This is shown to be true by the total curve, except at $T = 7$ where the correlation quantities balance. The two jets are of course coupled. From the point of view of the anticyclones, some of the energy generated on the westerly flank of inward moving air is expended on the easterly flank as the flow banks toward higher pressure. The remainder of the released potential energy is used to maintain the kinetic energy against friction. From the point of view of the cyclone, the effect of the indirect cell of the outward branch is to

maintain and increase the cold dome in the interior. Thus the temperature gradient across the inward jet can be maintained.

Atmospheric jet streams generally have a similar circulation with respect to the jet coordinates. The opposing tendencies in the equatorward (outward) and poleward (inward) branches serve to maintain and export the kinetic energy of the jet stream. Whether the equatorward branch possesses a direct circulation prior to amplification of the jet stream is not presently known. But the calculations for the annulus suggest that the quasi-balance between the direct and indirect circulations may be important in explaining the energy cycle of the vacillation. We now seek a criterion to determine the factors which affect the quasi-balance between the opposing circulations.

CHAPTER IX

POTENTIAL VORTICITY CONSIDERATIONS

Riehl and Fultz (1957) in their study of the three-wave case examined the vorticity changes following geostrophic relative streamlines on isothermal surfaces. Taking the vorticity variations at upper and lower surfaces together, the water moves toward higher vorticity east of the cyclone at low levels and toward lower vorticity at high levels. Qualitatively the theorem of conservation of potential vorticity is applicable. A quantitative check was not possible because of the uncertainties in experimental measurements.

In this section we begin with the assumption that conservation of potential vorticity is the guiding dynamical principle of the interior flow away from boundaries and diabatic layers. Then we shall make use of a theory based on this principle to examine the mechanism and cause of the vacillation.

We separate the problem into two questions: 1. Given the heating and rotation for which vacillation is observed to be the chosen mode of convection, how does this flow maintain its periodic nature? 2. Why does vacillation occur when a slightly different rotation with the same heating gives a steady flow regime? In the next section we attempt to show that the observed characteristics of the vacillation are consistent with linear instability theory for mixed barotropic-baroclinic zonal flows. We then suggest on this basis how only small changes in rotation and heating can invoke either steady or vacillating flows.

Growth and decay of the jet. In previous sections we have described the energy cycle integrated over the entire fluid. Regardless of which coordinate system one uses, the available potential energy changes with time are a characteristic of the vacillation. It is of interest however that the eddy potential energy, or azimuthal east-west tilt of the isotherms, does not change much over the cycle. The larger and strongly periodic variation in zonal potential energy, or radial tilt, may be related to the heating or energy input. We have already noted that the sudden decrease in \bar{P} is associated with development of the vortex flow. We now relate these developments to an instability of the flow. That is we examine the growth or decay of jet velocity as the jet satisfies sufficient conditions for stability or necessary conditions for instability.

Since the jet in the annulus possesses both horizontal and vertical shears, a mixed barotropic-baroclinic treatment is required. Several investigators (e.g. Charney and Stern, 1962, Pedlosky, 1963, 1964a, 1964b, Mahlman, 1966) have studied the stability of a zonal flow with both horizontal and vertical wind shear. Although the generally singular, nonseparable partial differential equation cannot be solved, the necessary conditions for stability can be obtained by integral methods. With some qualifications for the vertical boundary conditions, the non-vanishing of the potential vorticity gradient in isentropic surfaces is a sufficient condition for stability and its vanishing a necessary condition for instability.

In Appendix F we outline the development of the above theorem. The important modifications for the annulus are setting the variation of the Coriolis parameter β equal to zero and replacing the potential

temperature by the temperature. Because β does not enter in the annulus case we reorient the coordinate axis along the jet and apply the above criterion, i.e. we look for a change in sign of the potential vorticity gradient across the jet which is a necessary condition for decay of the jet. If the potential vorticity gradient does not change sign, the sufficient condition for stability is satisfied and the jet should intensify. For simplicity we compute the potential vorticities at the midradius in a vertical cross-section through one wavelength.

Figures 20a, 21a, and 22a show the total velocity at mid-radius in the layers 21-22, 20-21, and 19-20°C. At each time $T = 1$ to 15 the gridpoint 11 is on the troughline at the top surface so this approximately separates the outward flowing jet on the left from the inward flowing jet. When the upper layer (21-22°C) extends into the diabatic layer (above 6.0 cm), the isothermal surfaces become vertical and the computation of potential vorticity is terminated.

While our intent is to examine the relation between the increase and decrease in jet speed as a function of the instability of the jet, the shift in the jet axis, or the sharpness of the trough which characterizes the vacillation is quite evident in the velocity profiles. We later will discuss this shift as a manifestation of the tendency to conserve potential vorticity, and the "overshooting" which leads to the periodic shift in amplitude and tilt that is defined to be vacillation.

Figures 20b, 21b, and 22b show the corresponding potential vorticity profiles in the layers. Here we define the non-dimensional potential vorticity as $q = \frac{c_g + 2\beta h}{D}$ where the geostrophic relative vorticity $c_g = qv^2/h$ taken from the height h fields is used since the

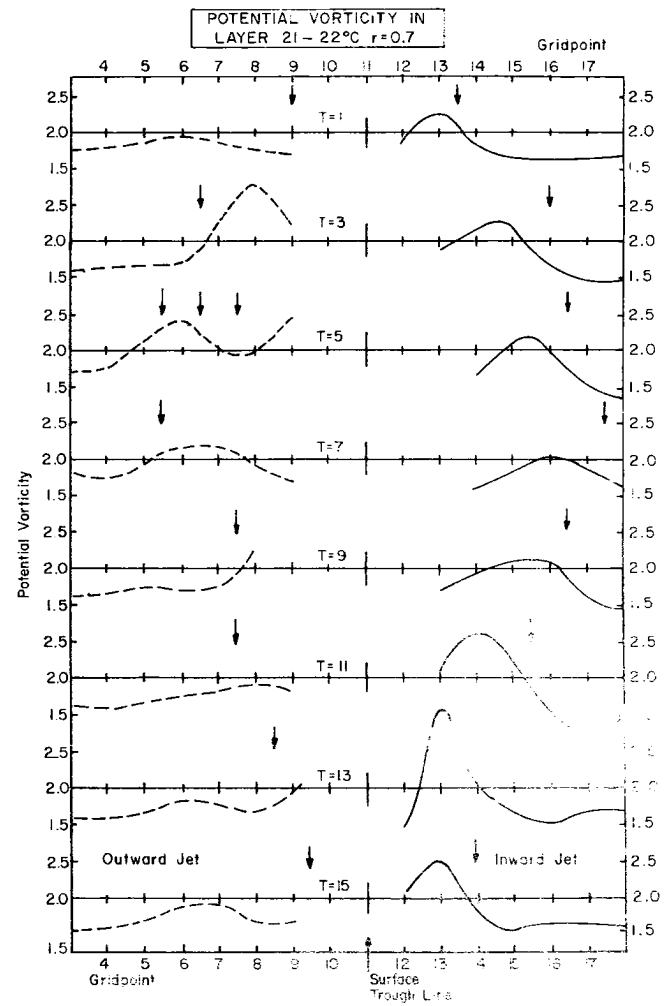
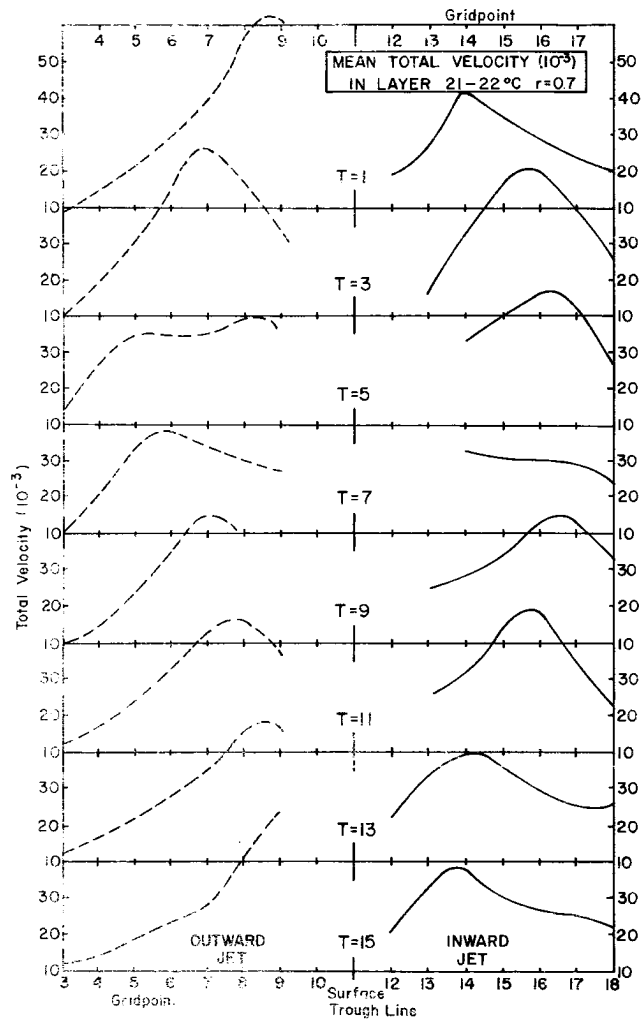


Fig. 10 (a) Mean velocity in the layer 21-22°C in a cross-section along midradius ($r = 0.7$),
(b) Corresponding potential vorticity curves.

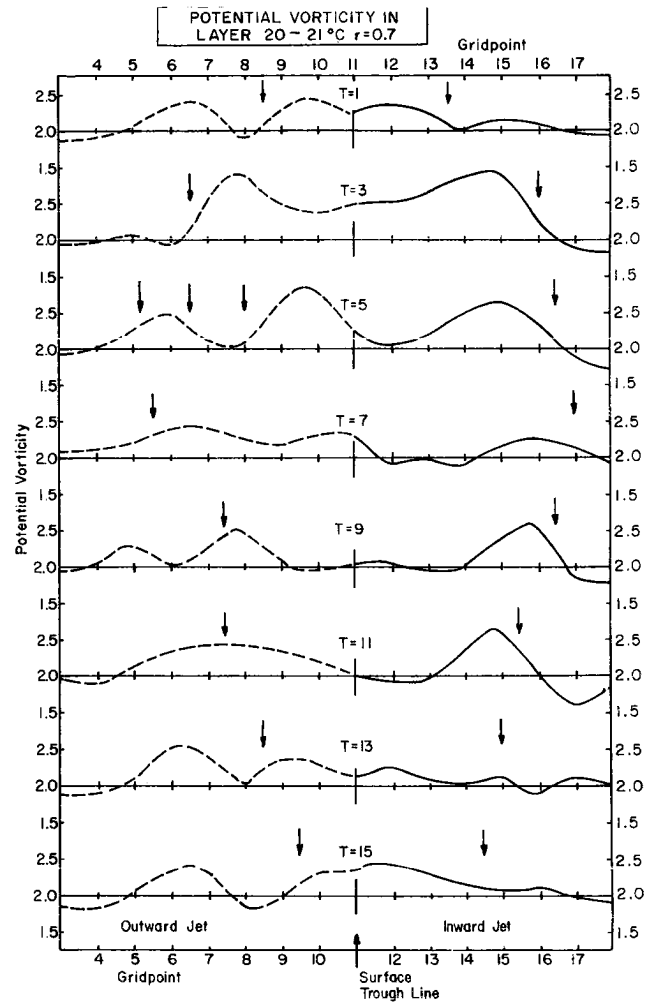
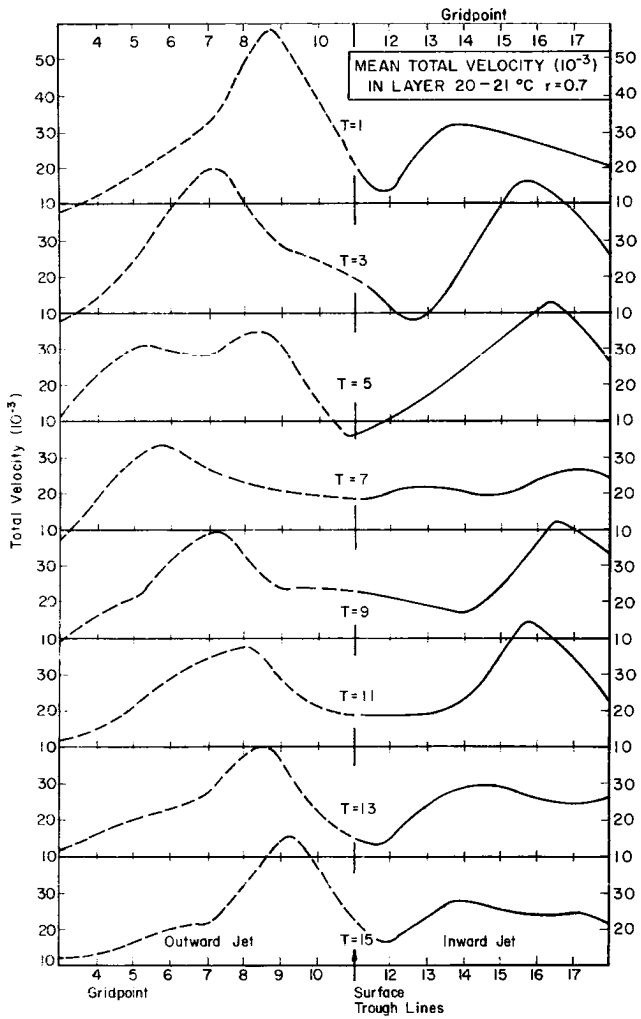


Fig. 21a-b Same as Fig. 20a-b for the layer 20-21°C.

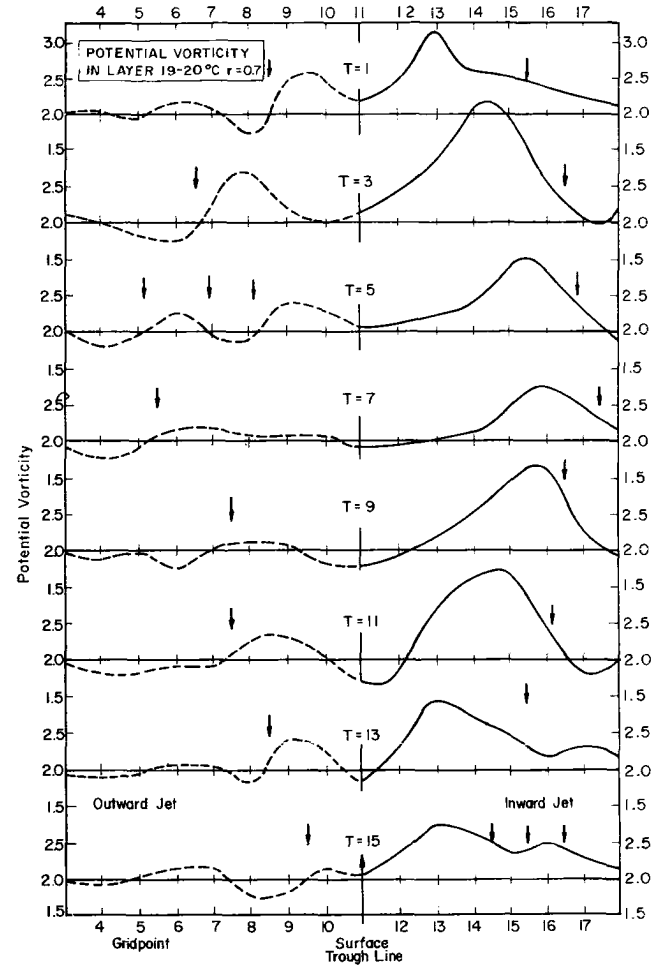
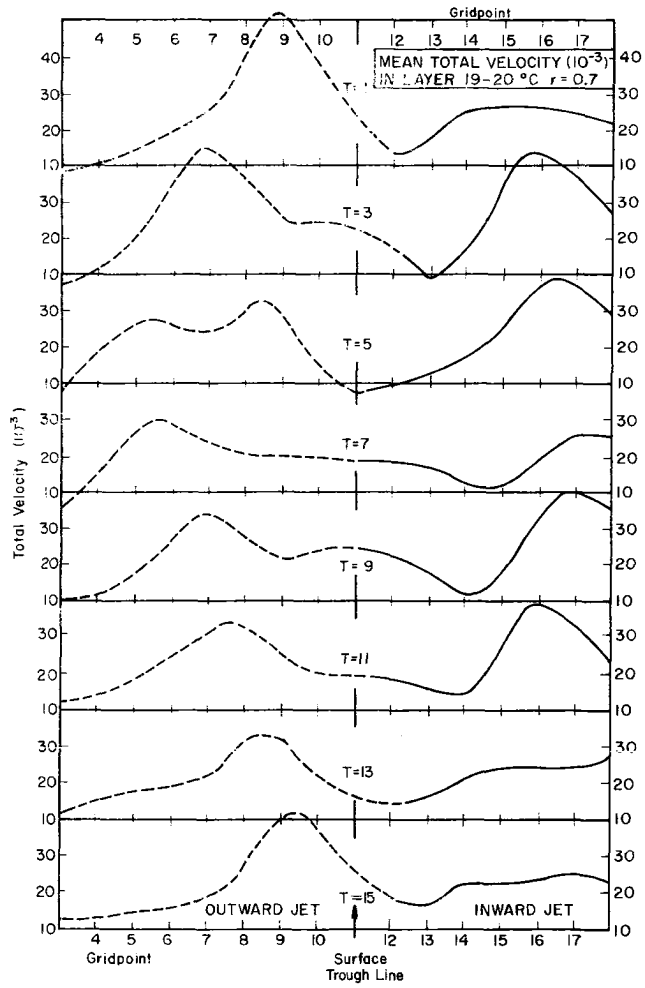


Fig. 22a-b Same as Fig. 20a-b for the layer 19-20°C.

Rossby number is small, 2Ω is the Coriolis parameter, and D is the distance between the isothermal surfaces. D is made non-dimensional by division by one since the normal lapse rate is $1^\circ\text{C}/\text{cm}$. Then since $2\Omega = 2.0$ at all points, the q values may be referenced to a normal value of 2.0. The gridpoints at which ζ_g changes sign are indicated by the vertical arrows and thus are near the locations of the jet axis.

Looking at the outward jet (on left side of the diagrams) first, one notes that the q profiles do change in gradient across the jet axis for a large number of the times. In some cases the small departures from a gradient of uniform sign may be ascribed to errors in the fields, or the grid scale being large with respect to the smaller scale features near the jet core. Also the matching of the two jets across the shear or troughline (near point 11 on the abscissa) leads to irregular q values, but to apply the linear theory for a "zonal" jet in that region would not be justifiable.

At best only the sufficiency part of the criterion may be strictly checked. Consequently we note that in the top ($21\text{-}22^\circ\text{C}$) layer q is essentially increasing from left (anticyclonic) to right (cyclonic) across the outward jet for $T = 1, 9, 11,$ and 13 . From Figure 20a we note that the jet is indeed intensifying at these times. However for the other two layers the jet speed changes (see Figures 21a, 22a) as in the upper layer but the corresponding q profiles may not be classified as stable in each case.

The weakness in the theoretical treatment is then evident, since only the necessary condition for instability (decay) of the jet is given. But the strong changes in slope of the q profiles which

occur when the jet is observed to decay (e.g. $T = 3$ for the outward jet) suggest that the concept of potential vorticity may be useful in extending the necessary condition.

One particularly interesting example where jet intensification is observed, although the necessary condition for instability is consistently satisfied, is shown in Figure 21 from $T = 9$ through $T = 1$. The q profile maintains nearly the same shape throughout with a maximum of positive potential vorticity on the anticyclonic side of the jet. This would imply the anticyclonic vorticity is too small (negative), and/or the corresponding thickness between isothermal surfaces D too small. The indirect circulation about the outward jet continues through most of this time period. An indirect cell by definition increases the potential energy at the expense of kinetic energy, and in addition the q profile clearly satisfies the necessary condition for decay of the jet speed. Nevertheless the jet continues to intensify, illustrating again the need for a sufficient condition for instability. The profile with a positive maximum of q well to the anticyclonic side of the jet axis is evidently stable, at least compared with $T = 3$ when the axis shifts outward and the jet decays. It appears that the degree of freedom in the horizontal allows for stable readjustment of the profile until the jet is constrained by the presence of the inward jet across the troughline. We will return to this hypothesis of stable shifting of the jet axis in the next section.

Without a sufficiency condition for instability, discussion of the inward jet can be quite limited. We note that large variations in q occur across the jet with the maximum q located on the cyclonic

side of the jet axis on nearly every profile. Consequently the necessary condition for instability is satisfied for nearly all levels and times.

One aspect of the vacillation which is readily apparent in the heat balance and energy cycle calculations is the re-appearance of the inward jet at $T = 9$. This is not identifiable in the surface isotachs (Figure 2) and thus was an unexpected feature. But it appears that it is important in the continuity of the vacillation cycle. Close examination of the inward jet q profiles suggests some time continuity between the levels of maxima q on the cyclonic side of the axis. This maximum is displaced upward from $T = 7$ (Figure 22b) to $T = 13$ (Figure 20b), associated with a subsequent decay of the jet profile at each level. In an earlier section (Table 2) we noted indications of upward displacement of eddy temperature variance which precedes the intensification of the jet. Again the evidence is not conclusive for vertical propagation of energy (and maximum instability), but these indications suggest how the continuity of the vacillation cycle is maintained. The mechanism for vertical propagation of the baroclinic energy is not suggested, but we note that there is very small vertical shear at $T = 7$ (Figures 20a, 21a, 22a) and considerations similar to those for the atmospheric case during the equinoxes may be relevant (Charney and Drazin, 1961).

In summary the theorem applies to the extent that increases in jet speed are observed when stable conditions are observed. However the more general case is the fulfillment of the necessary conditions for instability with either intensification or decay of the jet speeds being observed. In the outward jet a seemingly

unstable configuration of potential vorticity remains stable evidently by shifting of the jet axis. In the inward jet, which nearly always fulfills the necessary condition for instability, some evidence for vertical propagation of the instability is suggested to help explain the continuity of the vacillation.

Vacillation versus steady state. Separate consideration of the inward and outward jets illustrates the rather different character of the potential vorticity profiles. They are not disjoint, but between the two cross-sections the jet interacts with the outer wall and very extensively with the inner wall. One feature of joint variation of the jets is the consistent sharpening of the troughline from $T = 5$ through $T = 15$. The outward jet is intensifying throughout this period while the inward jet reaches a maximum at $T = 11$ and then decays. And the region of anticyclonic relative vorticity continues to expand until it covers a large part of the fluid, but with the vortex development the area covered by cyclonic relative vorticity dominates.

Because the Coriolis parameter does not vary in the annulus, there are only two degrees of freedom associated with conservation of potential vorticity, either relative vorticity changes or variations in the thickness D between isothermal layers. Thus we regard conservation of potential vorticity as a balance between vorticity and thermal fields. For steady waves these fields are in balance, but for vacillation our hypothesis is that the fields are slightly out of balance. This takes the form of overshooting as the jet shifts position to bring the thermal (D) and vorticity (ζ) fields into a stable configuration. Eventually the troughline becomes very sharp

and the configuration is unstable with respect to the theorem of the previous section. The kinetic energy of the zonal motion is then being fed into eddy motion as the vortex develops.

We may write the relative vorticity $\zeta = \frac{V}{R_S} - \frac{\partial V}{\partial n}$ in natural coordinates aligned along the velocity vector with magnitude V , where the radius of curvature R_S is defined negative for anticyclonic curvature and n is the normal coordinate positive to the left. Consider the tendency for conservation of potential vorticity on the anticyclonic side of the jet. In the outward branch the jet is stable and thus V is increasing. Suppose the D field with respect to the axis varies very little as V increases, then to conserve q the relative vorticity ζ must remain constant. Since $\frac{\partial V}{\partial n}$ is positive and increasing, there must be a decrease in the curvature vorticity, requiring an increase in R_S . This would tend to force the jet to expand into colder water, i.e. toward larger values of D on the cyclonic side of the axis. For the jet to be in equilibrium this tendency to expand should be in balance with an increase of D in the colder water. That is the thermal and velocity fields must be in adjustment, for the jet cannot exist without the concentrated horizontal temperature field. Now as the anticyclonic jet expands and sharpens the troughline from $T = 5$ to 15 the temperature field tries to maintain its quasi-equilibrium with the velocity. While continuing to transfer heat inward by virtue of the kinematic and thermal structure, the amount of transfer can and does vary. Because the horizontal and vertical temperature gradients are proportional in the annulus, the adjustment for increasing horizontal heat transfer shifts the lapse rate. Consequently D can come into balance. The general requirement for

conservation of potential vorticity reflects the balance between vorticity (or momentum) and heat transport requirements. In the case of vacillation the variation in the area of anticyclonic and cyclonic vorticity is interpreted as an overshooting as the particles tend to, but do not achieve, conservation of potential vorticity. Eventually the shifting of the jet axis creates a very sharp troughline and instability occurs.

To relate the potential vorticity to the question of vacillation versus steady waves we return to a more precise expression for the isentropic coordinates. Using the temperature T rather than the potential temperature for atmospheric case, we write

$$q = \frac{\zeta_T + f}{\frac{\partial p}{\partial T}} = \text{constant}$$

where ∂p is the pressure increment between isothermal surfaces. Now using Fultz' (1959) notation for the non-dimensional (starred) variables, we obtain

$$q = \frac{\frac{\Omega_0}{r_0^2 \Omega_0^2} \zeta^* T + f^*}{\frac{\partial p^*}{\partial T^*}} = \frac{\alpha_0 \Delta_r T}{r_0^2 \Omega_0} q^* \quad (7)$$

where $\Delta_r T$ is the impressed radial temperature gradient due to the heating. The coefficient required to make the potential vorticity non-dimensional involves both the heating and the rotation and is equal to a constant times $\Omega_0 R_{0T}$ where R_{0T} is the thermal Rossby number defined in the introduction. We emphasize that the potential vorticity is explicitly related to the parameters which determine the flow regime which exists in the annulus. And in a different way we see that conservation of potential vorticity is a balance between heat

and momentum requirements. We suggested above that vacillation may be characterized as a quasi-stable oscillation about equilibrium potential vorticity states. The heating and rotation which results in such an equilibrium state is then a steady wave regime. Since Eady's baroclinic stability criterion may be shown (Hide, 1966) to be applicable to the annulus, the wave number of maximum instability can be predicted. Eady's parameter mainly depends on the product of the lapse rate and the rotation (not at all on the vertical shear), so that a given value of q corresponds to a particular dominant wave number. Discrete changes in heating (changing the lapse rate) and rotation lead to discrete changes in wave number as represented by the plot of R_{OT} versus Ω_0 (Fultz, et al, 1959, Fultz, 1964).

Suppose we start from conditions which typify a steady regime, and change the rotation slightly, but not enough to require a different wave number. A number of authors (e.g. Kuo, 1956) have shown that the effects of rotation and stable stratification work in different directions to inhibit the motion. The motion must decrease its horizontal scale and increase its vertical scale at higher rates of rotation if the static stability is to remain the same. If the number of waves around the annulus is not to change, and the waves extend from wall to wall as they do in the vacillation case, then an increase in rotation will require a decrease in static stability or lapse rate, which means an increase in D .

For almost the same heating rate a maximum velocity in the jet of 1 cm/sec was observed for the symmetric, three-wave and the present case. Taking this as the limiting velocity V_{max} for this heating rate we may presume that if the maximum shears are limited

by molecular process the maximum relative vorticity will be proportional to $\frac{V_{\max}}{L}$ where L is the wavelength. Again the vorticity is proportional to Ω_0 since L is inversely proportional to Ω . Because the numerator of the potential vorticity depends on Ω_0 while the denominator depends on Ω_0^2 , there exists the possibility that only small changes in Ω_0 with the same heating rate will result in overshooting as the flow tends to conserve its potential vorticity. As Ω_0 continues to increase larger wave numbers will develop and consequently larger relative vorticities. Even so the adjustments in D will eventually dominate and an irregular wave regime will be the only possible flow.

CHAPTER X

CONCLUSION: ANNULUS --ATMOSPHERE ANALOGUE

Structure of the flow. It is surprising how nearly similar the annulus flow is to atmospheric cyclone waves considering that dynamic similitude is violated in many respects. Previous models, including numerical models, have shown that relatively crude assumptions still produce flows analogous to those in the atmosphere. Evidently the requirement that a rotating, stratified fluid transfer a given amount of heat is best accomplished by quasi-horizontal convection of the type observed in the atmosphere. While momentum must be conserved, this constraint evidently is subservient to the heat transfer requirement.

Among the flow features which we have checked for similarity with atmospheric waves are the temperature, streamfunction and vertical motion. In the meridional cross-section, we noted that the fluid was nearly barotropic over the base heating ring, with concentration of the horizontal temperature gradients near the walls, rather than in the "middle latitudes" as in the atmosphere. Smaller horizontal temperature gradients are observed in the upper levels of the annulus compared with those below the atmospheric jet stream. However the vertical structure of the temperature field is analogous since the axis of cold water tilts forward with height. Because hydrostatic balance holds, the vertical tilt of the streamfunction field will be as in the atmospheric case. Consequently the low-level cyclone is located under the inflection point of the upper level jet. Theoretical analyses, such as Eady (1949), have shown that this variation of temperature and streamfunction is necessary to transfer heat northward,

the main requirement of the flow. To provide the energy to maintain the flow against friction the vertical motion must be such as to lift warmer water relative to sinking colder water. The computed vertical motions in the annulus accomplish this with patterns analogous to those in the atmosphere, other than the maximum of sinking motion as the water comes away from the cold source. Patterns of convergence-divergence relative to the wave are as in the atmosphere. We were thus encouraged to examine the mechanism by which the annulus flow repeats in periodic manner, to obtain clues for similar atmospheric behavior.

Effects of annulus geometry on the flow mechanisms. One aspect of the annulus flow which has been emphasized is the coupling of the boundary layers with the interior flow. Since the energy and momentum sources are separated from the interior by boundary layers, what is made available to the interior is related to the time changes occurring in the boundary layers. For a diagnostic study such as this one, we require sufficient data at points near and in the boundary layers to define the large gradients of the variables, particularly the double structure. This data cannot be taken simultaneously because the physical presence of the present measuring devices disrupts the flow.

Since it is only the internal flow structure which is analogous to the atmospheric disturbances, we are mainly interested in the manner in which the fluid adjusts itself to accomplish the various transports required of it. To that end we have attempted to isolate the coupling with the boundary layers, tacitly assuming that sources and sinks passively provide or accept the required energy.

However the inability of the fluid to transfer the heat between the walls with a stable momentum configuration for this rotation rate, precludes complete decoupling. A very intense production of zonal kinetic energy in the vertical boundary layers is mainly offset by the dissipation in the same layers. Some of this zonal kinetic energy is necessary to maintain the interior flow, since there exists a conversion of zonal to eddy kinetic energy, which is in contrast to the atmosphere. By changing the temperature lapse rate and the zonal wind profile near the walls, the momentum source or sink as well as the available potential energy generated by the heating and cooling are affected.

In addition to the existence of the thermal boundary layers at the vertical walls, the requirement that all the heat be transported from wall to wall is a more stringent requirement than for atmospheric waves. This is partially modified by the base heating ring since that portion of the heat comes in closer to the cold source. Nevertheless an important feature of the vacillation is the extreme efficiency of the eddy motions in transferring heat. A strong indirect cell is required to compensate for the "excess" heat transfer by the eddies.

It is mainly the requirement of nearly constant radial heat transport which requires wall-to-wall amplitude of the waves and affects their dynamic character. In the radial direction the horizontal scale is forced, and only the wavelength is adjustable for differing rotation and heating rates. This may not be entirely true in the steady three-wave case, where the surface jet does not closely approach the outer wall. Furthermore the excess of eddy heat transfer over the required heat transfer is much smaller in the three-wave case. This

suggests that at the lower rotation rates the direct cell at the outer wall is effective in transferring the heat over a greater radial distance. The eddies are not required to transport an excessive amount of heat over a very large fraction of the radial interval gap, and thus the amplitude of the surface jet is not wall-to-wall.

An interesting feature of the three-wave case, which may be related to the smaller amplitude of the surface jet, is the observation that the outer wall did not strongly participate in the momentum balance. In the present case the impinging of the jets on the outer wall suggests that some angular momentum is lost to the wall. A different arrangement of source and sink at the walls must be related to the other surfaces, particularly the base.

It has already been pointed out that the base heating ring has several important effects on the thermal structure. First it decreases the east-west temperature gradients and thereby destroys eddy available potential energy. Secondly it decreases the vertical stability. It also serves to concentrate the horizontal temperature gradient near the walls. The largest vertical shear is then located near the walls, corresponding to the strong easterlies near the bottom. However over the base ring the zonal motion is still westerly. This momentum source/sink arrangement broadly corresponds to that in the atmosphere although the magnitudes are somewhat different. Because the easterlies near the outer wall are stronger and at a larger torque arm, this should be the major angular momentum source region. Then since the predominant sink appears to be the inner wall, one would have expected net inward momentum flux, an arrangement similar to the atmosphere. But we have shown that at the lower layers

the troughline tilts northwest-southeast over the entire cycle, thus net outward eddy momentum flux occurs. The mean meridional circulation accomplishes very little net transport since there is almost no vertical shear over the base heat source. As a result of this and inaccuracies in the time change term, the momentum balance was not successfully resolved.

An effect which has not been treated qualitatively is the presence of the evaporating layer at the top surface. Of what importance this unstable layer is compared to the stable stratosphere above the tropopause is not known.

The variation of the Coriolis parameter, or the β effect, is one of the most important of the atmospheric effects which is missing in the annulus. Since Rossby (1939) showed that neutral barotropic waves on the β plane have wavelengths comparable to those of the long waves in the atmosphere, much importance has been attached to this effect. We have already noted that the stability of the zonal jet is dependent on the northward gradient of potential vorticity on an isentropic surface, and thus includes β . In the present case we have shown that application of this criterion to the branches of the jet agreed fairly well with subsequent growth. When the jet was stable the vorticity and thermal fields were in balance. For the atmosphere the β effect is an additional stabilizing factor, at least for zonal jets, indicating the atmospheric flows may become more out of balance than the annulus jet before becoming unstable. Thus in the atmosphere much stronger cyclonic and anticyclonic shears occur near the jet axis. It is important to emphasize that this is only a necessary condition for instability. However when the sufficient

condition for instability is reached, at least the possibility for stronger readjustment exists in the atmosphere than in the annulus. This may be another factor in preventing the occurrence of periodic cyclone development in the atmosphere.

A secondary effect of β is the tendency for northward propagation of cyclones in the atmosphere. Even if such an effect were included in the annulus (Fultz and Kaylor, 1959) the presence of the inner wall still constrains the motion more than in the atmosphere. This also assures that the same disturbance is available in the annulus for subsequent intensification in the next cycle of the vacillation.

Arguing from the analogy with the annulus, one would look for conditions in the atmosphere which have somewhat the same character. Flow in the upper middle latitudes is indicated by the momentum flux characteristics. The smaller heat transport requirements and the larger vertical component of the earth's rotation at higher latitudes are in agreement with general experimental conditions. Certainly the analogy with traveling cyclones and anticyclones and the associated polar front jet would be better than for conditions dominated by a strong quasi-stationary subtropical jet.

Carrying the analogy further one would look for more barotropic intensification of the jet similar to the model of Kuo (1951). In that model the energy for intensification was added from a baroclinic layer below during dormant periods, and the subsequent redistribution of energy in the form of an index cycle was predicted from barotropic instability. In the experiment the energy is added almost constantly and the redistribution is determined by a mixed baroclinic-

barotropic instability. The annulus geometry acts in various ways to constrain the model to make it periodic. An investigation of an atmospheric index cycle occurring in the regions mentioned above is necessary to indicate whether the mechanisms which allow periodic motion in the annulus are operating in the atmosphere. At lower heat transfer requirements the development due to baroclinic instability with its vorticity transport requirements could lead to overshooting which is still stable. Consideration of the potential vorticity on isentropic surfaces and the further investigation of sufficient conditions for instability in the atmospheric case are required to complete the annulus-atmosphere analogue.

LITERATURE CITED

- Bring, A. and E. Charasch, 1958: An experiment in numerical prediction with two nongeostrophic barotropic models. Tellus, 10, 88-94.
- Charney, J.G. and P.G. Drazin, 1961: Propagation of planetary-scale disturbances from the lower into the upper atmosphere. Journal of Geophysical Research, 66, 83-110.
- Charney, J.G. and M.E. Stern, 1962: On the stability of internal baroclinic jets in a rotating atmosphere. Journal of the Atmospheric Sciences, 19, 159-172.
- Fultz, D., 1952: On the possibility of experimental models of the polar-front wave. Journal of Meteorology, 9, 379-384.
- Fultz, D., 1956: A survey of certain thermally and mechanically driven fluid systems of meteorological interest, in Fluid models in geophysics. Proceedings 1st Symposium on the Use of Models in Geophysical Fluid Dynamics, Baltimore, Sept., 1953, 27-63.
- Fultz, D., et al, 1959: Studies of thermal convection in a rotating cylinder with some implications for large-scale atmospheric motions. Meteorological Monographs, Boston, American Meteorological Society, 4, 21, 104 pp.
- Fultz, D. and R. Kaylor, 1959: The propagation of frequency in experimental baroclinic waves in a rotating annular ring. The Atmosphere and the Sea in Motion, Rockefeller Institute Press, New York, 359-371
- Fultz, D., 1964: Research on hydrodynamic analogues of large-scale meteorological phenomena. Final Report, Contract No. AF 19(604)-8361, University of Chicago.
- Fultz, D. and T. Spence, 1968: Preliminary experiments on baroclinic westerly flow over a north-south ridge. Proceedings of the Symposium on Mountain Meteorology. Atmospheric Science Paper 122, Colorado State University, 157-191.
- Hide, R., 1953: Some experiments on thermal convection in a rotating liquid. Quarterly Journal of the Royal Meteorological Society, 79, 161.
- Hide, R., 1956: Fluid motion in the earth's core and some experiments on thermal convection in a rotating liquid, in Fluid models in geophysics. Proceedings 1st Symposium on the Use of Models in Geophysical Fluid Dynamics, Baltimore, Sept., 1953, 101-116.
- Hide, R., 1964: The viscous boundary layer at the free surface of a rotating baroclinic fluid. Tellus, 16, 523-529.

- Hide, R., 1965: The viscous boundary layer at the free surface of a rotating baroclinic fluid: effects due to the temperature dependence of surface tension. Tellus, 17, 440-442.
- Hide, R., 1966: On the dynamics of rotating fluids and related topics in geophysical fluid dynamics. Bulletin American Meteorological Society, 47, 11, 873-885.
- Hunter, C., 1967: The axisymmetric flow in a rotating annulus due to a horizontally applied temperature gradient. Journal of Fluid Mechanics, 27, 4, 753-778.
- Kuo, H.-L., 1951: Dynamical aspects of the general circulation and the stability of zonal flow. Tellus, 3, 268-284.
- Kuo, H.-L., 1956: Forced and free meridional circulation in the atmosphere. Journal of Meteorology, 13, 561-568.
- Lorenz, E.N., 1955: Available potential energy and the maintenance of the general circulation. Tellus, 7, 157-167.
- Mahiman, J.D., 1966: Atmospheric general circulation and transport of radioactive debris. Atmospheric Science Paper 103, Colorado State University, 184 pp.
- Pedlosky, J., 1963: Baroclinic instability in two layer systems. Tellus, 15, 20-25.
- Pedlosky, J., 1964a: The stability of currents in the atmosphere and the ocean, Part I. Journal of the Atmospheric Sciences, 21, 201-219.
- Pedlosky, J., 1964b: The stability of currents in the atmosphere and the ocean, Part II. Journal of the Atmospheric Sciences, 21, 342-353.
- Pfeffer, R.L., D. Mardon, P. Sterbenz and W. Fowles, 1967: A new concept of available potential energy. Proceedings of the International Symposium on the Dynamics of Large-Scale Processes, Moscow, June, 1965, 179-189.
- Pfeffer, R.L. and Y. Chiang, 1967: Two kinds of vacillation in rotating laboratory experiments. Monthly Weather Review, 95, 2, 75-82.
- Riehl, H. and D. Fultz, 1957: Jet stream and long waves in a steady rotating-dishpan experiment: structure of the circulation. Quarterly Journal of the Royal Meteorological Society, 83, 215-231.
- Riehl, H. and D. Fultz, 1958: The general circulation in a steady rotating-dishpan experiment. Quarterly Journal of the Royal Meteorological Society, 84, 389-417.

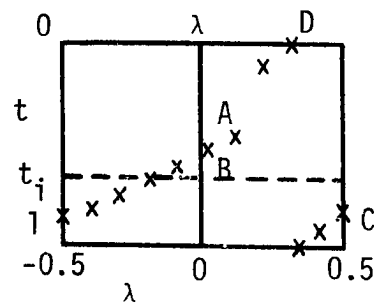
- Rossby, C.-G., 1939: Relation between variations in the intensity of the zonal circulation of the atmosphere and the displacements of the semi-permanent centers of action. Journal of Marine Research, 2, 1, 38-55.
- Rossby, C.-G., 1947: On the distribution of angular velocity in gaseous envelopes under the influence of large-scale horizontal mixing processes. Bulletin of the American Meteorological Society, 28, 53-68.
- Shuman, F.G., 1957: Numerical methods in weather prediction: 1. The balance equation. Monthly Weather Review, 85, 10, 329-332.
- Starr, V.P., 1948: Essay on the general circulation of the earth's atmosphere. Journal of Meteorology, 5, 2, 39-43.
- Väisänen, A., 1961: The general circulation in a symmetrical dishpan experiment. Geophysica, 8, 1, 39-46.
- Wiin-Nielsen, A., J.A. Brown and M. Drake, 1964: Further studies of energy exchange between the zonal flow and the eddies. Tellus, 16, 168-180
- Williams, G.P., 1967: Thermal convection in a rotating fluid annulus: Part 1. The basic axisymmetric flow. Journal of Atmospheric Sciences, 24, 2, 144-161.
- Winston, J.S. and A.F. Krueger, 1961: Some aspects of a cycle of available potential energy. Monthly Weather Review, 89, 9, 307-318.

APPENDIX A

PROCESSING OF TEMPERATURE DATA

Longitude-cycle time measurements. A thermocouple placed at a particular radius and height will trace out the temperature profile as the waves move eastward relative to the annulus. Each rotation the temperature is read and a photograph taken so that the thermocouple can be located relative to wave-zero longitude (WZL). The sequence of photographs through the vacillation cycle also defines the cycle time at each rotation and temperature measurement. In the sketch let this

temperature be at point A on the longitude (λ)-cycle time (t). Since the wave moves to the east, the next temperature measurement at point B will be nearer to the wave zero longitude ($\lambda=0$) at the new cycle time. As



the thermocouple passes into the next wave at point C, the series of points continues from the right side of the diagram. As one vacillation cycle is completed, the cycle time repeats at point D. Over a complete modulation the data points will return to a point near A and eventually will cover the λ - t field. Then for the particular radius r and height z of the thermocouple, the temperature field is completely specified.

For the majority of (λ , t) diagrams three thermocouples spaced a wavelength apart were all located at the same radius and height. For each thermocouple the temperature, λ , and t values were individually determined, and then the average value was used. Generally two complete modulations were used to more completely fill the data plane. Table 3 shows the points in the meridional cross-section for which λ - t diagrams were constructed. Then the data at time t_i corresponding to a surface

$$\nabla^2 h = -\frac{2\Omega\zeta}{g} + \frac{\delta}{2\alpha} \nabla^2 \alpha + \frac{C_D}{g\delta} \{-V(\zeta - D_h) + (v_\theta - v_r) \frac{\partial V}{r\partial\theta} + (v_\theta + v_r) \frac{\partial V}{\partial r}\}_{p=0}$$

which is equation (1) of the text, where $D_h = \frac{\partial(v_r r)}{r\partial r} + \frac{\partial v_\theta}{r\partial\theta}$ and

$V^2 = v_\theta^2 + v_r^2$. Note also that the expression for v_θ when solved for $\frac{\partial h}{\partial r}$ becomes the boundary condition for the relaxation solution of $\nabla^2 h$.

APPENDIX C

QUASI-GEOSTROPHIC ω EQUATION

We derive the ω equation in analogy with the atmospheric form by combining the adiabatic (thermodynamic), hydrostatic, vorticity and state equations. Since our data are in a coordinate system moving with the wave, we expand the total derivative $\frac{D}{Dt} \equiv \frac{\delta}{\delta t} + (\underline{v}-\underline{c}) \cdot \nabla + \omega \frac{\partial}{\partial p}$ or $\frac{D}{Dt} = \frac{\partial}{\partial t} + J(\psi_c, \) + \omega \frac{\partial}{\partial p}$ where ψ_c is the relative streamfunction and we neglect the advection by the divergent part of the motion.

Writing: (a) The equation of state $\alpha = \beta^* \tau$ where α, τ are the deviations from standard values of specific volume and temperature and $\beta^* = \epsilon \Delta_r T$, the volume expansion coefficient times the reference temperature difference across the annulus

$$(b) \text{ Adiabatic equation } \frac{\delta \tau}{\delta t} = -J(\psi_c, \tau) - \omega \frac{\partial \tau}{\partial p}$$

$$(c) \text{ Hydrostatic equation } \alpha = - \frac{\partial \phi}{\partial p} \text{ where } \phi \text{ is the geopotential}$$

$$(d) \text{ Vorticity equation } \frac{\delta}{\delta t} \nabla^2 \psi = -J(\psi_c, \nabla^2 \psi) + 2\Omega \frac{\partial \omega}{\partial p}$$

$$\text{and (e) Balance equation } \nabla^2 \psi = \frac{1}{2\Omega} \nabla^2 \phi$$

By expressing (b) in terms of α by using (a), and then using (c) we obtain one equation in $\frac{\delta \phi}{\delta t}$. Another equation is obtained by combining (d) and (e). Then eliminating $\frac{\delta \phi}{\delta t}$ and defining the static stability $\sigma = \frac{\partial \tau}{\partial p}$ we obtain

$$\nabla^2(\omega\sigma) - (2\Omega)^2 \frac{\partial^2 \omega}{\partial p^2} = \nabla^2 \{-J(\psi_c, \alpha)\} - 2\Omega \frac{\partial}{\partial p} \{J(\psi_c, \nabla^2 \psi)\}$$

In the derivation we have assumed that β^* was a constant. Since we had previously derived ψ from a more complete balance equation, this was used although the corresponding terms have been omitted in the ω equation.

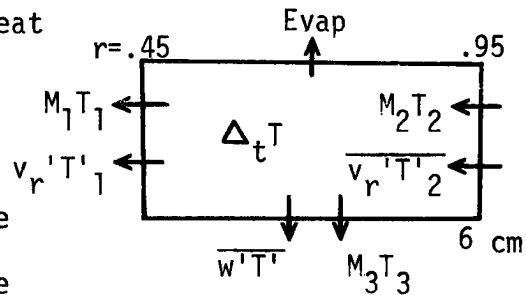
APPENDIX D

HEAT AND MASS BALANCE IN TOP LAYER

From the solution of the ω equation we know the mean vertical motion at 6.0 cm between only $r = 0.45$ to 0.95. To convert this to mean meridional motion we require a \bar{v}_r value at some radius from which we could integrate the continuity equation. Since the surface values of \bar{v}_r were irregular the required \bar{v}_r value could not be determined from the streak measurements.

One alternative is to combine statements of both heat and mass balances in the boxes to solve for the \bar{v}_r through the radial surface. As we require only one \bar{v}_r value if we accept the mass flow through $z = 6$ cm from the vertical motion solution, we write the heat and mass balances between $r = 0.45$ and $r = 0.95$. For the evaporation loss we take a value of 1.0 cc/hour (4.2 watts cooling for $0.45 \leq r \leq 0.95$).

As shown in the sketch, the heat balance of the upper layer contains the products of the mass (M) and its temperature T . Here $\Delta_t T$ is the time change of the mean zonal temperature within the



box and we use mass flows $M = \bar{c}_n (2\pi r \Delta s)$ where \bar{c}_n is \bar{v}_r with $\Delta s = \Delta z$ and \bar{w} with $\Delta s = \Delta r$. Writing mass continuity as $0 = M_1 + M_2 + M_3$ where we define outward flows as positive. Then we write the heat balance as

$$\Delta_t T + M_2 T_2 + M_1 T_1 + M_3 T_3 + (\bar{v}_r' T')_2 + (\bar{v}_r' T')_1 + \bar{w}' T' + E = 0$$

where the eddy heat flows and time changes have the proper area weighting values, and the heat fluxes on the lower surface $M_3 T_3$ and

$\overline{w'T}$ are actually the sum of fluxes computed over radial increments of 0.05 units. The evaporation is converted to a cooling of the entire layer by the proper dimensions and heat constant. As M_3 is known there are two unknowns, M_1 and M_2 , simple algebraic manipulation allows us to solve for either. Table 4 shows the result of these calculations as $\overline{rv}_r \times 10^{-5}$ with minus signs indicating flows into the upper layer. Since r at radius 2 is 0.95 these values are nearly equal to \overline{v}_r and a

TABLE 4

Mass flow through the 7-6 cm layer

Time	$(rv_r)_2$	$(rv_r)_1$	Time	$(rv_r)_2$	$(rv_r)_1$
1	-130	32	9	-170	86
3	-84	0	11	-128	43
5	-30	-3	13	-133	32
7	-119	53	15	-145	55

value of 100 represents a velocity of one mille of the equatorial speed. Even the largest value at $T = 9$ represents an atmospheric value of less than 1.0 m/sec. Since these are part of the direct cell bringing the warmer water away from the heat source, the values occur near the cold source, indicating a tendency toward an indirect cell there. Figure 10 shows the Stokes streamfunction of the mean meridional motion over the entire fluid and indicates how the values in Table 4 match the interior values derived from the ω equation.

APPENDIX E

ENERGY CYCLE EQUATIONS

We develop equations analogous to those of Lorenz (1955) to examine the energy cycle integrated over the entire fluid. The kinetic energy equation formed by vector multiplying the horizontal equation of motion by the velocity is split into zonal and eddy components. Even when integrated over the entire mass, the convective acceleration term does not go to zero, but gives rise to a term which may be interpreted as the conversion from eddy to zonal kinetic energy. We then derive a potential energy equation which contains the conversion between potential and kinetic energy which appeared in the kinetic energy equation. In the process we define the available zonal (and eddy) potential energy, that part of the potential energy which is available for conversion to kinetic energy by frictionless, adiabatic redistribution of mass.

We define the eddy component as the deviation from the zonal average given by the relation $(\overline{\quad}) = \frac{1}{2\pi} \int_0^{2\pi} (\quad) d\theta$

Multiplying the zonally averaged \bar{v}_θ and \bar{v}_r equations by \bar{v}_θ and \bar{v}_r respectively, summing, reducing the equation by use of the averaged continuity equation, and integrating over the mass, we obtain

$$\begin{aligned} \frac{\partial}{\partial t} \langle \bar{K} \rangle &= \langle \bar{v}_\theta' \bar{v}_r' \frac{\partial \bar{v}_\theta}{\partial r} + \bar{\omega}' \bar{v}_\theta' \frac{\partial \bar{v}_\theta}{\partial p} + \bar{v}_r' \bar{v}_r' \frac{\partial \bar{v}_r}{\partial r} + \bar{\omega}' \bar{v}_r' \frac{\partial \bar{v}_r}{\partial p} \rangle \\ &- \langle \frac{\bar{v}_r}{r} [\bar{v}_r'^2 + \bar{v}_\theta'^2] \rangle - g \langle \bar{h} (-\frac{\partial \bar{\omega}}{\partial p}) \rangle + \langle \bar{v}_\theta' \bar{F}_\theta + \bar{v}_r' \bar{F}_r \rangle \end{aligned}$$

The following definitions have been used

$\langle \quad \rangle$ integration over the mass

$$\bar{K} = 1/2 (\bar{v}_\theta^2 + \bar{v}_r^2)$$

$$K' = 1/2 (\bar{v}_\theta'^2 + \bar{v}_r'^2)$$

$\bar{F}_\theta, \bar{F}_r$ zonally-averaged components of the frictional force.

Because of the integration over the entire mass, the advection of \bar{K} by the mean motion tends to zero as do terms involving derivatives with respect to θ . The terms within the first bracket on the right come from the advection term, while the curvature terms appear in the second bracket. Because \bar{v}_r is very small compared to \bar{v}_θ and vanishes upon vertical integration, only the first two terms involving gradients of v_θ are important. We interpret these terms as the tendency for eddy fluxes of angular momentum to convert eddy kinetic energy into zonal kinetic energy $C(K', \bar{K})$. Using the hydrostatic equation in the third term in brackets reduces it to the conversion of zonal potential energy to \bar{K} , $C(\bar{P}, \bar{K}) = -\langle \bar{\omega} \bar{\alpha} \rangle$. Then defining the last term to be the dissipation of \bar{K} , $D(\bar{K})$, we write the equation as

$$\frac{\partial \bar{K}}{\partial t} = C(K', \bar{K}) + C(\bar{P}, \bar{K}) + D(\bar{K})$$

The eddy kinetic energy is derived by subtracting the \bar{K} equation from the total kinetic energy integrated over the mass with the result

$$\frac{\partial K'}{\partial t} = -C(K', \bar{K}) + C(P', K') + D(K')$$

where $C(P', K') = -\langle \bar{\omega}' \alpha' \rangle$ and $D(K') = \langle \bar{v}_\theta' F_\theta' + \bar{v}_r' F_r' \rangle$

To derive the corresponding potential energy equations we begin from the thermodynamic equation in the flux form

$$\frac{\partial \tau}{\partial t} + \frac{\partial (rv_r \tau)}{r \partial r} + \frac{\partial (v_\theta \tau)}{r \partial \theta} + \frac{\partial \omega \tau}{\partial p} = \frac{Q}{C_p}$$

The temperature deviation τ from a standard value is related to a specific volume deviation α by the equation of state $\alpha = \beta^* \tau$. Taking $\beta^* = \beta^*(p)$ we multiply the zonally averaged thermodynamic equation by $\beta^* \tau = \bar{\alpha}$ and take the zonal average, obtaining

$$\frac{\beta^*}{2} \frac{\partial \bar{\tau}^2}{\partial t} + \beta^* \frac{\bar{\tau}}{r} \frac{\partial}{\partial r} \overline{rv_r \tau} + \beta^* \frac{\bar{\tau}}{r} \frac{\partial \bar{\omega} \tau}{\partial p} = \frac{\beta^*}{C_p} \bar{Q} \bar{\tau}$$

where $\epsilon = \frac{f_0^2 L^2}{g\kappa D}$, $\mu = \frac{D}{H}$, $\gamma = \frac{C_p}{C_v}$, $\kappa = D \frac{\partial \ln \theta_s}{\partial z}$, $H = \frac{p_s}{g\rho_s}$ and D and L are the characteristic vertical and horizontal scales. These are the quasi-geostrophic equations where we have dropped the terms involving variation of the Coriolis parameter. A single partial differential equation is derived by eliminating the pressure between e) and f), utilizing the continuity equation to express the divergence in terms of w_0 which is eliminated with the aid of the adiabatic equation h). Using the identity i) the equation is written (Pedlosky, 1964a)

$$\left\{ \frac{\partial}{\partial t} + \psi_x \frac{\partial}{\partial y} - \psi_y \frac{\partial}{\partial x} \right\} \left\{ \psi_{xx} + \psi_{yy} + \frac{1}{\rho_s} (\epsilon \rho_s \psi_z)_z \right\} = 0 \text{ where } \psi = p_0,$$

which can be shown (Charney and Stern, 1962) to be the conservation of potential vorticity. Detailed consideration of the proper formulation of the boundary condition for w_0 at the top and bottom is given in both of the above references. For an incompressible fluid the potential temperature is replaced by the specific volume or by the temperature if the equation of state is linear.

After insertion of the perturbation $\psi = \Psi + \Phi$ and elimination of second order terms, solutions of the form $\Phi = \text{Re } \phi e^{i\alpha(x-ct)}$ are substituted in the linearized equation for the perturbation field Φ . The resulting frequency equation is

$$(u-c) (\phi_{xx} + \phi_{yy} + (\epsilon \rho_s \phi_z)_z - \alpha^2 \phi) + \phi \frac{\partial q}{\partial y} = 0$$

where the northward gradient of the geostrophic potential vorticity is $\frac{\partial q}{\partial y} = -u_{yy} - \frac{1}{\rho_s} (\epsilon \rho_s u_z)_z$ here u is the mean zonal velocity. The flow will be unstable if a solution exists with an associated eigenvalue $c = c_r + ic_i$ whose imaginary part is positive. Only if all solutions have $c_i = 0$ will the undisturbed flow be stable. The criterion is derived from the perturbation energy equation integrated over the

volume. Charney and Stern (1962) state the general theorem: "Zonal flow in a stratified rotating atmosphere which (a) is bounded by rigid horizontal boundaries, or (b) extends to infinity, is stable with respect to axially asymmetric disturbances if the gradient of potential vorticity in isentropic surfaces does not vanish and (a) the potential temperature is constant at the rigid boundaries, or (b) perturbation energy is reflected at infinity."

The non-vanishing of the potential vorticity gradient is thus a sufficient condition for stability and its vanishing a necessary condition for instability.